

NEW PHYSICS AND NEW TECHNOLOGIES IN NEXT-GENERATION NEUTRINO EXPERIMENTS.

Tommaso Boschi

31st March 2020

Submitted in partial fulfilment of the requirements
of the Degree of Doctor of Philosophy

QUEEN MARY UNIVERSITY OF LONDON
Particle Physics Research Centre, School of Physics and Astronomy

and

UNIVERSITY OF DURHAM
Institute for Particle Physics Phenomneology

I, Tommaso Boschi, confirm that the research included within this thesis is my own work or that where it has been carried out in collaboration with, or supported by others, that this is duly acknowledged below and my contribution indicated. Previously published material is also acknowledged below.

I attest that I have exercised reasonable care to ensure that the work is original, and does not to the best of my knowledge break any UK law, infringe any third party's copyright or other Intellectual Property Right, or contain any confidential material.

I accept that the College has the right to use plagiarism detection software to check the electronic version of the thesis.

I confirm that this thesis has not been previously submitted for the award of a degree by this or any other university.

The copyright of this thesis rests with the author and no quotation from it or information derived from it may be published without the prior written consent of the author.

Signature:

Date:

Details of collaboration and publications:

Abstract

We are living a pivotal moment for neutrino physics. A new generation of experiments is about to begin and will extend our understanding of neutrinos. Very large scale experiments, like Hyper-Kamiokande, will collect unprecedented statistics and will constrain oscillation parameters to high precision: the CP violation phase, the octant of θ_{23} , and the mass hierarchy are likely to be determined. Many are the experimental difficulties behind a successful megaton water Cherenkov detector, but improvements in photodetection technologies luckily allow such an ambitious project. One of the most important challenges is to keep systematical uncertainties under control, so as they do not dominate over statistical errors. Assessing the impact of the systematics on the overall sensitivity of the experiment is a fundamental requirement to the final success of Hyper-Kamiokande.

Thanks to powerful accelerator facilities, future long baseline experiments, such as DUNE, will also explore the intensity frontier of neutrino physics and study rare phenomena. Numerous extension to the Standard Model (SM) and alternative theories have been introduced to explain neutrino masses and mixings. These new scenarios often predict new physics, the signature of which is accessible to next-generation experiments. An interesting example comes from low-scale see-saw models, which consider GeV-scale neutral leptons coupled to SM particles with suppressed mixing angles. The near detector system of DUNE is an ideal place for searches of these particles, thanks to high exposure that compensate small event rates.

Current neutrino experiments have also joined this new venture; Super-Kamiokande has been extensively refurbish in view of a new phase, starting in early 2020, in which the detector will turn into a supernova observatory. This is achieved by doping the water of Super-Kamiokande with gadolinium, in order to increase the efficiency of neutron tagging up to 90 %. The use of gadolinium is a novel technique which will be adopted by many existing and planned experiments. The benefits of improved neutron tagging are not limited just to supernova neutrinos, but to a plethora of other studies, such as reactor and atmospheric neutrinos or proton decay.

In this thesis, all of the topics above are addressed. After a review of SM neutrino physics in Chapter 1, the gadolinium-loaded water Cherenkov technique is discussed in Chapter 2 with particular focus on Super-Kamiokande. Chapter 3 deals with CP violation in neutrino oscillation and the potential of Hyper-Kamiokande to constraining oscillation parameteres. In Chapter 4 we study a possible Standard Model extension to explain neutrino masses and in Chapter 5 we evaluate the prospect of DUNE's near detector to searches of new physics.

Contents

1 Neutrinos in the Standard Model and Beyond	7
1.1 Electroweak sector	8
1.1.1 Electroweak interactions	10
1.1.2 Higgs mechanism	11
1.1.3 Fermion mixing	13
1.2 Neutrino oscillations	14
1.2.1 Neutrino mixing	14
1.2.2 Propagation of neutrinos in vacuum	15
1.2.3 Propagation of neutrinos in matter	18
1.3 Neutrino production	18
1.3.1 Solar and supernova neutrinos	20
1.3.2 Atmospheric neutrinos	20
1.3.3 Reactor and accelerator neutrinos	20
1.4 Neutrino interactions	22
1.4.1 Coherent elastic neutrino–nucleus scattering	23
1.4.2 Neutrino–electron scattering	23
1.4.3 Neutrino scattering with nucleons	24
2 The gadolinium phase of Super-Kamiokande	27
2.1 Cherenkov detectors	28
2.2 The Super-Kamiokande experiment	30
2.3 Neutrons in Super-Kamiokande	31
2.3.1 Neutron tagging	32
2.3.2 Neutron calibration	35
2.4 Gadolinium neutron capture	37
2.5 Monitoring gadolinium concentration	40
3 CP violation with the Hyper-Kamiokande experiment	43
3.1 CP violation in neutrino oscillations	44

3.2	Hyper-Kamiokande experiment	47
3.3	Sensitivity studies	48
3.3.1	Event samples	48
3.3.2	Systematic model	49
3.3.3	Oscillation space	50
3.3.4	χ^2 test	51
3.4	Systematic studies	52
3.4.1	Validation of the fitter	52
3.4.2	Variations to the nominal model	53
3.5	Dependencies on exclusion of CP	53
4	Neutrino mass generation	54
4.1	Heavy neutrinos in seesaw models	56
4.2	Heavy neutrino decay	58
4.2.1	Polarised Majorana neutrino decay	60
4.2.2	Polarised (pseudo-)Dirac neutrino decay	65
4.3	Heavy neutrino production	66
4.3.1	Two-body decays	68
4.3.2	Three-body decays	69
5	HNL discovery with the DUNE experiment	71
5.1	Liquid argon time projection chamber	71
5.2	The DUNE experiment	71
5.3	Simulation of events at DUNE ND	71
5.3.1	Flux prediction	73
5.3.2	Background evaluation	75
5.3.3	HNL decay events and signal efficiency	78
5.4	Sensitivities of DUNE ND	79
5.4.1	Single dominant mixing	79
5.4.2	Two dominant mixings	81
5.5	Mass model constraints from DUNE ND	82
5.5.1	Mass model scan	82
5.5.2	Overall sensitivity	84
5.6	Background reduction	86
5.6.1	Two-body decays	87
5.6.2	Three-body decays	87
5.6.3	EM-detected decays	88

6 Conclusions	90
A List of integrals and identities	91
A.0.1 Decay widths	91
A.0.2 Scaling factors for three body-decays	92
A.1 Polarised $N \rightarrow \nu \ell_\alpha^- \ell_\beta^+$ distributions	94
A.1.1 Dirac ν_i	94
A.1.2 Dirac $\bar{\nu}_i$	94
A.1.3 Majorana N_i	94
B Open charm production	96

Chapter 1

Neutrinos in the Standard Model and Beyond

The Standard Model (SM) is a renormalisable Yang-Mills theory ?? that describes the strong, electromagnetic, and weak interactions of elementary particles in the framework of quantum field theory. It is based on the local gauge symmetry group

$$\mathrm{SU}(3)_C \otimes \mathrm{SU}(2)_L \otimes \mathrm{U}(1)_Y \quad (1.1)$$

where C , L and Y denote respectively colour, left-handed chirality and weak hyper-charge. The gauge group uniquely determines the interactions and the number of vector gauge bosons that correspond to the generators of the group. The electroweak subgroup $\mathrm{SU}(2)_L \otimes \mathrm{U}(1)_Y$ undergoes a spontaneous symmetry breaking process out of which three of the four vector bosons acquire mass (W^\pm and Z bosons) and the last one, the photon, remains massless. The colour section is unbroken and does not mix with the electroweak sector: the generators of the algebra of $\mathrm{SU}(3)_C$ corresponds to eight massless gluons. Since the number and properties of the gauge bosons is determined by the SM group, the only independent parameters left are the coupling constants of the interactions, which can be determined by the experiments. The spontaneous breaking symmetry requires at least one scalar boson thanks to the Higgs mechanism. The recent discovery of the Higgs boson is the crowning achievement of the SM ??.

On the contrary, the number and properties of scalar bosons and fermions are left unconstrained, except for the fact that they must transform according to the representations of the symmetry group, while the fermion representations must lead to the cancellation of quantum anomalies.

The known elementary fermions are divided in two categories, quarks and leptons. They are distinguished by the fact that quarks participate in all the interactions whereas leptons participate only in the electroweak interactions.

Generation	1st	2nd	3rd
Quark	u	c	t
	d	s	b
Leptons	e	μ	τ
	ν_e	ν_μ	ν_τ

Despite being the most successful theory of particle physics to date, the SM is actually limited in its approximation to reality, in that some clear evidences cannot be explained. The most outstanding breakthrough is the neutrino oscillations, which was awarded the Nobel Prize in Physics in 2015 and has proved that the neutrinos are not all massless, as it is assumed by theory. Mass terms for the neutrinos can be included in the SM, with the implications of theoretical problems. Likewise, the SM is unable to provide an explanation of the observed asymmetry between matter and anti-matter. It was noted by Sakharov that a solution to this puzzle would require some form of C and CP violation in the early Universe, along with Baryon number violation and out-of-equilibrium interactions. These facts suggest that the Standard Model is not a complete theory and additional physics Beyond the Standard Model (BSM) is required.

The study of neutrinos is for sure one of the most promising probe to BSM physics and is of vital importance to the future development of particle physics, in particular through precision measurement of their interactions. A deep understanding of neutrino interactions, and neutrino-nucleon interactions in particular, could lead to a great impact on long-baseline experiments, proton decay search, and supernova detection. Since the SM is a renormalisable theory, even its quantum corrections are insensitive to the physics beyond the SM. Because of this reason, the SM is phenomenologically very successful and so far has been able to describe all the known phenomena, except for the indications in favour of neutrino oscillations that we will discuss in the following chapters.

1.1 Electroweak sector

The electroweak (EW) sector of the SM is formed by the direct product of the weak isospin group $SU(2)_L$ and the hyper-charge group $U(1)_Y$. The two groups are connected by the Gell-Mann–Nishijima relation which connects the I_3 component of the weak isospin operator and the hyper-charge operator Y with the charge operator Q as

$$Q = I_3 + \frac{Y}{2} . \quad (1.2)$$

Left-handed chiral components of the fermion fields form doublets under $SU(2)_L$

$$\mathbf{L}_L = \begin{pmatrix} \boldsymbol{\nu}_L \\ \boldsymbol{\ell}_L \end{pmatrix} , \quad \mathbf{Q}_L = \begin{pmatrix} \mathbf{q}_L^U \\ \mathbf{q}_L^D \end{pmatrix} , \quad (1.3)$$

where the left-handed fields in bold-face represent the fermion families

$$\boldsymbol{\nu}_L = \begin{pmatrix} \nu_{eL} \\ \nu_{\mu L} \\ \nu_{\tau L} \end{pmatrix}, \quad \boldsymbol{\ell}_L = \begin{pmatrix} e_L \\ \mu_L \\ \tau_L \end{pmatrix}, \quad \boldsymbol{q}_L^D = \begin{pmatrix} d_L \\ s_L \\ b_L \end{pmatrix}, \text{ and } \boldsymbol{q}_L^U = \begin{pmatrix} u_L \\ c_L \\ t_L \end{pmatrix}. \quad (1.4)$$

The right-handed fields, instead, transform simply as singlets and they are

$$\boldsymbol{\ell}_R = \begin{pmatrix} e_R \\ \mu_R \\ \tau_R \end{pmatrix}, \quad \boldsymbol{q}_R^D = \begin{pmatrix} d_R \\ s_R \\ b_R \end{pmatrix}, \text{ and } \boldsymbol{q}_R^U = \begin{pmatrix} u_R \\ c_R \\ t_R \end{pmatrix}. \quad (1.5)$$

Note that the right-handed components of the neutrino fields, $\nu_{\alpha R}$, are not historically considered in the SM because the neutrinos were believed massless until recent times ?? . As such, neutrinos are assumed to be massless in the SM. The EW Lagrangian is therefore the most general renormalisable Lagrangian invariant under the local symmetry $SU(2)_L \otimes U(1)_Y$:

$$\begin{aligned} \mathcal{L}_{EW} = & i \bar{\boldsymbol{L}}_L \not{D} \boldsymbol{L}_L + i \bar{\boldsymbol{Q}}_L \not{D} \boldsymbol{Q}_L + i \bar{\boldsymbol{\ell}}_R \not{D} \boldsymbol{\ell}_R + i \bar{\boldsymbol{q}}_R^D \not{D} \boldsymbol{q}_R^D + i \bar{\boldsymbol{q}}_R^U \not{D} \boldsymbol{q}_R^U \\ & - \frac{1}{4} B_{\mu\nu} B^{\mu\nu} - \frac{1}{4} \mathbf{A}_{\mu\nu} \mathbf{A}^{\mu\nu} + (D_\mu H)^\dagger (D^\mu H) - \mu^2 H^\dagger H - \lambda (H^\dagger H)^2 \\ & - \left(\bar{\boldsymbol{L}}_L Y^\ell H \boldsymbol{\ell}_R + \bar{\boldsymbol{Q}}_L Y^D H \boldsymbol{q}_R^D + \bar{\boldsymbol{Q}}_L Y^U \tilde{H} \boldsymbol{q}_R^U + \text{h.c.} \right), \end{aligned} \quad (1.6)$$

where the covariant derivative is defined as

$$D_\mu = \partial_\mu + ig \mathbf{A}_\mu \cdot \mathbf{I} + ig' B_\mu \frac{Y}{2}, \quad (1.7)$$

and satisfies gauge invariance, and $\tilde{H} = i\sigma_2 H^*$ is the conjugate Higgs field. It is important to note that Dirac mass terms for fermion fields other than neutrinos are anyway forbidden by the gauge symmetry. These terms will become manifest once the symmetry is broken through the Higgs mechanism (see Section 1.1.2). The vector boson fields $\mathbf{A}^\mu = (A_1^\mu, A_2^\mu, A_3^\mu)$ and B^μ corresponds respectively to the three generators $\mathbf{I} = (I_1, I_2, I_3)$ of the $SU(2)_L$ group and the generator Y of the $U(1)_Y$ group. The $SU(2)_L$ generators are $I_a = \sigma_a/2$, where σ_a are the Pauli matrices, and thus satisfy the commutation relation

$$[I_a, I_b] = i\varepsilon_{abc} I_c, \quad (1.8)$$

with ε_{abc} the Levi-Civita tensor.

1.1.1 Electroweak interactions

Expanding the covariant derivative and ignoring the kinetic terms, we can retrieve the interaction term for the leptonic sector

$$\mathcal{L}_{\text{int}} = -\frac{1}{2} \sum_{\alpha} \begin{pmatrix} \bar{\nu}_{\alpha L} & \bar{\ell}_{\alpha L} \end{pmatrix} \begin{pmatrix} g \mathbb{A}_3 - g' \mathbb{B} & g(\mathbb{A}_1 - i\mathbb{A}_2) \\ g(\mathbb{A}_1 + i\mathbb{A}_2) & -g \mathbb{A}_3 - g' \mathbb{B} \end{pmatrix} \begin{pmatrix} \nu_{\alpha L} \\ \ell_{\alpha L} \end{pmatrix} + g' \bar{\ell}_{\alpha R} \mathbb{B} \ell_{\alpha R}, \quad (1.9)$$

where α is a family generation index. Defining the combinations

$$W^{\mu} = (A_1^{\mu} - iA_2^{\mu})/\sqrt{2} \quad (1.10)$$

$$Z^{\mu} = \cos \vartheta_W A_3^{\mu} - \cos \vartheta_W B^{\mu} \quad (1.11)$$

$$A^{\mu} = \sin \vartheta_W A_3^{\mu} + \cos \vartheta_W B^{\mu}, \quad (1.12)$$

the electromagnetic field A^{μ} is expressed as a rotation of A_e^{μ} and B^{μ} , thus recovering QED; the new field Z^{μ} also describes a neutral current process. The Lagrangian in Eq. (1.9) can therefore be divided into two parts, $\mathcal{L}_{\text{int}} = \mathcal{L}^{(CC)} + \mathcal{L}^{(NC)}$, describing charged-current (CC) and neutral-current (NC) interactions. These are

$$\mathcal{L}_{\text{CC,L}} = -\frac{g}{2\sqrt{2}} j_{\text{CC,L}}^{\mu} W_{\mu} + \text{h.c.} \quad \text{and} \quad \mathcal{L}_{\text{NC,L}} = -\frac{g}{2 \cos \vartheta_W} j_{\text{NC,L}}^{\mu} Z_{\mu} + g \sin \vartheta_W \bar{\ell} \mathbb{A} \ell, \quad (1.13)$$

where the W and Z vector bosons have been factorised out, leaving the fermionic currents

$$j_{\text{CC,L}}^{\mu} = \bar{\nu} \gamma^{\mu} (1 - \gamma^5) \ell \quad (1.14)$$

$$j_{\text{NC,L}}^{\mu} = \bar{\nu} \gamma^{\mu} (g_V^{\nu} - g_A^{\nu} \gamma^5) \nu + \bar{\ell} \gamma^{\mu} (g_V^{\ell} - g_A^{\ell} \gamma^5) \ell. \quad (1.15)$$

The constant g' has been re-written in terms of g and ϑ_W by setting to zero the coupling of neutrinos to the electromagnetic field for neutrinos, which gives

$$g \sin \vartheta_W = g' \cos \vartheta_W. \quad (1.16)$$

Another important relation comes from the charged lepton couplings with the electromagnetic field which must coincide the QED Lagrangian: we have that $g \sin \vartheta_W = q_e$ and so $g^2 + g'^2 = q_e^2$. The constants g_V and g_A , introduced in Eq. (??), can be defined for any fermion f as

$$g_V^f = I_3^f - 2q^f \sin^2 \vartheta_W \quad \text{and} \quad g_A^f = I_3^f. \quad (1.17)$$

Thanks to this notation, the interaction Lagrangian for the quark sector can be written in the same form of Eq. (1.13), where the fermionic currents of Eqs. (1.14) and (1.15) now become

$$j_{\text{CC},Q}^\mu = \bar{\mathbf{q}}^U \gamma^\mu (1 - \gamma^5) \mathbf{q}^D \quad (1.18)$$

$$j_{\text{NC},Q}^\mu = \bar{\mathbf{q}}^U \gamma^\mu (g_V^U - g_A^U \gamma^5) \mathbf{q}^U + \bar{\mathbf{q}}^D \gamma^\mu (g_V^D - g_A^D \gamma^5) \mathbf{q}^D . \quad (1.19)$$

1.1.2 Higgs mechanism

In the EW Lagrangian in Eq. (1.6), the Higgs H is a complex scalar field and an $SU(2)_L$ doublet

$$H(x) = \begin{pmatrix} H^+(x) \\ H^0(x) \end{pmatrix} , \quad (1.20)$$

the potential of which can spontaneously break if $\lambda > 0$ and $\mu^2 < 0$, in

$$V(H) = \mu^2 H^\dagger H + \lambda (H^\dagger H)^2 . \quad (1.21)$$

Defining

$$v \equiv \sqrt{-\frac{\mu^2}{\lambda}} , \quad (1.22)$$

the potential $V(H)$ shows a minimum for $H^\dagger H = v^2/2$, which corresponds to the lowest energy state, or vacuum. In general, fermion and non-zero spin boson fields must have a vanishing vacuum expectation value (vev), so as to preserve the Lorentz symmetries of space and time. The same applies to charged scalar fields, as the vacuum is electrically chargeless. On the other hand, neutral scalar fields can have a nonzero value in vacuum, and so the vev of the Higgs field could be given by

$$\langle H \rangle = \frac{1}{\sqrt{2}} \begin{pmatrix} 0 \\ v \end{pmatrix} . \quad (1.23)$$

This value spontaneously breaks the EW group $SU(2)_L \times U(1)_Y$, but it remains invariant under the gauge transformations from the $U(1)_Q$ group, with Q from Eq. (1.2), which guarantees the existence of a massless gauge boson associated with the photon. We can expand the scalar field around its vev and by choosing the unitary gauge three of the four real scalar fields can be rotated away being unphysical, simplifying to

$$\langle H \rangle = \frac{1}{\sqrt{2}} \begin{pmatrix} 0 \\ v + h(x) \end{pmatrix} . \quad (1.24)$$

Using the definition of the EW fields in Eq. (1.10), the covariant derivative of Eq. (1.7) applied to the Higgs is

$$D_\mu H(x) = \frac{1}{\sqrt{2}} \begin{pmatrix} i \frac{g}{\sqrt{2}} W_\mu(x)[v + h(x)] \\ \partial_\mu h(x) - i \frac{g}{2 \cos \vartheta_W} Z_\mu(x)[v + h(x)] \end{pmatrix}. \quad (1.25)$$

The Lagrangian terms with the Higgs field therefore becomes

$$\begin{aligned} \mathcal{L}_{\text{Higgs}} = & \frac{1}{2} (\partial h)^2 - v^2 \lambda h^2 - \lambda h^3 - \frac{\lambda}{4} h^4 + \frac{g^2 v^2}{4} W_\mu^\dagger W^\mu + \frac{g^2 v^2}{8 \cos^2 \vartheta_W} Z_\mu Z^\mu \\ & + \frac{g^2 v}{2} W_\mu^\dagger W^\mu h + \frac{g^2 v}{4 \cos^2 \vartheta_W} Z_\mu Z^\mu h + \frac{g^2}{4} W_\mu^\dagger W^\mu h^2 + \frac{g^2}{8 \cos^2 \vartheta_W} Z_\mu Z^\mu h^2. \end{aligned} \quad (1.26)$$

The second term of the first line is a mass term for the scalar fields, from which the mass of the Higgs boson is determined to be $m_H = v \sqrt{(2\lambda)} = \sqrt{-2\mu^2}$, a value recently measured ???. The fifth and sixth terms represent the mass terms for the W and Z bosons, namely

$$m_W = \frac{gv}{2}, \quad m_Z = \frac{gv}{2 \cos \vartheta_W}, \quad (1.27)$$

and the following parameter

$$\rho = \frac{m_W^2}{m_Z^2 \cos^2 \vartheta_W} \quad (1.28)$$

is predicted to be $\rho = 1$ in the SM: experimentally it is measured to be $\rho = 0.999999$. The other terms of 1.26 describe self-interactions of the Higgs and interactions with the W and Z vector bosons.

Applying the same expansion of Eq. (1.24) to the Yukawa terms of the SM Lagrangian, we direct coupling between left and right chiral fields and trilinear couplings of the fermions with the Higgs. We have in the lepton section

$$\mathcal{L}_{H,L} = -\frac{v}{\sqrt{2}} \bar{\ell}_L Y^\ell \ell_R - \frac{1}{\sqrt{2}} \bar{\ell}_L Y^\ell \ell_R h + \text{h.c.}, \quad (1.29)$$

The same is found in the quark sector:

$$\mathcal{L}_{H,Q} = -\left(\frac{v}{\sqrt{2}} \bar{q}_L^D Y^D q_R^D + \frac{v}{\sqrt{2}} \bar{q}_L^U Y^U q_R^U \right) - \left(\frac{1}{\sqrt{2}} \bar{q}_L^D Y^D q_R^D h + \frac{1}{\sqrt{2}} \bar{q}_L^U Y^U q_R^U h \right) + \text{h.c.}. \quad (1.30)$$

The terms in the Lagrangians of Eqs. (1.29) and (1.30) proportional to $\bar{f}_L f_R = \bar{f} f$ are Dirac mass terms for the fermion f . However, there is no principle by which the Yukawa coupling matrices Y^f should be diagonal *a priori*, but without a diagonal matrix the fermion masses are not properly defined. Being a generic complex matrix, the diagonalisation can be performed via a biunitary transformation

$$V_L^{f\dagger} \left(\frac{v}{\sqrt{2}} Y^f \right) V_R^f = \frac{v}{\sqrt{2}} \hat{Y}_\alpha^f = \text{diag} \left(\frac{y_\alpha^f v}{\sqrt{2}} \right), \quad (1.31)$$

where V_L and V_R are both unitary matrices and the fermion masses are defined by the Yukawa couplings

$$m_\alpha^f \equiv \frac{y_\alpha^f v}{\sqrt{2}} , \quad (1.32)$$

with α a family generation index. The biunitary transformation acts on the lepton fields as

$$\hat{\ell}_L = V_L^{\ell\dagger} \ell_L \quad , \quad \hat{\ell}_R = V_R^{\ell\dagger} \ell_R \quad (1.33)$$

and on the quark fields as

$$\begin{aligned} \hat{q}_L^D &= V_L^{D\dagger} q_L^D \quad , \quad \hat{q}_R^D = V_R^{D\dagger} q_R^D \\ \hat{q}_L^U &= V_L^{U\dagger} q_L^U \quad , \quad \hat{q}_R^U = V_R^{U\dagger} q_R^U , \end{aligned} \quad (1.34)$$

Dropping the “hat notation” to indicate mass eigenfields, we obtain in the lepton sector

$$\mathcal{L}_{\text{mass}} = - \sum_{\alpha=e,\mu,\tau} \frac{y_\alpha^\ell v}{\sqrt{2}} \bar{\ell}_\alpha \ell_\alpha = - \sum_{\alpha=e,\mu,\tau} m_\alpha \bar{\ell}_\alpha \ell_\alpha , \quad (1.35)$$

and in the quark sector

$$\mathcal{L}_{\text{mass}} = - \sum_{\alpha=d,s,b} \left(\frac{y_\alpha^D v}{\sqrt{2}} \bar{q}_\alpha^D q_\alpha^D \right) - \sum_{\beta=u,c,t} \left(\frac{y_\beta^U v}{\sqrt{2}} \bar{q}_\beta^U q_\beta^U \right) = - \sum_{\alpha=d,s,b} (m_\alpha \bar{q}_\alpha^D q_\alpha^D) - \sum_{\beta=u,c,t} (m_\beta \bar{q}_\beta^U q_\beta^U) . \quad (1.36)$$

As noted previously, in the SM there are no mass terms for neutrino fields.

1.1.3 Fermion mixing

The same transformations of Eqs. (1.42) and (1.34) should be equally applied to all the parts of the EW Lagrangian. Let us start from the quark CC current expressed in Eq. (1.18)

$$j_{\text{CC},Q}^\mu = 2 \bar{q}_L^U \gamma^\mu q_L^D = 2 \bar{q}_L^U V_L^{U\dagger} \gamma^\mu V_L^D \hat{q}_L^D = 2 \bar{q}_L^U \gamma^\mu V \hat{q}_L^D , \quad (1.37)$$

where the unitary matrix $V = V_L^{U\dagger} V_L^D$, called Cabibbo-Kobayashi-Maskawa (CKM) matrix, describes the mixing between quark fields in weak interaction processes when initial and final states represent particles with definite masses. The same mixing matrix, however, does not appear in the NC current of Eq. (1.19); defining the couplings $2g_L^f = g_V^f + g_A^f$ and $2g_R^f = g_V^f - g_A^f$, the current with mass eigenstates becomes

$$\begin{aligned} j_{\text{NC},Q}^\mu &= 2g_L^U \bar{q}_L^U \gamma^\mu q_L^U + 2g_R^U \bar{q}_R^U \gamma^\mu q_R^U + 2g_L^D \bar{q}_L^D \gamma^\mu q_L^D + 2g_R^D \bar{q}_R^D \gamma^\mu q_R^D \\ &= 2g_L^U \bar{q}_L^U V_L^{U\dagger} \gamma^\mu V_L^U \hat{q}_L^U + 2g_R^U \bar{q}_R^U V_R^{U\dagger} \gamma^\mu V_R^U \hat{q}_R^U + 2g_L^D \bar{q}_L^D V_L^{D\dagger} \gamma^\mu V_L^D \hat{q}_L^D + 2g_R^D \bar{q}_R^D V_R^{D\dagger} \gamma^\mu V_R^D \hat{q}_R^D \\ &= 2g_L^U \bar{\hat{q}}_L^U \gamma^\mu \hat{q}_L^U + 2g_R^U \bar{\hat{q}}_R^U \gamma^\mu \hat{q}_R^U + 2g_L^D \bar{\hat{q}}_L^D \gamma^\mu \hat{q}_L^D + 2g_R^D \bar{\hat{q}}_R^D \gamma^\mu \hat{q}_R^D . \end{aligned} \quad (1.38)$$

The neutral current with massive fields has the same form of the neutral current with un-rotated fields. This is true also for the electromagnetic current of the EW Lagrangian. This phenomenon is called Glashow-Iliopoulos-Maiani (GIM) mechanism, by which flavour-changing neutral currents (FCNCs) are forbidden at tree level thanks to the unitarity of the weak interaction, but allowed in suppressed loop diagrams.

Looking at the lepton sector, the transformation of Eq. (1.42) are not analogously defined for neutrino fields. Therefore, we can arbitrarily choose neutrino states such that $\hat{\nu}_L = V_L^{\ell\dagger} \nu_L$, where V_L^ℓ is the same of Eq. (1.42). The lepton CC current becomes

$$j_{\text{CC},L}^\mu = 2 \bar{\nu}_L \gamma^\mu \ell_L = 2 \bar{\nu}_L V_L^{\ell\dagger} \gamma^\mu V_L^\ell \hat{\ell}_L = 2 \bar{\nu}_L \gamma^\mu \hat{\ell}_L . \quad (1.39)$$

The fields $\hat{\nu} = (\hat{\nu}_e, \hat{\nu}_\mu, \hat{\nu}_\tau)$ are called *flavour neutrino fields*, because they couple only to the corresponding charged lepton fields in the equation above. As in the case of the quark fields, thanks to the unitarity of the matrices V_L^ℓ and V_R^ℓ the GIM mechanism applies even for the leptonic neutral current.

1.2 Neutrino oscillations

As seen in Section 1.1, the SM does not consider right-handed neutrino fields. For this reason, a Yukawa term coupling the lepton $SU(2)_L$ doublet with the conjugate Higgs field does not appear in the EW Lagrangian. It follows that after the spontaneous symmetry breaking caused by the Higgs non-zero vev the neutrinos do not gain Dirac mass terms, as the other fermions do. This “asymmetry” between fermion fields can be easily resolved by extending the SM, introducing right-handed neutrino fields

$$\nu_R = \begin{pmatrix} \nu_{eR} \\ \nu_{\mu R} \\ \nu_{\tau R} \end{pmatrix} . \quad (1.40)$$

With both chiralities, Dirac mass terms can be constructed also for neutrinos, leading however to neutrino mixing and so the neutrino oscillation phenomenon, observed in various neutrino experiments.

1.2.1 Neutrino mixing

Thanks to this extension, the following Yukawa term is now allowed

$$\mathcal{L}_{\text{EW}} \supset - \left(\bar{L}_L Y^\ell H \ell_R + \bar{L}_L Y^\nu \tilde{H} \nu_R + \text{h.c.} \right) , \quad (1.41)$$

and using the expansion of Eq. (1.24) we have to diagonalise the Yukawa matrix with a biunitary transformation to define masses for the neutrino fields. This lead to new eigenfields

$$\hat{\nu}_L = V_L^{\nu\dagger} \boldsymbol{\nu}_L = \begin{pmatrix} \nu_{1L} \\ \nu_{2L} \\ \nu_{3L} \end{pmatrix}, \quad \hat{\nu}_R = V_R^{\nu\dagger} \boldsymbol{\nu}_R = \begin{pmatrix} \nu_{1R} \\ \nu_{2R} \\ \nu_{3R} \end{pmatrix}, \quad (1.42)$$

where the fields $\nu_i = \nu_{iL} + \nu_{iR}$ describe Dirac neutrinos with definite masses. Looking at the lepton sector, the transformation of Eq. (1.42) are not analogously defined for neutrino fields. Therefore, we can arbitrarily choose neutrino states such that $\hat{\nu}_L = V_L^{\ell\dagger} \boldsymbol{\nu}_L$, where V_L^ℓ is the same of Eq. (1.42). Having now neutrino mass eignestates, the lepton charged current of Eq. (1.14) becomes

$$j_{CC,L}^\mu = 2 \bar{\nu}_L \gamma^\mu \ell_L = 2 \bar{\nu}_L V_L^{\nu\dagger} \gamma^\mu V_L^\ell \hat{\ell}_L = 2 \bar{\nu}_L \gamma^\mu U \hat{\ell}_L, \quad (1.43)$$

where the unitary matrix $U = V_L^\nu V_L^\ell$ is completely analogous to the CKM matrix of the quark weak charged current. This matrix is called Pontecorvo-Maki-Nakagawa-Sakata (PMNS) matrix. Since the flavour of charged lepton is uniquely defined by their masses, it is customary to re-define the left-handed flavour neutrino fields as

$$\boldsymbol{\nu}_L = U \hat{\boldsymbol{\nu}}_L, \quad (1.44)$$

which allows to write the charged current Lagrangian in terms of flavour neutrinos begin careful that if neutrino masses are taken into account mixing of the fields occur:

$$\begin{aligned} \mathcal{L}_{CC,L} &= -\frac{g}{\sqrt{2}} \sum_{\alpha=e,\mu,\tau} \bar{\nu}_\alpha W(1-\gamma^5) \ell_\alpha + \text{h.c.} \\ &= -\frac{g}{\sqrt{2}} \sum_{\alpha=e,\mu,\tau} \sum_{i=1}^3 U_{\alpha i}^* \bar{\nu}_i W(1-\gamma^5) \ell_\alpha + \text{h.c.} \end{aligned} \quad (1.45)$$

The GIM mechanism is still valid and no mixing occurs in neutral current interactions.

1.2.2 Propagation of neutrinos in vacuum

The effect of neutrino mixing is mostly visible in the propagation of neutrinos in space-time. Neutrinos with flavour α are produced and detected in charged current interactions in association with a charged lepton, according to Eq. (1.45). Approximating the neutrino field with plane-waves, the flavour states are described by

$$|\nu_\alpha\rangle = \sum_i U_{\alpha i}^* |\nu_i\rangle, \quad (1.46)$$

where the mass eigenstates are orthonormal, $\langle \nu_i | \nu_j \rangle = \delta_{ij}$, and due to the unitarity of the PMNS matrix, we have $\langle \nu_\alpha | \nu_\beta \rangle = \delta_{\alpha\beta}$. It follows that the probability of producing and detecting a neutrino in the

same point of space-time is, unexpectedly, one. However, in a typical neutrino experiment, production and detection of neutrinos happen in two different locations and times. The massive neutrino states $|\nu_i\rangle$ are eigenstates of the Hamiltonian, with eigenvalues their energies:

$$\mathcal{L}|\nu_i\rangle = E_i |\nu_i\rangle = \sqrt{\mathbf{p}^2 + m_i^2} |\nu_i\rangle , \quad (1.47)$$

with \mathbf{p} the momentum of the produced flavour neutrino. The Hamiltonian dictates the time evolution of the states through the Schrodinger's equation, and so assuming neutrinos evolve as plane waves, we have

$$|\nu_i(t)\rangle = e^{-iE_i t} |\nu_i\rangle \quad \text{and} \quad |\nu_\alpha(t)\rangle = \sum_i U_{\alpha i}^* e^{-iE_i t} |\nu_i\rangle . \quad (1.48)$$

Using the relation of Eq. (1.46), the pure neutrino flavour state $|\nu_\alpha(t)\rangle$ at $t = 0$ is expressed as a superposition of flavour states at time $t > 0$, as

$$|\nu_\alpha(t)\rangle = \sum_{\beta=e,\mu,\tau} \left(\sum_i U_{\alpha i}^* e^{-iE_i t} U_{\beta i} \right) |\nu_\beta\rangle , \quad (1.49)$$

therefore the transition probability from a state ν_α to a state ν_β over a certain amount of time t is

$$P(\nu_\alpha \rightarrow \nu_\beta) \equiv |\langle \nu_\alpha | \nu_\beta(t) \rangle|^2 = \sum_{ij} U_{i\alpha}^* U_{\beta i} U_{\alpha j} U_{j\beta}^* e^{-i(E_j - E_i)t} . \quad (1.50)$$

For ultra relativistic neutrino, the energy values can be approximated by

$$E_i \simeq E + \frac{m_i^2}{2E} , \quad (1.51)$$

whereas the propagation time is comparable to the propagation length, $t \simeq L$ as it is easier to determining experimentally. Adopting these approximations, the probability of Eq. (1.50) is

$$P(\nu_\alpha \rightarrow \nu_\beta) \equiv |\langle \nu_\alpha | \nu_\beta(t) \rangle|^2 = \sum_{ij} U_{i\alpha}^* U_{\beta i} U_{\alpha j} U_{j\beta}^* \exp\left(-i \frac{\Delta m_{ij}^2 L}{2E}\right) , \quad (1.52)$$

where $\Delta m_{ij}^2 = m_i^2 - m_j^2$ are the squared mass differences of the neutrinos. The probability of Eq. (1.52) is called *oscillation probability* because it shows an oscillatory behaviour with respect to L/E , which depend on the experiment, while the other parameters—the PMNS matrix elements and the neutrino masses—are constant of nature. The transition probability for $\alpha = \beta$ is usually called *disappearance probability*, and for $\alpha \neq \beta$ is called *appearance probability*, because typically experiments measure the amount of neutrino of a certain flavour

The oscillating term is the result of the interference of different massive neutrinos, which propagate at different velocities, but coherency between states is preserved. It could happen that neutrinos are

produced or detected incoherently, for which interfere terms do not appear, or that the resolution on the propagation length or the energy is limited, for which the probability must be average. In both cases, the oscillation probability simplifies to

$$\langle P(\nu_\alpha \rightarrow \nu_\beta) \rangle = \sum_i |U_{\alpha i}|^2 |U_{\beta i}|^2 , \quad (1.53)$$

and for $\alpha \neq \beta$ it can be shown that the maximum value the averaged probability can take is

$$\langle P(\nu_\alpha \rightarrow \nu_\beta) \rangle_{\max} = \frac{1}{N} , \quad (1.54)$$

with N the number of massive neutrinos. Under these circumstances, the elements of the mixing matrix have all the same absolute, called *N-maximal mixing*. This corresponds to minimal average disappearance probability and maximal average appearance probability, equal to $1/N$ in each possible channel.

Apart from this limit scenario, the PMNS matrix (and the CKM matrix) are generic unitary $N \times N$ matrices, where N is the number of fermion generations. A matrix with this characteristics depends on N^2 independent real parameters, divided among

$$\frac{N(N-1)}{2} \text{ angles and } \frac{N(N+1)}{2} \text{ phases .} \quad (1.55)$$

Due to the unitarity of the neutral currents, only the weak charged current can manifest these phases, even though not all of them are observable: $2N - 1$ phases can be reabsorbed by a redefinition of the fermion fields. The physical phases are therefore just

$$\frac{(N-1)(N-2)}{2} , \quad (1.56)$$

meaning that with three generations the PMNS matrix (and the CKM matrix) can be described by three mixing angles and one physical phase. The PMNS matrix is typically parameterised as follows

$$U = \begin{pmatrix} 1 & 0 & 0 \\ 0 & c_{23} & s_{23} \\ 0 & -s_{23} & c_{23} \end{pmatrix} \begin{pmatrix} c_{13} & 0 & s_{13}e^{-i\delta_{CP}} \\ 0 & 1 & 0 \\ -s_{13}e^{i\delta_{CP}} & 0 & c_{13} \end{pmatrix} \begin{pmatrix} c_{12} & s_{12} & 0 \\ -s_{12} & c_{12} & 0 \\ 0 & 0 & 1 \end{pmatrix} , \quad (1.57)$$

where $c_{ij} \equiv \cos \theta_{ij}$ and $s_{ij} \equiv \sin \theta_{ij}$. The angle δ_{CP} is the physical phase which is responsible for CP violation (see Section 3.1).

1.2.3 Propagation of neutrinos in matter

Neutrinos propagating in a dense medium can interact with the particles in the medium. The probability of an incoherent inelastic scattering is very small. For example the characteristic cross section for ν -proton scattering is of the order

$$\sigma \simeq \frac{G_F^2 s}{\pi} \sim 10^{-43} \text{cm}^2 \left(\frac{E}{\text{MeV}} \right)^2 \quad (1.58)$$

where s is the square of the center of mass energy of the collision. When neutrinos propagate in dense matter, they can also interact coherently with the particles in the medium. By definition, in coherent interactions, the medium remains unchanged so it is possible to have interference of the forward scattered and the unscattered neutrino waves which enhances the effect of matter in the neutrino propagation. In this case the effect of the medium is not on the intensity of the propagating neutrino beam, which remains unchanged, but on the phase velocity of the neutrino wave, and for this reason the effect is proportional to G_F , instead of the G_F^2 dependence of the incoherent scattering. Coherence also allows decoupling the evolution equation of the neutrinos from those of the medium. In this limit the effect of the medium is introduced in the evolution equation for the neutrinos in the form of an effective potential which depends on the density and composition of the matter.

In general, the discussion of oscillations in matter for three neutrino mixing is quite complicated, because of the possible interplay of the effects of the different mass squared differences. Fortunately, in the case of the hierarchy of squared-mass differences, for which

$$\Delta m_{\text{sol}}^2 = \Delta m_{21}^2 \ll \Delta m_{\text{atm}}^2 = |\Delta m_{31}^2| , \quad (1.59)$$

the effects of the large and small squared-mass differences can be separated out, leading to a considerable simplification of the discussion and a clear understanding of the physical mechanisms at work in experiments.

1.3 Neutrino production

Neutrinos are the most abundant fermion in the Universe. With the expansion and cooling of the Universe, the rate of weak interaction primordial neutrinos decreased below the expansion rate, resulting in a decoupling of the neutrinos from the other particles. These *relic neutrinos* form what is called the Cosmic Neutrino Background (CνB), a radiation analogous to the Cosmic Microwave Background (CMB) which decoupled at early stages of the Universe. The CνB formed well before the CMB, due to the weak nature of neutrino interactions, and it has a temperature given by the famous relation

$$T_\nu = \left(\frac{4}{11} \right)^{1/3} T_\gamma = (1.945 \pm 0.001) \text{K} . \quad (1.60)$$

This relation makes a precise prediction of the temperature of the neutrinos T_ν , connecting it with the photon temperature T_γ , which is accurately measured by CMB surveys. The temperature is equivalent to $T_\nu = (1.676 \pm 0.001) \times 10^{-4}$ eV and so at least two mass states of relic neutrinos are non-relativistic, comparing this energy to the measured mass differences from oscillation experiments. Neutrinos at these energies are almost impossible to detect with the current technologies. The density of relativistic neutrinos can be related to the density of photons, thanks to Eq. (1.60), and

$$\frac{\rho_\nu}{\rho_\gamma} = \frac{7}{8} \left(\frac{4}{11} \right)^{1/3} N_{\text{eff}} , \quad (1.61)$$

by which the energy density with respect to the critical density is

$$\Omega_{\nu_R} h^2 = \left(\frac{4}{11} \right)^{1/3} \Omega_\gamma h^2 , \quad (1.62)$$

with h the Hubble constant. When the neutrinos are non-relativistic, their energy density is given by $\rho_\nu \simeq \sum_i m_i n_i$, where n_i are the number density of each species which are equal to each other, up to negligible corrections from flavour effect. Using the expression of Eq. (1.61) and knowing the number density of photons n_γ , the total energy density of non-relativistic neutrinos today is

$$\Omega_{\nu_{\text{NR}}} h^2 = \frac{\sum_i m_i}{94.14 \text{ eV}} , \quad (1.63)$$

and the contribution of relativistic neutrinos to the total mass is also negligible. Due to the fact that the density of Eq. (1.63) can never be greater than the energy density of all matter in the Universe, a naive bound on the neutrino masses can be derived:

$$\sum_i m_i \lesssim 13 \text{ eV} . \quad (1.64)$$

The limit can be improved with more precise theoretical considerations under Λ CDM assumption, which combined with the latest cosmological surveys goes down to $\sum_i m_i \lesssim 0.12$ [?].

Other than cosmological neutrinos, these elusive fermions are produced and involved in a large variety of processes. They are emitted in astrophysical processes, such as supernova explosions, blazars, and in the nuclear reactions of the cores of stars. Cosmic ray interactions with the Earth's atmosphere also produces neutrino from decays of secondary mesons. Human-made sources include accelerator facilities in which neutrino beams are produced in a controlled environment, as well as those emitted by nuclear reactors. Neutrinos are also the products of β -decays, from the study of which neutrinos were first hypothesised. The study of the rare double- β decay is of utter importance, because the neutrinoless manifestation of this decay is a true lepton number violating process, the detection of which has deep and considerable connotation for neutrino mass theories.

In the following sections we discuss the most relevant sources relevant for the neutrino experiment mentioned in this thesis.

1.3.1 Solar and supernova neutrinos

Neutrinos produced in the core of the Sun were the first astrophysical source of neutrinos detected. They are yielded in thermonuclear reaction in the solar core. Being a G-type star in the main sequence, the Sun's energy is powered mostly from proton–proton (*pp*) chain and partly by the carbon–nitrogen–oxygen (CNO) cycle. In both these processes, the net result is the conversion of four protons and two electrons into an α -particle, of ${}^4\text{He}$ nucleus, and two neutrinos



along with the release of 26.731 MeV in the form of photons or kinetic energy of the neutrinos.

When a massive star at the end of its life collapses to a neutron star, it radiates almost all of its binding energy in the form of neutrinos, most of which have energies in the range 10 to 30 MeV, and are emitted over a timescale of several tens of seconds. These neutrinos are released just after core collapse, whereas the photon signal may take hours or days to emerge from the stellar envelope.

Stars that are at the onset of their collapse, just after carbon ignition, will release most of its energy through neutrinos. During the silicon burning stage, the neutrino luminosity is eight orders of magnitude less than in the peak at core-collapse, but while the later lasts just a few seconds, the Si burning phase takes several days. During the Si burning phase roughly 1% of the total energy of core-collapse are emitted through “pre-supernova” neutrinos with a monotonically increasing rate.

1.3.2 Atmospheric neutrinos

1.3.3 Reactor and accelerator neutrinos

Neutrino beams are derived from the decays of charged π and K mesons, which in turn are created from proton beams striking thick nuclear targets. The precise selection and manipulation of the π/K beam control the energy spectrum and type of neutrino beam.

The π^\pm mesons have a mass of 139.6 MeV and a mean lifetime of 2.6×10^{-8} s. The primary decay mode of a pion, with a branching fraction of 99.9877 %, is a leptonic decay into a muon and a muon neutrino:

$$\pi^+ \rightarrow \mu^+ + \nu_\mu \quad (1.66)$$

$$\pi^- \rightarrow \mu^- + \bar{\nu}_\mu \quad (1.67)$$

The second most common decay mode of a pion, is the leptonic decay into an electron and the

corresponding neutrino, $\pi^\pm \rightarrow \nu_e + e$. In spite of the considerable differences in the space momentum, this process is suppressed with respect to the muonic one. This effect is called *helicity suppression* and is due to the great mass of the muon ($m_\mu = 105.658$ MeV) compared to the electron's ($m_e = 0.510$ MeV); this results in a stronger helicity-chirality correspondence for the electron rather than for the muon. Given that the π mesons are spinless, neutrinos are left-handed, and antineutrinos are right-handed, the muonic channel is preferred because of spin and linear momentum preservation. The suppression of the electronic decay mode with respect to the muonic one is given approximately within radiative corrections by the ratio:

$$R_\pi = \left(\frac{m_e}{m_\mu} \right)^2 \left(\frac{m_\pi^2 - m_e^2}{m_\pi^2 - m_\mu^2} \right) = 1.283 \times 10^{-4} \quad (1.68)$$

The measured branching ratio of the electronic decay is indeed $(1.23 \pm 0.02) \times 10^{-4}$.

As far as the charged K meson is concerned, it mainly decays in a muon and its corresponding neutrino, with a branching ratio of 63.55 %:

$$K^+ \rightarrow \mu^+ + \nu_\mu \quad (1.69)$$

$$K^- \rightarrow \mu^- + \bar{\nu}_\mu \quad (1.70)$$

The second most frequent decay (20.66 %) is the decay into two pions, $K^\pm \rightarrow \pi^0 + \pi^\pm$. Other decays have a branching ratio of 5 % or less and are listed in table Tab. 1.1. On the contrary, the decays of the neutral kaon produce neutrino in few cases. Because of the oscillation phenomenon given by the mixing between K^0 and \bar{K}^0 , the neutral kaon has two manifestations, the short kaon K_S and the long kaon K_L , named after their lifetimes. While the K -short decays only in two pions ($2\pi^0$ or $\pi^+ + \pi^-$), the K -long has a wider variety of final state combination, all of them involving three particles. Among these, neutrinos are produced in the processes:

$$K_L^0 \rightarrow \pi^\pm + \mu^\mp + \overset{(-)}{\nu}_\mu \quad (1.71)$$

$$K_L^0 \rightarrow \pi^\pm + e^\mp + \overset{(-)}{\nu}_e \quad (1.72)$$

Neutrinos are also produced by the decay of muons. Muons are unstable elementary particles and decay via the weak interaction. The dominant decay mode, called *Michel decay*, is also the simplest possible: because lepton numbers must be conserved, one of the product neutrinos of muon decay must be a muonic neutrino and the other an electronic antineutrino, along with an electron, because of the charge preservation. Vice versa, an antimuon decay produces the corresponding antiparticles. These two decays are:

Tab. 1.1: Decay mode for a charged kaon, K^\pm , sorted by branching ration (in percent).

$\mu^\pm + \overset{(-)}{\nu}_\mu$	65.55 ± 0.11
$\pi^\pm + \pi^0$	20.66 ± 0.08
$\pi^+ + \pi^\pm + \pi^-$	5.59 ± 0.04
$\pi^0 + e^\pm + \overset{(-)}{\nu}_e$	5.07 ± 0.04
$\pi^0 + \mu^\pm + \overset{(-)}{\nu}_\mu$	3.35 ± 0.03
$\pi^\pm + \pi^0 + \pi^0$	1.76 ± 0.02

$$\mu^- \rightarrow e^- + \bar{\nu}_e + \nu_\mu \quad (1.73)$$

$$\mu^+ \rightarrow e^+ + \nu_e + \bar{\nu}_\mu \quad (1.74)$$

1.4 Neutrino interactions

Neutrino interactions in their flavour states are described by Eqs. (1.14) and (1.15). Replacing the values of g_V^ν and g_A^ν for a neutrino, the relevant lagrangian terms are

$$\mathcal{L}_{\text{CC},\nu} = -\frac{g}{2\sqrt{2}} \sum_{\alpha=e,\mu,\tau} \bar{\nu}_\alpha \not{W} (1 - \gamma^5) \ell_\alpha + \text{h.c.} \quad (1.75)$$

$$\mathcal{L}_{\text{NC},\nu} = -\frac{g}{4 \cos \vartheta_W} \sum_{\alpha=e,\mu,\tau} \bar{\nu}_\alpha \not{Z} (1 - \gamma^5) \nu_\alpha . \quad (1.76)$$

For energies below the W and Z mass, the allowed tree-level interactions involving at least one neutrino are any allowed variation of the processes represented in Fig. 1.1. The vector bosons cannot be produced on-shell and so their field operator must contract with some other external field. The amplitudes of the processes shown in Fig. 1.1 are

$$i\mathcal{M}_{\text{CC}} = i \frac{g^2}{8} \bar{u}_{\ell_\alpha} \gamma^\mu (1 - \gamma^5) u_{\nu_\alpha} \frac{\eta_{\mu\nu}}{k^2 - m_W^2 + i\varepsilon} \bar{u}_{f_2} \gamma^\nu (1 - \gamma^5) V_{12} u_{f_1} \quad (1.77)$$

$$i\mathcal{M}_{\text{NC}} = i \frac{g^2}{8 \cos \vartheta} \bar{u}_{\nu_\alpha} \gamma^\mu (1 - \gamma^5) u_{\nu_\alpha} \frac{\eta_{\mu\nu}}{k^2 - m_Z^2 + i\varepsilon} \bar{u}_f \gamma^\nu (g_V^f - g_A^f \gamma^5) u_f , \quad (1.78)$$

where k is the momentum of the propagator and V_{12} a possible mixing between generic fermions f_1 and f_2 . Because of the typical energies involved, the momentum propagating between the particles is small compared to the masses of the intermediate bosons and therefore this mass is typically factorised out,

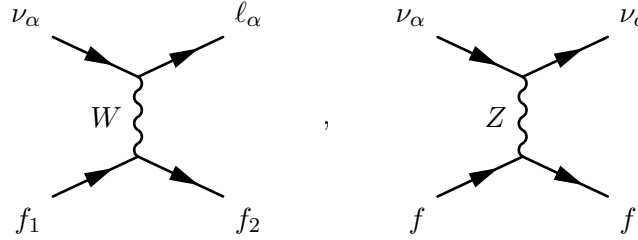


Fig. 1.1: Generic CC (right) and NC (left) tree-level interactions with neutrinos involved. Note that these diagrams have illustration purpose only, and that's why time flow convention is not respected.

resulting in

$$i\mathcal{M}_{\text{CC}} \simeq i \frac{G_F^2}{\sqrt{2}} \bar{u}_{\ell_\alpha} \gamma^\mu (1 - \gamma^5) u_{\nu_\alpha} \bar{u}_{f_2} \gamma^\mu (1 - \gamma^5) V_{12} u_{f_1} \quad (1.79)$$

$$i\mathcal{M}_{\text{NC}} \simeq i \frac{G_F^2}{\sqrt{2}} \bar{u}_{\nu_\alpha} \gamma^\mu (1 - \gamma^5) u_{\nu_\alpha} \bar{u}_f \gamma^\mu (g_V^f - g_A^f \gamma^5) u_f , \quad (1.80)$$

where the relation in Eq. (1.28) was used and a new constant was introduced

$$\frac{G_F}{\sqrt{2}} = \frac{g^2}{8 m_W^2} . \quad (1.81)$$

The constant in Eq. (1.81) is called Fermi's constant and the interactions can be described by effective four-point Lagrangians.

In the following sections we will review the most important neutrino interactions with matter, from low to higher energies

1.4.1 Coherent elastic neutrino–nucleus scattering

1.4.2 Neutrino–electron scattering

The easiest interaction to study between neutrinos and matter components at low energies is the neutrino–electron elastic scattering

$${}^{(-)}\nu_\alpha + e^- \rightarrow {}^{(-)}\nu_\alpha + e^- . \quad (1.82)$$

For the electron neutrino ν_e , both CC and NC interactions are allowed and for the electron antineutrino $\bar{\nu}_e$ the s -channel and t -channel diagrams are swapped, whereas for $\alpha = \mu, \tau$ only neutral-current interactions exist. Using the effective four-point Lagrangians, one can calculate the differential cross-sections in the laboratory frame with an initial electron at rest:

$$\frac{d\sigma}{dq^2} = \frac{G_F^2}{\pi} \left[\kappa_1^2 + \kappa_2^2 \left(1 - \frac{q^2}{2(p_\nu \cdot p_e)} \right)^2 - \kappa_1 \kappa_2 m_e^2 \frac{q^2}{2(p_\nu \cdot p_e)^2} \right] , \quad (1.83)$$

where $-q^2 = t$ and the quantities κ_1 and κ_2 depend on the neutrino flavour and embeds CC and NC contributions. Using the vector and axial coupling of Eq. (1.17) they read

$$\begin{aligned}\kappa_1^{\nu_e} &= \kappa_2^{\bar{\nu}_e} = 1 + \frac{g_V^\ell + g_A^\ell}{2} = \frac{1}{2} + \sin^2 \vartheta_W \\ \kappa_2^{\nu_e} &= \kappa_1^{\bar{\nu}_e} = \frac{g_V^\ell - g_A^\ell}{2} = \sin^2 \vartheta_W \\ \kappa_1^{\nu_{\mu,\tau}} &= \kappa_2^{\bar{\nu}_{\mu,\tau}} = \frac{g_V^\ell + g_A^\ell}{2} = -\frac{1}{2} + \sin^2 \vartheta_W \\ \kappa_2^{\nu_{\mu,\tau}} &= \kappa_1^{\bar{\nu}_{\mu,\tau}} = \frac{g_V^\ell - g_A^\ell}{2} = \sin^2 \vartheta_W .\end{aligned}$$

The variable t is the squared difference between the four-momentum of the initial and final electrons, and denoting $T_e = E_e - m_e$ as the kinetic energy of the outgoing electron, we see that

$$-t = q^2 = 2 m_e T_e . \quad (1.84)$$

With some simple kinematics the kinetic energy is found to be

$$T_e = \frac{2 m_e E_\nu^2 \cos^2 \theta}{(m_e + E_\nu)^2 - E_\nu^2 \cos^2 \theta} , \quad (1.85)$$

and so the differential cross-section in Eq. (1.83) can be given as a function of the electron scattering angle θ with respect to the incoming neutrino with energy E_ν :

$$\begin{aligned}\frac{d\sigma}{d \cos \theta} &= \frac{2 G_F^2 m_e}{\pi} \frac{4 E_\nu^2 (m_e + E_\nu)^2 \cos \theta}{[(m_e + E_\nu)^2 - E_\nu^2 \cos^2 \theta]^2} \times \\ &\left[g_1^2 + g_2^2 \left(1 - \frac{2 m_e E_\nu \cos^2 \theta}{(m_e + E_\nu)^2 - E_\nu^2 \cos^2 \theta} \right)^2 - g_1 g_2 \frac{2 m_e^2 \cos^2 \theta}{(m_e + E_\nu)^2 - E_\nu^2 \cos^2 \theta} \right] .\end{aligned} \quad (1.86)$$

1.4.3 Neutrino scattering with nucleons

Neutrinos can also interact with hadrons in matter, namely proton and neutrons, as the quark components of these baryons couple to the W and Z vector bosons according to the currents of Eqs. (1.37) and (1.38). Even though In general, these processes can be categorised according to the momentum transfer. At small q^2 , elastic interactions dominate and may be brought about by both charged and neutral currents. When this occurs via neutral currents, all flavour of neutrinos and anti-neutrinos can scatter off both neutrons and protons in what is referred to as “NC elastic” scattering. The process is:



Once neutrinos acquire sufficient energy they can also undergo the analogous charged current interactions, called “quasi-elastic”, due to the fact that the recoiling nucleon changes its charge and mass transfer occurs. The processes are

$$\nu_l + n \rightarrow p + l^- \quad (1.89)$$

$$\bar{\nu}_l + p \rightarrow n + l^+ , \quad (1.90)$$

with $l = e, \mu, \tau$. For the muonic neutrino with energy below one GeV, the CCQE is the dominant interaction, even though the cross-section plateaus at higher energies, as the available Q^2 increases: it becomes increasingly unlikely for the nucleon to remain intact.

The physics behind the CC quasi-elastic processes is more complicated. The differential cross-section for the scattering in the laboratory frame is given by

$$\frac{d\sigma_{CC}}{dQ^2} = \frac{G_F^2 |V_{ud}|^2 m_N^4}{8\pi(p_\nu \cdot p_N)^2} \left[A(Q^2) \pm B(Q^2) \frac{s-u}{m_N^2} + C(Q^2) \frac{(s-u)^2}{m_N^4} \right], \quad (1.91)$$

where the plus sign refers to the $N = n$ interactions, while the minus sign to $N = p$.

$$\frac{d\sigma_{CC}}{d \cos \theta} = -\frac{G_F^2 |V_{ud}|^2 m_N^2}{4\pi} \frac{p_l}{E_\nu} \left[A(Q^2) \pm B(Q^2) \frac{s-u}{m_N^2} + C(Q^2) \frac{(s-u)^2}{m_N^4} \right], \quad (1.92)$$

The functions $A(Q^2)$, $B(Q^2)$, and $C(Q^2)$ depends on the nucleon form-factors in the following way:

$$A = \frac{m_l^2 + Q^2}{m_N^2} \left\{ \left(1 + \frac{Q^2}{4m_N^2} \right) G_A^2 - \left(1 - \frac{Q^2}{4m_N^2} \right) \left(F_1^2 - \frac{Q^2}{4m_N^2} F_2^2 \right) + \frac{Q^2}{m_N^2} F_1 F_2 - \frac{m_l^2}{4m_N^2} \left[(F_1 + F_2)^2 + (G_A + 2G_P)^2 - \frac{1}{4} \left(1 + \frac{Q^2}{4m_N^2} \right) G_P^2 \right] \right\} \quad (1.93)$$

$$B = \frac{Q^2}{m_N^2} G_A (F_1 + F_2) \quad (1.94)$$

$$C = \frac{1}{4} (G_A^2 + F_1^2 + \frac{Q^2}{4m_N^2} F_2^2). \quad (1.95)$$

The form factors $F_1(Q^2)$, $F_2(Q^2)$, $G_A(Q^2)$, and $G_P(Q^2)$ are called, respectively, *Dirac*, *Pauli*, *axial*, and *pseudoscalar* weak charged-current form factors of the nucleon. These functions of Q^2 describe the spatial distributions of electric charge and current inside the nucleon and thus are intimately related to its internal structure.

CCQE interactions are particularly important to neutrino physics for mainly two reasons:

- measurements of the differential cross-section in Eq. 1.91 give information on the nucleon form-factors, which are difficult to measure;
- their nature as two-body interactions enable the kinematics to be completely reconstructed, and hence the initial neutrino energy determined which is critical for measuring the oscillation parameters.

eters.

In fact, if the target nucleon is at rest, at least compared to the neutrino energy, then this can be calculated as:

$$E_\nu = \frac{m_n E_l + \frac{1}{2}(m_p^2 - m_n^2 - m_l^2)}{m_n - E_l + p_l \cos \theta_l}, \quad (1.96)$$

where the measurement of the momentum, p_l and the angle with respect to the neutrino, θ_l , of the outgoing charged lepton are only required.

Similar calculations can be made for the NCQE scatterings. The cross-sections have the same form as the CC cross-sections in Eq. 1.91 and 1.92, without the mixing term $|V_{ud}|^2$ and with the proper nucleon form factors. Since the values of the electromagnetic form factors, F_1 and F_2 , are reasonably well known and the part in Eq. 1.93 containing G_P can be often neglected, thanks to the different mass magnitudes of leptons and nucleons, the axial form factor, G_A , can be determined through measurements of the charged-current quasielastic scattering processes. On the contrary, measurements of the neutral-current elastic scattering cross-section give information on the *strange* form factors of the nucleon, whose main contribute comes from the strange quark.

The low Q^2 region also presents an inelastic scattering contribution mostly affected by resonance production, where the nucleon is excited into a baryonic resonance before decaying. At high Q^2 , inelastic scattering is dominated by deep inelastic scattering (DIS), because the neutrino can scatter directly off a constituent quark, fragmenting the original nucleon. In between these extreme scenarios, an additional contribution comes from interactions where the hadronic system is neither completely fragmented nor forms a recognisable resonance. These interactions are referred to as “shallow inelastic scattering”, and there is no clear model for dealing with them.

Chapter 2

The gadolinium phase of Super-Kamiokande

As studied in the previous chapter, the typical total cross-section for an accelerator neutrino ($\sim 1 \text{ GeV}$) is of the order of 10^{-38} cm^2 and for a solar neutrino ($\lesssim 10 \text{ MeV}$) it is one order of magnitude lower. These small values make the detection of neutrinos a challenging task. Neutrino experiments usually compensate the small cross-section by instrumenting large active volumes, so that a statistically significant amount of neutrino interactions with matter can be recorded. By studying the final state particles some knowledge on the incoming neutrino may be retrieved. Large volumes are, however, prone to higher background, either from cosmic rays or natural radioactivity. and passive or active techniques to reduce such undesired events must be put into place. Neutrino physics has greatly progressed in recent times, thanks to both massive active detectors and improvements in the detection technologies. The most emblematic example of neutrino experiments are SNO and Super-Kamiokande (SK) which respectively demonstrated solar [1] and atmospheric [2] neutrino oscillations. The picture of three-flavour neutrino oscillations has been since intensively studied by numerous experiments with not only atmospheric and solar neutrinos, but also with neutrinos from reactors and accelerators. Current and future neutrino experiments rely on the experimental techniques that were pioneered and perfected by these two successful experiments.

SK and SNO are both water Cherenkov detectors, in which a large body of water is surrounded by photodetectors to capture Cherenkov radiation emitted by the charged leptons produced in neutrinos CC and NC interactions. The volumes of SNO and SK are located in mines so as to take advantage of the thick rock overburden, which acts as a passive shield to cosmic muons. An outer detector system provides a passive and active veto to the fiducial region in both experiment. These simple measurements are responsible for the suppression of the majority of background. The most difficult background to control is given by neutrons, which are typically produced by spallation events induced by cosmic rays or by the decay chains of radioactive elements—such as uranium and thorium—naturally present in the

detector's components. As we are entering a precision era for neutrino experiments, the capability of tagging neutron events is becoming a more and more crucial requisite for detectors. One of the most promising approach is the addition of gadolinium to the active medium of the detector. Certain isotopes of gadolinium (Gd) have a very high cross-section for thermal neutron capture accompanied with the emission of high energy photons, which makes neutron detection more efficient. Many existing neutrino experiments are already using Gd-loaded water or scintillator for neutron tagging (EGADS, ANNIE, RENO), and future experiments are planning to use the same principle. After a summer-long refurbishment in 2018, Super-Kamiokande will become the largest Gd-doped water Cherenkov detector.

In this chapter, we will review the working principle of a generic Cherenkov detector in Section 2.1, before illustrating in more detail the Super-Kamiokande experiment (Section 2.2). We will then justify the importance for neutron tagging in Section 2.3 and the benefits of gadolinium-doping (Section 2.4 and Section 2.5).

2.1 Cherenkov detectors

Light travelling through a transparent material undergoes a reduction of its phase velocity due to a superposition with the electromagnetic fields of the electrons in the medium. The change in velocity will therefore depend on the frequency of the incoming photons. The ratio of the new phase velocity and the speed of light in vacuum defines the *refractive index* of the material:

$$n(\lambda) = \frac{c}{v_P(\lambda)} , \quad (2.1)$$

which by definition is greater than one.

A charged particles moving at a velocity faster than the speed of light in a medium emits a coherent electromagnetic radiation, called *Cherenkov radiation*. As the particle is moving faster than c/n , the front wave of the EM radiation forms a cone which follows behind the charged particle. Provided that the length of the track of the particle in the medium is large compared to the emitted wavelength and that the speed of the particle is constant with respect to the period of emission $\tilde{t} = \frac{\lambda}{c}$, the radiation is produced when

$$\beta = \frac{v}{c} > \frac{1}{n} , \quad (2.2)$$

where v is the velocity of the particle. The minimum energy of the particle to reach this condition is therefore

$$E_{\text{thr}} = m \sqrt{1 + \frac{1}{n^2 - 1}} , \quad (2.3)$$

with m the mass of the charged particle. Particles of mass m with energy above the threshold will

radiate Cherenkov light in the shape of a cone, which has an angular aperture θ given by

$$\cos \theta = \frac{1}{n\beta} . \quad (2.4)$$

The maximum angle is reached by ultra-relativistic particle with $\beta \simeq 1$. The charged particle, however, will typically lose energy in the medium due to ionization, slowing down until its energy falls below the threshold E_{thr} . As soon as the condition of Eq. (2.3) does not hold anymore, the particle stops emitting radiation and the cone of light reduces to a truncated cone, which forms a ring when projected onto a surface.

Many particle phsyics experiments take advantage of this effect, in order to convert the passage of charged particles into detectable light. A volume of transparent material, such as water, ice, aerogel, or a liquid scintillator, can be instrumented with photodetectors to capture the Cherenkov radiation. The number of photons emitted by a charged particle of charge z per unit path length and per unit energy interval, or equivalently to λ , has a distribution that follows the Frank-Tamm formula:

$$\frac{\partial^2 N}{\partial x \partial \lambda} = \frac{2\pi\alpha z^2}{\lambda^2} \left(1 - \frac{1}{\beta^2 n^2(\lambda)}\right) = \frac{2\pi\alpha z^2}{\lambda^2} \sin^2 \theta , \quad (2.5)$$

where α is the fine structure constant and z is the charge of the particle.. Due to the inverse dependence on λ^2 , most of the Cherenkov photons are emitted at shorter wavelengths. A real medium is always dispersive and allowed frequencies are restricted to the region for which $n(\lambda) > \frac{1}{\beta}$. The radiation is hence typically emitted in the near visible and ultraviolet regions of the EM spectrum. At higher frequencies, for example in the x-ray region, the refractive index drops below one and Cherenkov photons cannot be produced at such short wavelengths. Experiments exploiting Cherenkov light try to match the sensitivity band of photodetectors to the radiation region. Photomultipliers (PMT) are the detectors of choice, thanks to their low noise and capability of single photodetection, but silicon photomultipliers (SiPM) are also employed.

This technique is largely used in neutrino detection, since it allows to easily transform large volumes of some transparent medium into a detector sensitive to charged particles. Amongst the most notable examples, the IceCube experiment is the largest Cherenkov detector, in which more than five thousands PMTs are deployed into the Antarctic ice, covering a volume of one cubic kilometer. Charged-current interactions of neutrinos on a nucleon produce charged leptons that are likely to acquire most of the incoming neutrino momentum thanks to the heavy mass of the nucleon. If the outgoing lepton has sufficient energy above the threshold of Eq. (2.3), the emitted radiation can be collected and used to reconstruct the interacting neutrino, with some limited resolution. The photons collected on the light sensors are correlated to the particle's energy, whereas the location and timing of the hit photodetectors is used to reconstruct the vertex and the direction of the interaction. Certain Cherenkov detectors are also capable of particle identification. In IceCube, for example, events are classified in the following

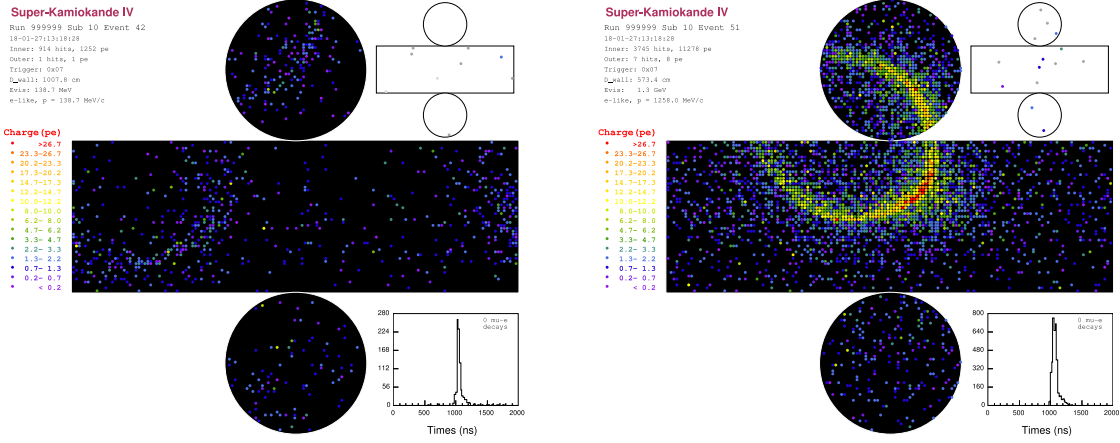


Fig. 2.1: Fully-contained events in the fiducial volume of Super-Kamiokande.

categories: “cascades”, typically generated by CC interactions of ν_e or NC interactions; “tracks”, produced by very energetic muons; “double bangs”, the results of a ν_τ producing a tau lepton, which decays inside the detector.

2.2 The Super-Kamiokande experiment

The Super-Kamiokande experiment (SK) is a water Cherenkov detector, located in the Kamioka mine, under Mt. Ikeno in the Gifu prefecture, Japan. The rock overburden of ~ 1000 m (2700 m.w.e.), shields very efficiently the experiment and only cosmic-rays with energies above 1.3 TeV can reach the detector: the muon flux at SK is about $6 \times 10^{-8} \text{ cm}^{-2}\text{s}^{-1}\text{sr}^{-1}$, which translates to a rate of 2 Hz. The detector consists of a cylindrical stainless steel tank, with a height of 41.4 m and a diameter of 39.3 m, and it is filled with 50 kt of ultra pure water (18 MΩ). The water region is separated into two concentric cylindrical regions, called the inner detector (ID, 33.8 m in diameter) and the outer detector (OD), the latter working as passive and active veto. The two regions are separated a 55 cm insensitive region containing the support structure for the PMTs and their cables. The ID is instrumented with 11,129 20" Hamamatsu R3600 PMTs, facing towards the inside of the tank. Since the 2001 implosion accident, the photocathode of the PMTs are protected by UV-transparent acrylic domes and the side with fiber-reinforced plastic. The photo coverage of the inner surface is around 40 %; the remaining surface not occupied by a PMT is lined with black sheet to reduce light reflection. The main goal of the OD is to tag events originating or finishing outside the ID. It is instrumented with 1885 8" Hamamatsu R1408 PMTs which are optically coupled to wavelength shifting plates to increase light collection to increase light collection. Sheets of white tyvek maximise the propagation of photons inside the ID and helps the reconstruction of corner-clipping events.

The refractive index of water in the visible and ultraviolet region is $n \geq 1.33$, and so a charged particle can emit Cherenkov radiation if it is travelling with speed $\beta \gtrsim 0.75$. This converts to an energy threshold of 0.78 MeV for electrons, 160.26 MeV for muons, 211.69 MeV for pions, and 1423.13 MeV for protons,

which are the particles usually detected in SK. The Cherenkov photons, thanks to the high-purity water, reach the walls of the tank where they are collected by the PMTs, forming ring patterns. From the time and charge deposited on the PMTs, the event reconstruction algorithm extracts information of the event such as vertex, direction, and energy. The same algorithm performs particle identification by looking at the topology and the multiplicity of the ring patterns: for example, an electron travelling in the water is more likely to be scattered compared to a muon, that on the other hand will follow a more straight path, and as a consequence the electron-induced ring is less defined and fuzzier than the muon-induced one. This can be appreciated on the reconstructed events of Fig. 2.1. Pions usually interact hadronically nuclei with oxygen nuclei, and therefore they have shorter and the Cherenkov rings are also less defined than a muon ones. Muon and pion events can be accompanied by secondary rings from the electrons produced in their decays. Energetic gamma rays can also be detected, as for instance the ones from π^0 decays, through rings of electrons accelerated by compton scattering.

As part of the strategies to tackle backgrounds, typically only events originating at the centre of the ID are considered to be valid. The materials of the walls of the tank, and particularly the glass of PMTs, contains radioactive material, such as isotopes of thorium, uranium and potassium. These impurities can mimic a signal event in the MeV energy region, crucial for solar neutrino studies. The selection algorithm simply discards any reconstructed event the vertex of which is less than 200 cm away from the ID walls. This criteria defines a fiducial volume (FV), which is around 22.5 kt in water mass. The water used to fill the tank may also contain impurities, among which radon, that cause background events. The water in the tank is continuously filtered at a flow rate of 60 t/hour by a water purification system. An air purification system pumps radon-free air into the SK area inside the mine. This prevents radon in the air to dissolve in the purified water. Radon contamination is usually less than 3 mBq/m³, compared to unpurified air that can peak at about 1200 Bq/m³. Thanks to these precautions the current energy threshold for SK is 3.5 MeV. The main oscillation analyses of SK consider only events originating inside the FV and fully-contained, i.e. that do not propagate in the OD, as this is signature is given mostly by neutrino interactions.

2.3 Neutrons in Super-Kamiokande

Super-Kamiokande and other large scale water Cherenkov detectors have provided many evidences in the experimental understanding of neutrinos, be it originated in solar, atmospheric, or accelerator facilities. Despite the large exposure of the experiment, some studies are still curbed by statistical uncertainty and would benefit from simply collecting more data. Other searches, instead, suffer from irreducible background events, as for example the detection of Relic Supernova Neutrinos (SNR), also known as Diffuse Supernova Neutrino Background (DSNB), an incoherent background spectrum produced from all previous core-collapse supernova explosions in the Universe (see Section 1.3.1). The observation

of SNR would be of great importance for improving our knowledge on the population of core-collapse SN and the rate of star formation. The predictions provide with several limits but although SK has the best world limit, no SRN has been detected yet. The average energies of these neutrinos are around a few tens of MeV, at which the largest cross-section corresponds to inverse beta decay (IBD, see Section ??). This measurement is afflicted at low energies by invisible muon decay—muons below Cherenkov threshold that decay into electrons—and at high energies, between $14 \text{ MeV} < E_\nu < 30 \text{ MeV}$, by atmospheric neutrinos. The energy threshold is also limited by muon-induced spallation events and solar neutrinos, that could be successfully rejected with neutron tagging. If we could detect neutrons efficiently, these backgrounds could be reduced significantly and thus, making the detection of the DSNB possible for the first time.

Searches of galactic supernova burst could also avail of an improved background suppression. SK will be exposed to a huge number of neutrino events if a core-collapse supernova occurs inside our galaxy, providing not only an early warning system for other observatories (see Section ??), but also information about the neutrino spectrum, time profile, and information about early stages of the core-collapse process, such as pre-supernova neutrinos from the silicon burning phase [?]. The majority of neutrinos emitted are actually antineutrinos in the energies where IBD cross-section dominates. Detecting the neutron in the final state can be fundamental in distinguishing whether the incoming particle is a neutrino or an antineutrino.

Improved neutron tagging is also helpful to understand atmospheric and accelerator neutrino interactions and final states. At energies $E_\nu > 1 \text{ GeV}$, the number of CCQE interactions decreases and often additional neutrons or pions are also released by secondary hadronic interaction. The capability of separating neutrinos and antineutrinos can still produce anti-neutrino enriched samples. Finally, the background in proton decay searches can be reduced, since it requires no neutrons to appear in the final state.

2.3.1 Neutron tagging

Neutrons have a relative long lifetime and since they cannot directly emit Cherenkov radiation, these particles can travel quite some distance from they production point. Neutrons interact with nuclei in various way, depending on their energy and the target nucleus. The interactions are divided in three typologies: scattering, which can elastic or inelastic, absorptions, such as radiative capture or fission, and nucleon transfer reactions. The kinetic energy of the neutron T , sometimes referred to as the *detection temperature*, is the main factor in determining the dominant cross-section of these interactions. For fast neutrons, with $T > 1 \text{ MeV}$, elastic scattering is the dominant interaction mode, and for some target nuclei the only mode possible. The cross-section for these energetic neutrons presents some wide resonance peaks which depend on the target nuclei. The elastic scattering cross-sections at energies below 1 MeV is almost independent of the neutron energy. This is true for most light isotopes, but some

intermediate and heavy elements presents some specific behaviour at higher energy. Neutrons for which $T \simeq 0.0025$ eV are called *thermal neutrons* because a Maxwell-Boltzmann distribution at a temperature 290 K peaks at that energy; such neutrons are therefore in thermal equilibrium with the surrounding medium. At thermal energies and below the most important interaction is neutron absorption and the cross-section follows the “ $1/v$ law”, with v the velocity of the neutron. In this region, absorption cross-section increases as the velocity, or the detection temperature, of the neutron decreases

$$\sigma \sim \frac{1}{v} \sim \frac{1}{T} \quad (2.6)$$

Being in thermal equilibrium and having a lower kinetic energy allows the neutron to form a compound nucleus with the target, which might undergo fission or radiation emission if it is a non-fissile nuclide. For energies between a few eV and hundreds of keV, resonances in the capture cross-section occurs and these are strongly dependent on the target isotope, but also on the temperature of the material. The thermal motions of the target relative to the incident neutron broadens the resonance peaks, despite the integrated cross-section over the energy remains constant. This effect is called *Doppler broadening*, and results in a decreased likelihood of capture or fission when the target material has a wide energy distribution.

Fast neutrons slow down to thermal energies via subsequent elastic collisions, until the free neutron is captured by some nuclei. This process is called *thermalisation*. Considering a scattering between a neutron and a nucleus, $n + A \rightarrow n + A$, the final state energy of the neutron depends on the outgoing angle $\hat{\theta}$ in the centre of mass frame

$$E_f = E_i \frac{(1 + \zeta) + (1 - \zeta) \cos \hat{\theta}}{2}, \quad (2.7)$$

where $E_{i,f}$ are the initial and final energies of the free neutron and ζ is the following kinematic factor

$$\zeta = \frac{(m_n - M_A)^2}{(m_n + M_A)^2} \simeq \frac{(1 - A)^2}{(1 + A)^2}. \quad (2.8)$$

Using classic mechanics, in the laboratory frame the scattering angle θ is given by

$$\cos \theta = \frac{A \cos \hat{\theta} + 1}{\sqrt{1 + 2 A \cos \hat{\theta} + A^2}}, \quad (2.9)$$

and we can therefore estimate the average scattering angle

$$\langle \cos \theta \rangle = \frac{\int d\Omega \cos \theta}{\int d\Omega} = \frac{2}{3A}. \quad (2.10)$$

Heavy targets will deviate on average more the neutron from its path than light targets. For hydrogen

($A = 1$), the average angle is $\langle \theta \rangle \simeq 48^\circ$, but for heavier elements with large atomic mass, the average angle approximate $\langle \theta \rangle \rightarrow 90^\circ$. Assuming uniform isotropic scattering, the average outgoing energy for the neutron is

$$\langle E_f \rangle = \frac{\int d\Omega E_f}{\int d\Omega} = E_i \frac{1 + \zeta}{2}. \quad (2.11)$$

This means that if each neutron collision decreases to the same average final state energy, after n interactions the neutron energy is

$$E_n = E_0 \left(\frac{1 + \zeta}{2} \right)^n = E_0 e^{-n\xi}. \quad (2.12)$$

The thermalisation process follows an exponential law, and ξ represents the typical energy decrease in log-scale, which on average equals to

$$\langle \xi \rangle = \frac{\int d\Omega \log \left(\frac{E_i}{E_f} \right)}{\int d\Omega} = \frac{\zeta - \zeta \log \zeta - 1}{\zeta - 1} = 1 + \frac{(A - 1)^2}{2A} \log \frac{A - 1}{A + 1}. \quad (2.13)$$

With the expression, we can compute the average number of collisions a neutron undergoes when propagating in a medium. Because of the dependency of ξ on A , lighter nuclides are more effective than heavier ones. For example, the number of interactions for a fast neutron to slow down to thermal energies in lead ($A = 208$) is about hundred times the number of interactions that would occur in hydrogen. In reality, the media in which neutrons propagate are compounds with more than one type of target. The energy decrease for these materials is an average of the individual components weighted by their respective elastic cross-sections

$$\xi_{\text{tot}}(E) = \frac{\sum_k \sigma_k(E) \xi_k(E)}{\sum_k \sigma_k(E)}. \quad (2.14)$$

In this simplified scenario we overlooked the impact of resonance capture, which manifests at around the keV energy range. While fast neutrons with energies above 1 MeV are being slowed down to thermal energies, the mean free path decreases with the neutron's velocity, and the possibility of resonance capture increases. These captures would affect the relative neutron flux around the energy of the resonance peaks, which might be widened by the Doppler broadening effect.

From the considerations above, we can deduce that water is a good moderator for thermalising fast neutrons. The energy decrease for water is $\xi_{\text{H}_2\text{O}} \simeq 0.93$, when the kinetic energy of the neutron is in the range $2.5 \text{ meV} \lesssim T \lesssim 0.1 \text{ MeV}$. Neutrons that reach sub-thermal energies enter the $1/v$ regions in which the capture probabilities increases as T^{-1} . Hydrogen presents a relative high cross-section for neutron capture, as it can be seen from Fig. 2.2: the cross-section for a thermal neutron on hydrogen is measured to be 332.6 mb [3]. The cross-section of capture on the oxygen nucleus ^{16}O is around 0.19 mb, four orders of magnitude smaller than the capture on hydrogen. The hydrogen capture is followed by the

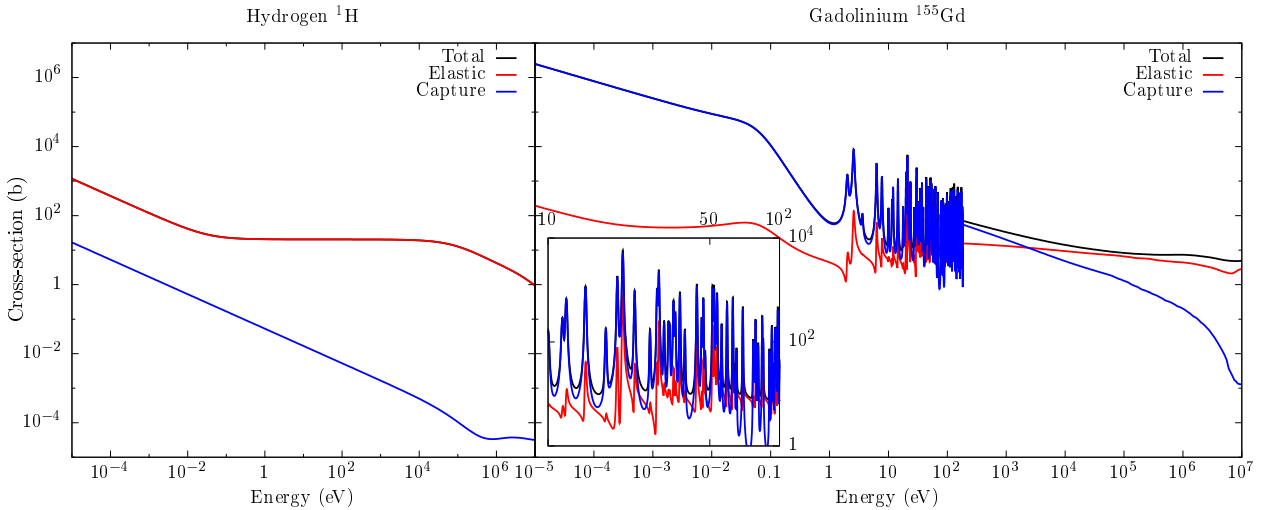


Fig. 2.2: Neutron cross-sections on hydrogen (left) and gadolinium (right) as a function of energy. The dominant component for ^1H is elastic scattering, despite neutron capture reaches relative high cross-section values for sub-thermal neutrons ($T < 2.5 \text{ meV}$). Fast neutrons interact on ^{155}Gd via elastic scattering, but for lower energies the main contribution comes from neutron capture cross-section. The $1/v$ dependency can be appreciated in both cases. The inset shows a detail of the resonance region of the cross-section, between 10 eV and 100 eV.

emission of a 2.2 MeV gammas from the deexcitation of the newly-formed deuterium. The characteristic time for Maxwellian neutrons with energy below 10 MeV to thermalise and being captured by hydrogen in water has been measured to be $(204.8 \pm 0.4) \mu\text{s}$ [?]. The typical time and energy of this event require special triggers and dedicated analysis to correctly identify the neutron capture on hydrogen in SK. Since the SK-IV phase, after any primary events above a fixed, higher threshold is detected, a time window of $535 \mu\text{s}$ is saved with no threshold requirement, so that approximately the 92 % of neutron capture signals are collected. The 2.2 MeV γ , on average, produces 7~8 PMT hits, which are difficult to reconstruct accurately. The PMT hits are expected to happen in a narrow timing distribution and to be anisotropic. A 10 ns sliding window is used to look for γ candidates with more than 7 hits and less than 50 to avoid high energy backgrounds. With these simple selection criteria, an efficiency of 33.2 % is obtained from a simulation of neutron capture events, with an expected 4.5 background events per neutrino event. The background rejection is improved by feeding the simulated data of the selected candidates to a neural network, which retains an overall efficiency of 20.5 % with 0.018 backgrounds per signal event [?]. The efficiency is found to be highly dependent on the distance travelled by the released neutron, due to the fact that knowing the location of the capture significantly reduce the background.

2.3.2 Neutron calibration

Neutron tagging efficiency in SK has been measured with an americium-beryllium (Am-Be) source [?]. In an AmBe source, ^{214}Am decays 100 % of the time into ^{237}Np via α emission, with a half-life of 432.6 y. The α particle is captured by the ^9Be nuclei to become $^{12}\text{C}^*$ with the emission of a neutron. The carbon deexcites to the ground state with sometimes the emission of a 4.43 MeV photon. This gamma is used to trigger the neutron emission. The AmBe source is placed at the centre of a cube

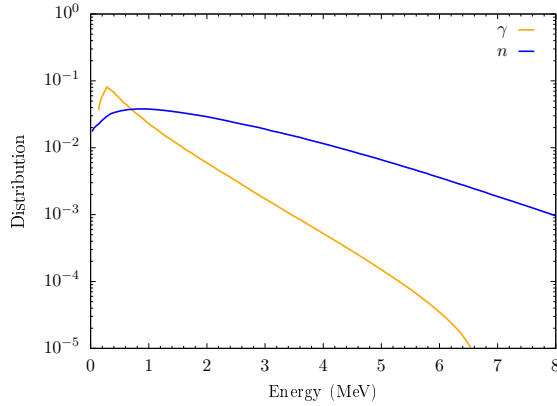


Fig. 2.3: Normalised energy distribution of neutron and photons emitted by SF events of a ^{252}Cf source [4, 5].

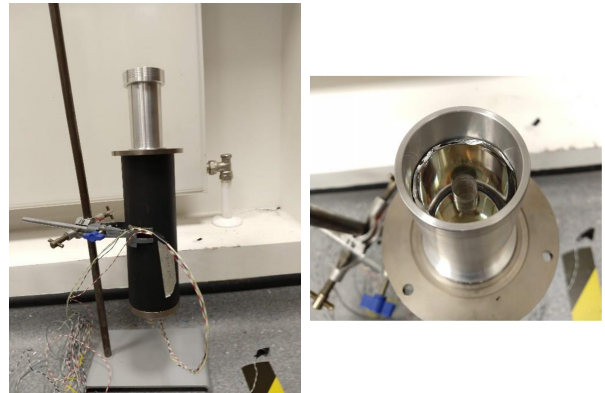


Fig. 2.4: Setup used to test the californium source.

of bismuth germanite (BGO) crystal scintillator and the device is lowered inside the water Cherenkov tank. The gamma ray from the beryllium neutron capture is promptly absorbed by the BGO crystal, with the release of scintillation light that triggers the detectors. Around a thousands of photoelectrons were typically observed. Forced triggers were imposed during the SK-III phase to extend the acquisition time window. A similiary analysis to the simulation study is then applied to search for candidates of neutron captures on hydrogen. Neutrons released by beryllium have an energy ranging from 2-10 MeV, much less than the average neutron energy following atmospheric neutrino interactions. Thus, we can make the assumption that the location of the Am-Be apparatus is roughly the same as the neutron capture vertex. The efficiency measured in Ref. [?] range from 13.1 % to 24.5 %, the exact value of which is position dependent.

Another possible source for neutron calibration is californium-252, which undergoes α -emissions (96.91%) and spontaneous fission (SF) (3.09%). With a half-life of 2.645 y, a ^{252}Cf source has a higher activity compared to an Am-Be source with the same number of nucleons. Furthermore, the SF process emits an average of 3.75 neutrons per fission and an average of 10.3 photons having a total energy of 8.2 Mev. As for the case of Am-Be, the photons can be collected by a scintillating material to tag the emission of neutrons. After this trigger signal, multiple neutron captures on hydrogen are expected, separated by short intervals in time. The yield of multiple neutrons is another advantage of ^{252}Cf that the SNO collaboration exploited to develop a method, called *Time Series Analysis* method that uses multiplicity and time intervals between the detected events to find the neutron detection efficiency, the neutron mean life inside the detector, and activity from non-fission events. The fast-neutron and photon energy spectra are shown in 2.3: the neutrons are emitted with a most-probable energy of 0.7 MeV and an average energy of 2.1 MeV.

A ^{252}Cf source was purchased by QMUL with an activity of 4.3 kBq, measured on the 28th of July, 2017. The californium is encapsulated in a double hull stainless steel cylinder, 9.5 mm in diameter and 37.5 mm high. The source is tested in a simple calibration device (see Fig. 2.4), which consists of a cylindrical plastic scintillator (EJ-200), coated with mylar to contain optical photons, and optically

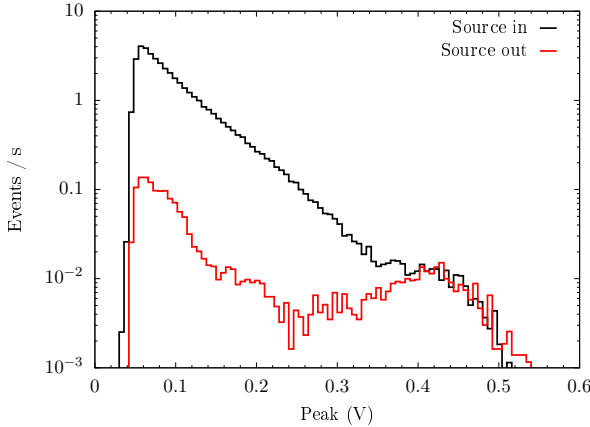


Fig. 2.5: Distribution of PMT peaks measured with source inside (black) and source removed from the scintillator (red).

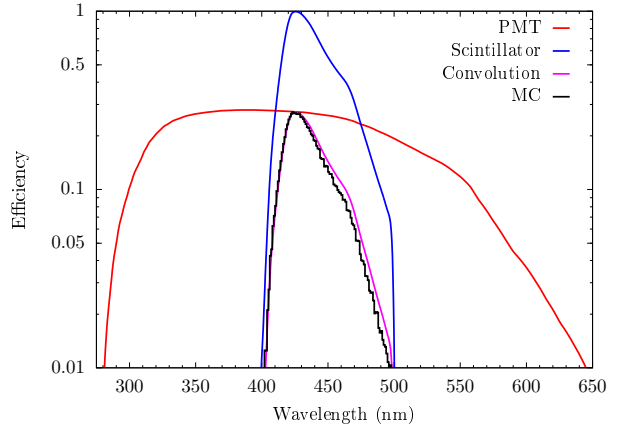


Fig. 2.6: Plot showing PMT quantum efficiency (red), the scintillator yield (blue), their convolution (magenta) and the distributions of photon collected by the PMT in the GEANT4 simulation of optical photons (black).

coupled to a ET Enterprise 9902B series PMT. A hole, coaxial to the plastic cylinder, allows to place the source in the middle of the scintillator. The cylinder is 3 in in length and 1.5 in in diameter. With this setup, the rate of photons emitted by the ^{252}Cf source can be measured; we used a Struck SIS3316 14-bit VME digitiser to count the number of photon triggers from the PMT and a daisy-chain of NIM amplifier, threshold, and discriminator is used before the digitiser to optimise the signal. Without the source inside the scintillator, an event rate of 1.633 Hz was measured, whereas with the source inside the rate increases to 41.395 Hz. The distributions of the PMT peaks collected by the digitiser are shown in Fig. 2.5. A predicted activity of 3.1 kBq is expected on the day when the measurement was taken—446 days after the activity measurement—which translates to a SF rate of 96.46 Hz. The SF tagging efficiency with this setup is therefore around 41 %.

We performed a GEANT4 simulation of the setup, with the aim of optimising the calibration device. An ideal calibration device would absorb all the photons converting them into visible light without affect the neutrons. The plot in Fig. 2.6 shows the correct implementation of the scintillator and PMT efficiencies, as there is good agreement with the MC distribution and the expected optical photon spectrum. The scintillating volume is therefore varied in the simulation to study the preformance of the device. Bismuth germanate oxide (BGO) crystal and a generic vinyltoulouene plastic are studied as scintillating materials. The size of the scintillator is also varied and shapes of a cube and a cylinder with equal diameter and height are tested. The simulation keeps track of the energy deposited in the scintillator and the number of neutrons escaping the device. The result is shown in Fig. 2.7. Unsurprisingly, the BGO crystal performs better than the plastic scintillator, with the optimal volume being a cube with 12 cm sides. The hydrogen in the plastic thermalises neutrons, which can have an impact on the thermalisation time in a water Cherenkov detector.

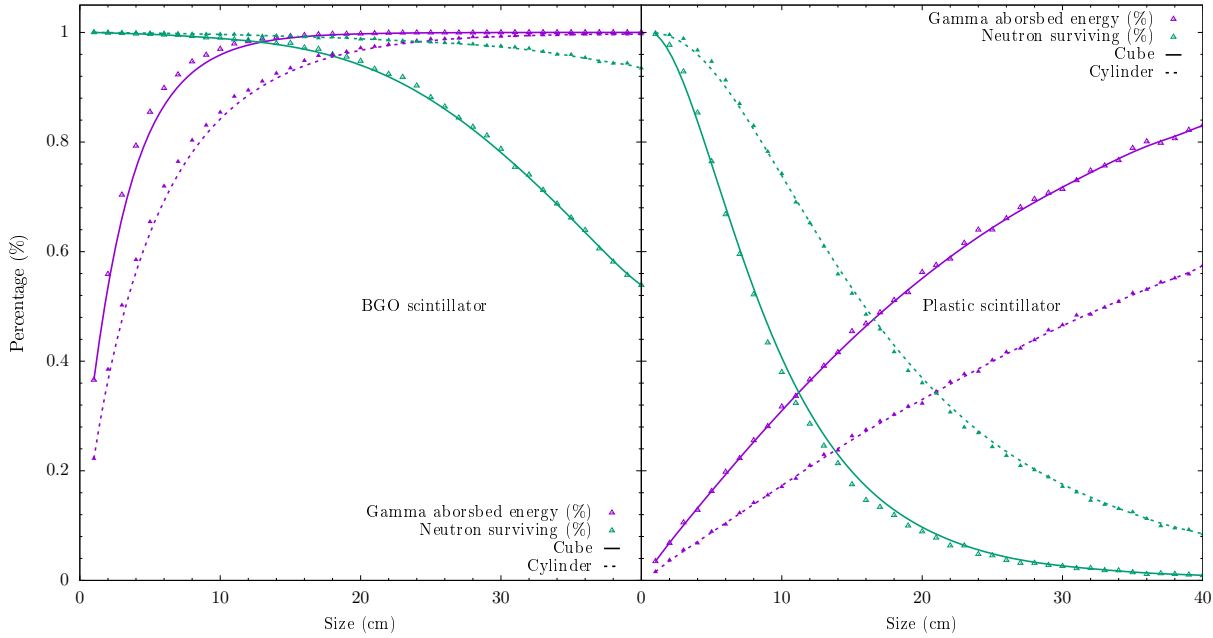


Fig. 2.7: Result of the GEANT4 simulation, showing the performance of different scintillators. Two shapes are tested: a cube (solid lines) and a cylinder with equal diameter and height (dashed lines). The percentage of energy absorbed by the scintillator (purple) and the percentage of neutrons escaping the scintillators (green) are estimated for every simulation. Left: BGO is used as scintillating material. Right: a generic vinyltoluene plastic is used.

2.4 Gadolinium neutron capture

In the next phase of the Super-Kamiokande experiment, a gadolinium salt compound $\text{Gd}_2(\text{SO}_4)_3$ will be added to the detector [], which will improve the ability of the detector to identify neutrons. Neutrons are emitted in inverse beta decay (IBD) process, $\bar{\nu}_e + p \rightarrow e^+ + n$. The current technique to tag neutrons in SK is by detecting capture on hydrogen nuclei. Capture of a thermal neutron on hydrogen has a cross-section of 332.6 ± 0.7 b, characteristic time of $\sim 200 \mu\text{s}$ in water, with the release of 2.2 MeV gammas. After the prompt Cherenkov radiation from the charged lepton, the secondary signal from an electron, compton-scattered by the 2.2 MeV photon, is looked for in a long time window. However, in water what matters are the electrons Compton-scattered above the Cerenkov threshold by relatively hard gammas.

The detectable light following neutron capture on Gd (in thin foils) in possible discrete counters was carefully simulated for the SNO heavy water Cerenkov detector. The equivalent single electron energy was found to peak at about 5 MeV, and range over 3–8 MeV. This spread reflects the intrinsic variation in the gamma cascades and the detector energy resolution (the simulation had 5 photoelectrons per MeV of electron energy, compared to 6 in SK-I) [?]. The energy threshold for SK is 5 MeV, and the search of hydrogen-tagged neutrons is not efficient (20%). A long time window in which to look for the hydrogen signal, Capture on gadolinium has a cross-section of 49×10^3 b, which de-excites emitting a ~ 8 MeV gamma-ray cascade. By adding 0.2 % by mass of the Gd salt as $\text{Gd}_2(\text{SO}_4)_3$, the characteristic time of capture is $\sim 30 \mu\text{s}$ and an efficiency of 90 % can be achieved. The isotopes ^{155}Gd and ^{157}Gd present very high cross-sections to thermal neutron capture, respectively 6.074×10^4 b and 2.537×10^5 b.

Hydrogen alone has a cross-section of 3.321×10^{-1} b.

Gadolinium-157 has the highest thermal neutron capture cross-section among any stable nuclides: 259,000 barns. Dissolving gadolinium compounds in water could considerably increase the neutron capture probability. The neutron in water thermalises quickly and can thus be captured by a Gd nucleus with a probability of 90 %. Upon capturing a neutron the Gd emits 3-4 gamma rays having a total energy of about 8 MeV. The time and spatial correlation of the positron and neutron capture events (20 μ s and 4 cm) can significantly reduce the backgrounds, and hence enhance the neutrino signal events. Even moderately energetic neutrons ranging from tens to hundreds of MeV will quickly lose energy by collisions with free protons and oxygen nuclei in water. Once thermalised, the neutrons undergo radiative capture, combining with a nearby nucleus to produce a more tightly bound final state, with excess energy released in a gamma-ray () cascade. Gd-doped water enhances the capture cross-section compared to pure water (49,000 barns compared with 0.3 barns on a free proton) and, since the cascade happens at higher energies (8 MeV vs 2.2 MeV), it produces enough optical light to be reliably detected in a large target volume.

In the original proposal by John Beacom and Mark Vagins, gadolinium trichloride GdCl_3 was proposed, but the current full-scale plan has steered on gadolinium sulfate $\text{Gd}_2(\text{SO}_4)_3$ as the salt of choice (other candidate could be gadolinium nitrate $\text{Gd}(\text{NO}_3)_3$). There are a few requirements which a Gd compound must meet in order to become a good candidate for a full scale test. The compound must be water soluble, and it should not be too difficult to dissolve large amounts. The above three candidates can all be dissolved fairly easily, with the GdCl_3 and $\text{Gd}(\text{NO}_3)_3$ only needing stirring to fully dissolve, while the $\text{Gd}_2(\text{SO}_4)_3$, can be forced into solution with the addition of a small amount of sulfuric acid, about 380 ml of acid for 28 kg of $\text{Gd}_2(\text{SO}_4)_3$ in 14 tons of water (test done at EGADS). So, this solubility requirement does not immediately rule out any of these three compounds. Next, if the compound is to be used inside a very large water Cherenkov detector, such as SK, it must be safe for the detectors components and tank, and it should be a non-toxic chemical, so it may be easily put into existing detectors. While none of the above salts are toxic, they do have very different corrosive properties, due to the different anions of the molecule. The nitrate and the sulfate turn out to be non-corrosive, and do not seem to affect detectors components much, if at all. An extensive soak test study was carried out in Japan, with each of the 31 different materials inside the SK detector being soaked in both pure water and $\text{Gd}_2(\text{SO}_4)_3$ solution. Only the rubber used for the PMT pressure housing showed any difference between the pure water and the $\text{Gd}_2(\text{SO}_4)_3$ solution, with further studies showing the rubber is unaffected by the Gd solution, if the temperature is kept below 15 °C, which it is in the case of SK. However, the chloride is corrosive, so for this reason the GdCl_3 has been ruled out as a full scale test candidate. Last the Gd compound solution must maintain a high level of optical transparency, so that light can be seen from the opposite side of the detector. Although the GdCl_3 has fairly good optical properties, it has been ruled out by the above. $\text{Gd}(\text{NO}_3)_3$ is opaque in the UV region of the electromagnetic

(EM) spectrum, for wavelengths less than 350 nm, and this unfortunately is where a large fraction of Cherenkov light is detected in SK PMTs, so it cannot be a good full scale test candidate either. This leaves $\text{Gd}_2(\text{SO}_4)_3$, and it turns out to have good transparency in the UV and optical regions of the EM spectrum, leaving it as the best candidate for the EGADS test facility. This is in fact the choice that has been made by the EGADS group, and the remaining studies described in this paper have been done using, or under the assumption that, $\text{Gd}_2(\text{SO}_4)_3$ will be used. One last exceptionally nice quality about this compound is today it costs only 5 US dollars per kilogram, meaning it would only be about 500,000 US dollars to dope SK [11], a price which is on the scale of such a major experiment. [?].

2.5 Monitoring gadolinium concentration

The concentration of Gd in water affects the efficiency and timing of neutron captures, antineutrino measurements depends on this. It is fundamental to measure the concentration regularly, as this can change in time inside the tank. On such a large scale, it is not a trivial task to predict temperature and flow dependency of the dissolved Gd. At the moment, the Evaluating Gadolinium’s Action on Detector Systems (EGADS) keeps track of the Gd concentration with a Zeeman atomic absorption spectrometer, located near the experiment. Water samples are collected from the EGADS tank, diluted and atomised inside the AAS machine. The amount of Gd is then compared to known samples of Gd loaded water to determine the concentration.

We propose an alternative method, which still uses atomic absorption lines of Gd, but in solution in water. Gadolinium presents strong emission/absorption lines in the UV region [?]. Using a UV source and a spectrometer it would be possible to measure the absorption by gadolinium dissolved in water. The absorbance is directly proportional to the amount of gadolinium and therefore to the concentration, where absorbance is defined as

$$\mathcal{A}(x) = \log_{10} \frac{I_0(x)}{I_{\text{Gd}}(x)} . \quad (2.15)$$

The spectrum I_0 of a reference sample of pure water is taken before the gadolinium loaded water sample I_{Gd} . These two spectrum are then compared at a given wavelength. The gadolinium absorbance spectrum presents a series of lines in the 270 nm – 275 nm region. The height of one peak is related to the concentration, as the amount of light surviving the sample is related to

$$I_{\text{Gd}}(x) = I_0(x) e^{-\ell/\lambda} , \quad (2.16)$$

with λ the attenuation length and ℓ the sample length. For a fixed cross-section volume and a fixed-length sample, the attenuation length will decrease with the amount of Gd in the sample m_{Gd} , or since

the volume is constant, with the concentration of Gd ρ_{Gd} .

$$\rho_{\text{Gd}} = \frac{m_{\text{Gd}}}{X \ell} . \quad (2.17)$$

The Beer-Lambert law relates the optical attenuation of a physical material containing a single attenuating species of uniform concentration to the optical path length through the sample and absorptivity of the species.

$$\mathcal{A} = \varepsilon \ell \rho = \log_{10}(e) \frac{\ell}{\lambda} , \quad (2.18)$$

where ε is the molar attenuation coefficient, or absorptivity, of the attenuating species. The Beer-Lambert law agrees with the expectation of decreasing attenuation length with increasing concentration.

In an absorbance measurement, however, there could be other sources of absorption. In a real setup, a light source and a photo sensor are needed, in addition to optical interfaces with the sample to measure; the solvent of the sample will also contribute to the overall absorbance. The Beer-Lambert law can be generalised to a generic N number of attenuating elements

$$\mathcal{A} = \sum_{i=1}^N \varepsilon_i \int_0^\ell dz \rho_i(x) = \varepsilon \ell \rho_0 + \sum_{i=1}^{N-1} \varepsilon_i \int_0^\ell dz \rho_i(x) = a + b \rho_0 , \quad (2.19)$$

where the attenuating species of interest has been isolated: if the other elements are constant, there is a linear law with measured absorbance and concentration. The absorbance will also depend on the solvent, *i.e.* water, purity and other factors, *e.g.* optical interfaces etc. The measurement of absorption could also be biased by the presence of wavelength-independent factors, or at least independent in the portion of the spectrum of interest. Examples of these factors could be micro-bubbles or other impurities in the samples. Micro-bubbles will scatter or block light, thus adding a bias on the absorbance measurement. Using two absorption peaks the measurement could be improved by taking the difference of the absorption, as any effect which is wavelength independent is removed.

$$\Delta \mathcal{A} = \mathcal{A}(x_1) - \mathcal{A}(x_2) = \log_{10} \frac{I_0(x_1)}{I(x_1)} - \log_{10} \frac{I_0(x_2)}{I(x_2)} . \quad (2.20)$$

Supposing the intensity of the reference sample is reduced by a factor η , whereas the intensity of the study sample is reduced by a factor ζ , we would have

$$\Delta \mathcal{A} = \log_{10} \frac{\eta I_0(x_1)}{\zeta I(x_1)} - \log_{10} \frac{\eta I_0(x_2)}{\zeta I(x_2)} = \log_{10} \frac{I_0(x_1)}{I(x_1)} - \log_{10} \frac{I_0(x_2)}{I(x_2)} , \quad (2.21)$$

since the difference of two logarithmic elements is taken. The drawback of this method is that two measurements are needed at the two wavelengths x_1 and x_2 , and therefore the error on the measurement will increase by a factor $\sim \sqrt{2}$.

The first concept of tracking gadolinium concentration in water using absorbance spectrum was

tested using a 1 cm cell in a commercial spectrophotometer Shimadzu UV2600, in which an initial sample of 0.2% Gd water is diluted to obtain different concentration levels. The gadolinium loaded sample is compared to a pure water one to compute the absorbance spectrum. The result is...? And linear fit. The Shimadzu spectrophotometer uses a grating system to select very narrow windows of electromagnetic spectrum both at the source and at the detection, which is done by a photomultiplier. The source at UV wavelengths is provided by a deuterium lamp, integrated in the spectrometer. The advantage of this technique is that very high resolution can be achieved, but a scan wavelength per wavelength is done, taking one measurement at the time. This process can be quite slow and the gain from the resolution is not so relevant. We tested different model of other commercial spectrometers, without integrated source and with a grating system such that the input light is spread out on a linear CCD. Doing so, the whole spectrum to which the spectroemter is sensitive to, is taken simultaneously. The measurement is then only limited to the reading speed rate of the spectrometer. A set of consecutive measurement can be taken and averaging them the error can also be estimated. After testing different models from different companies, we purchased an Ocean HDX spectrometer. The advantage of this spectrometer is a very high light throughput thanks to a toroidal mirroring system which reduces stray light and maximises the input light. In addition to this, the sensor has a high dynamic range, which is the determining factor on the absorbance measurement. Wavelength resolution is not as important, because we use the relative position of the gadolinium peaks to determine the absorbance.

The first prototype based on a 10 cm cell for 0.2% Gadolinium sulphate doping achieved a 3% concentration measurement resolution (1% neutron capture efficiency) at the target concentration in comparison to the 3.5% currently achieved via a manual mass spectrometer method.

This device was intended for deployment in EGADS in Japan but the Gadolinium sulphate concentration was changed to 0.02% in preparation for Super-K phase 1 loading. Therefore work progressed to building the version 2 prototype of GAD for sensitivity to 0.02%, by increasing the volume to ≈ 1 meter.

This prototype has been successfully built and tested and shown a concentration measurement resolution of 1% at both 0.02% and 0.2% doping.

Chapter 3

CP violation with the Hyper-Kamiokande experiment

The violation of the CP–symmetry is a well-known process in the quark sector of the standard model (SM),

[explain what CP transofrmation on a field is]

C and CP violation are some of the conditions required in order to generate an asymmetry between matter and antimatter particles, together with baryon number violation and interactions out of thermal equilibrium [6]. The amount of CP violation in the quark sector is not enough to describe the observed baryon asymmetry within the SM. An asymmetry in the lepton sector, however, could be translated into baryogenesis, via non-perturbative sphaleronic processes [7]. This process, called *leptogenesis*, would be allowed by the addition of right-handed Majorana neutrinos to the SM, which can violate lepton number. This elegant solution to explain the baryon asymmetry is a strong motivation for searches of signals of CP violation in the lepton sector.

It has been extensively observed [8–12], giving clear evidence that the Cabibbo-Kobayashi-Maskawa (CKM) matrix is complex. The CKM matrix arises from mixing of quarks in charged-current interactions (see Eq. (1.37)), when describing the fermion fields in the mass basis.

It is a generic $N \times N$ unitary matrix, where N is the number of fermion generations. The N^2 independent real parameters which describe the matrix are typically categorised into

$$\begin{aligned} \frac{N(N-1)}{2} & \text{ mixing angles} \\ \frac{N(N+1)}{2} & \text{ phases ,} \end{aligned}$$

even though, not all the phases are observables, or give physical effects. Excluding the CC term, the SM Lagrangian is invariant under a global phase transformation of the quark fields, such as

$$q_\alpha^{U,D} \longmapsto e^{i\phi_\alpha^{U,D}} q_\alpha^{U,D} . \quad (3.1)$$

Applying this to the CC Lagrangian of Eq. (1.37), we can factorise a common phase outside:

$$\begin{aligned} j_{\text{CC},Q}^\mu &= 2 \sum_{\substack{\alpha=u,c,t \\ \beta=d,s,b}} \bar{q}_{L\alpha}^U \gamma^\mu e^{-i\phi_\alpha^U} V_{\alpha\beta} e^{i\phi_\beta^D} q_{L\beta}^D \\ &= 2e^{-i(\phi_t^U - \phi_b^D)} \sum_{\substack{\alpha=u,c,t \\ \beta=d,s,b}} \bar{q}_{L\alpha}^U \gamma^\mu e^{-i(\phi_\alpha^U - \phi_t^U)} V_{\alpha\beta} e^{i(\phi_\beta^D - \phi_b^D)} q_{L\beta}^D , \end{aligned}$$

showing that there are $2N - 1$ phases that can be reabsorbed in a redefinition of the fields. A common rephasing would leave the charged current unchanged. It follows that the physical phases are

$$\frac{N(N+1)}{2} - 2N + 1 = \frac{(N-1)(N-2)}{2} \quad (3.2)$$

and the total physical parameters are

$$\frac{N(N-1)}{2} + \frac{(N-1)(N-2)}{2} = (N-1)^2 \quad (3.3)$$

In the case of three generations, there are four physical parameters, divided amongst three angles and one complex phase. The complex phase is responsible for CP violation. From a model building point of view, the complex phase may arise from complex Yukawa couplings and/or from a relative CP-violating phase in the vacuum expectation values of Higgs fields.

As three generations exist also in the lepton sector, an entirely analogous phase is expected in mixing matrix of lepton mass. The best probe to discovery CP violation is neutrino oscillation, being a purely weak process in which CP-conjugate processes can be easily studied.

CP violation in the leptonic sector is plausible and it is also a necessary ingredient for leptogenesis. Neutrino oscillation experiments can lead to the discovery of CP violation, and it is foreseen that HK will determine the value of δ_{CP} , a milestone which requires precise measurements and a deep understanding of the systematic errors.

3.1 CP violation in neutrino oscillations

The Pontecorvo–Maki–Nakagawa–Sakata (PMNS) matrix, is usually parameterised as in Eq. (1.57), with the addition of two more phases if the neutrino is Majorana. The PMNS matrix relates flavour states $\alpha = e, \mu, \tau$ with mass eigenstates $i = 1, 2, 3$ as $|\nu_\alpha\rangle = \sum_i U_{\alpha i}^* |\nu_i\rangle$. The probability of flavour oscillation in vacuum is hence computed as

$$P(\nu_\alpha \rightarrow \nu_\beta) \equiv |\langle \nu_\alpha | e^{-i\mathcal{H}t} | \nu_\beta \rangle|^2 = \sum_{ij} U_{i\alpha}^* U_{\beta i} U_{\alpha j} U_{j\beta}^* \exp\left(-i \frac{\Delta m_{ij}^2 L}{2E}\right), \quad (3.4)$$

where \mathcal{H} is the Hamiltonian, $t \simeq L$ and $\Delta m_{ij}^2 = m_i^2 - m_j^2$, and it depends on the physical angles and phases of the PMNS matrix, with the exception of the Majorana phases $\gamma_{1,2}$. The CP-conjugate of a neutrino with negative helicity is an antineutrino with positive helicity, which, in terms of neutrino oscillations, means transforming the $\nu_\alpha \rightarrow \nu_\beta$ oscillation channel into the $\bar{\nu}_\alpha \rightarrow \bar{\nu}_\beta$ channel. The violation of CP in neutrino oscillation can be quantified by the asymmetry in oscillation probabilities between neutrinos and antineutrinos, which in vacuum reads as

$$A_{\alpha\beta}^{\text{CP}} = P(\nu_\alpha \rightarrow \nu_\beta) - P(\bar{\nu}_\alpha \rightarrow \bar{\nu}_\beta) = 4 \sum_{i>j} \Im[U_{i\alpha}^* U_{\beta i} U_{\alpha j} U_{j\beta}^*] \sin\left(\frac{\Delta m_{ij}^2 L}{2E}\right). \quad (3.5)$$

The quartic product $U_{i\alpha}^* U_{\beta i} U_{\alpha j} U_{j\beta}^*$ with $\alpha \neq \beta$ and $i \neq j$ is a physical observable and so it is invariant under a reparameterization of the mixing matrix. The imaginary part of the quartic products is anti-symmetric on the indices α, β and i, j and they are all equal up to a sign. We can prove this by starting with the unitarity of the mixing matrix, for example $U U^\dagger = 1$,

$$\sum_{i=1}^3 U_{\alpha i} U_{\beta i}^* = \delta_{\alpha\beta} \quad (3.6)$$

and multiplying it by $U_{\alpha j}^* U_{\beta j}$. We can write the new relation as

$$|U_{\alpha j}|^2 |U_{\beta j}|^2 + \sum_{i \neq j} U_{\alpha i} U_{\beta j} U_{\beta i}^* U_{\alpha j}^* = \delta_{\alpha\beta} |U_{\alpha j}|^2, \quad (3.7)$$

and by taking the imaginary part of left-hand and right-hand sides of the equation it follows that

$$\sum_{\alpha \neq \beta} \Im[U_{\alpha i} U_{\beta j} U_{\beta i}^* U_{\beta j}^*] = 0. \quad (3.8)$$

This condition and the anti-symmetry of the indices reveal that the quartic products are all equal up to a sign. This value is called *Jarlskog invariant* and using the parametrisation of the PMNS matrix in Eq. 1.57 it is equal to [13]

$$J = \Im[U_{\mu 3} U_{e 2} U_{\mu 2}^* U_{e 3}^*] = \frac{1}{8} \cos \theta_{13} \sin(2\theta_{12}) \sin(2\theta_{13}) \sin(2\theta_{23}) \sin \delta_{\text{CP}}. \quad (3.9)$$

It follows that CP violation can only be measured in “appearance” channels, as the argument of the imaginary part of Eq. 3.5 is real for $\alpha = \beta$. For example, for the main channel of interest for long baseline experiments (LBL), $\nu_\mu \rightarrow \nu_e$, the asymmetry looks like:

$$\begin{aligned} \mathcal{A}_{\mu e}^{\text{CP}} &= \frac{1}{2} \cos \theta_{13} \sin(2\theta_{12}) \sin(2\theta_{13}) \sin(2\theta_{23}) \sin \delta_{\text{CP}} \\ &\times [\sin \Delta_{12} - \sin \Delta_{13} + \sin \Delta_{23}], \end{aligned} \quad (3.10)$$

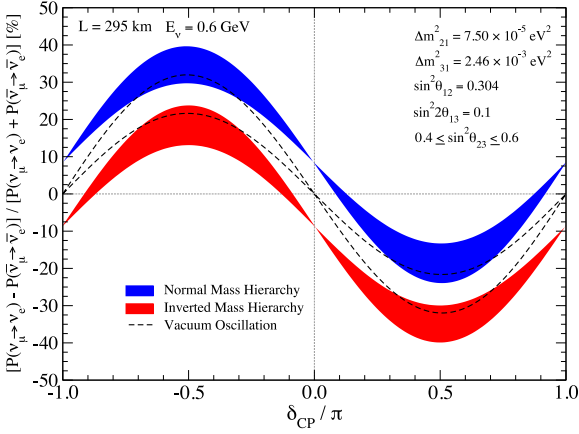


Fig. 3.1: Effect of δ_{CP} on the normalised asymmetry from Eq. 3.5.

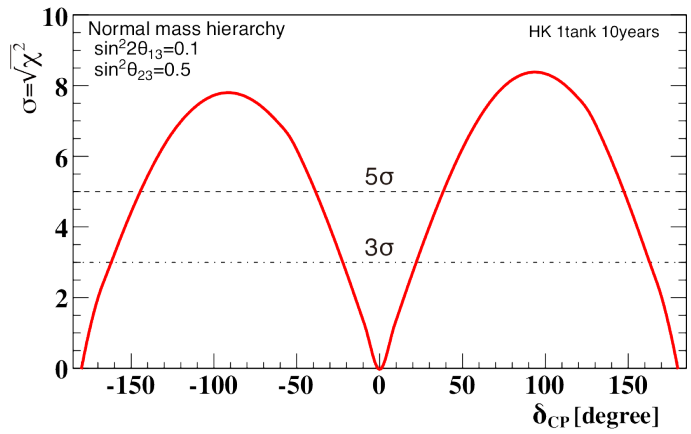


Fig. 3.2: Expected significance to exclude CP conservation, in case of normal hierarchy, where the mass hierarchy is assumed to be known [14].

where $\Delta_{ij} = \Delta m_{ij}^2 L / 4E$. Because of the above discussion, all the CP asymmetries, measured on each channel, are equal up to a sign:

$$\mathcal{A}_{\mu e} = \mathcal{A}_{\tau \mu} = \mathcal{A}_{e \tau} = -\mathcal{A}_{e \mu} = -\mathcal{A}_{\mu \tau} = -\mathcal{A}_{\tau e}. \quad (3.11)$$

Including matter effects, we can focus on the limit where the effects of the atmospheric mass difference dominates. This holds to LBL experiments and leads to helpful cancellations in the evolution equation which reads

$$i \frac{d}{dx} \begin{pmatrix} \psi_{\alpha 1} \\ \psi_{\alpha 2} \\ \psi_{\alpha 3} \end{pmatrix} = \frac{1}{2E} \begin{pmatrix} s_{13}^2 \Delta m_{31}^2 + a & 0 & c_{13} s_{13} \Delta m_{31}^2 \\ 0 & 0 & 0 \\ c_{13} s_{13} \Delta m_{31}^2 & 0 & c_{13}^2 \Delta m_{31}^2 \end{pmatrix} \begin{pmatrix} \psi_{\alpha 1} \\ \psi_{\alpha 2} \\ \psi_{\alpha 3} \end{pmatrix}, \quad (3.12)$$

which depends only on the mixing angle θ_{13} and is independent of the CP-violating phase. Hence, CP violation is not observable in experiments which are only sensitivite to Δm_{31}^2 , just by looking at neutrino oscillations in matter, as well as in vacuum. This is easily understandable, as the limit dictated by Eq. (1.59) corresponds to an effective two-flavour oscillation. However, the oscillation probabilities of neutrinos and antineutrinos in matter are not the same, because the medium is not CP-invariant and it induces CP violation in the oscillation probabilities.

The effect of the CP-violating phase on the asymmetry of Eq. 3.5 can be appreciated from the plot in Fig. 3.1.

Given the parametrisation in Eq. 1.57, this asymmetry is not measurable if the phase is trivial, *i.e.* $\delta_{CP} = 0$ or $\pm\pi$, or if θ_{13} is vanishing. From a model building point of view, however, a successful leptogenesis requires the parameters to satisfy $|\sin \theta_{13} \sin \delta_{CP}| \gtrsim 0.09$ when the Majorana phases are vanishing [15]. The value of θ_{13} has been measured to be non-zero [16–19] and for this reason it is expected that on-going and future generation neutrino experiments will also constrain the value of δ_{CP} .

3.2 Hyper-Kamiokande experiment

Hyper-Kamiokande (HK) [14] will be the next-generation water Cherenkov detector, superseding its predecessor, Super-Kamiokande (SK). Employing ring-imaging technique, the rare interactions of neutrinos can be detected, as well as the possible spontaneous decay of nucleons. The design of HK does not deviate much from SK and Kamiokande. The cylindrical tank of HK will be 72 m high and 68 m in diameter, with a fiducial volume of 188.4 kton (total volume 257.8 kton), around 8.4 times the fiducial volume of SK. The photo-coverage of the inner detector region will be 40 %, the same of SK, but it translates to roughly forty thousands photomultipliers (PMTs). New 20"box and line PMTs will be employed, with improved charge and timing resolution, thanks to the increased quantum efficiency which is almost twice the QE of previous PMT generation. It also has the high pressure tolerance for the usage below 60 m depth of water. A study for implementing multi PMT modules, containing each 23 3" PMT, is being carried out. The detector will be located underground at Kamioka mine in Gifu Prefecture, with an overburden of approximately 650 meters or more of rock, which is equivalent to 1750 meters or more of water.

Thanks to incredible statistics and cutting edge resolutions, HK will be capable of a vast variety of physics studies, from accelerator and atmospheric neutrinos to solar and supernova neutrinos. Besides detecting proton decay, the main goal of HK is to measure δ_{CP} and constrain the other oscillation parameters with high precision. This is achievable by studying accelerator neutrinos, and to this end the possibility of installing a second detector in Korea, at the secondary oscillation peak, is being investigated.

HK will be located 295 km away from the target and 2.5° off-axis with respect to the beamline. The detector cavity is planned to be excavated in Mt. Nijugo-yama in the Tochibora-mine in Gifu Prefecture, which is approximately 8 km south from SK. The neutrino beam is generated by a 30 GeV proton beam colliding on a fixed graphite target; a focusing horn selects positively charged (ν mode) or negatively charged ($\bar{\nu}$ mode) pions, which decay leptonically, to obtain an almost pure muon neutrino or antineutrino beam, peaking at 600 MeV. The accelerator facility at J-PARC will undergo a planned upgrade to increase the beam power up to 1.3 MW, before HK starts operation. The T2K near detector system, comprised of the two modules ND280 and INGRID, will be refurbished and the new Intermediate Water Cherenkov Detector, possibly gadolinium-loaded, will be located around 1 km from the target.

HK will take data for ten years, collecting a total of 2.7×10^{22} Protons On Target, divided between ν and $\bar{\nu}$ beam modes. Studies have shown that CP violation discovery is not very sensitive to the time ratio between the two modes (ref?). Assuming $\nu : \bar{\nu} = 1 : 3$ and $\delta_{CP} = 0$, the expected number of fully-contained events in the fiducial volume for the channels $\nu_\mu \rightarrow \nu_e$ and $\bar{\nu}_\mu \rightarrow \bar{\nu}_e$ are respectively 1643 and 15 in ν mode and 206 and 1183 in $\bar{\nu}$ mode, assuming CP conservation. Deviations from these expected numbers could be indication of CP violation. A preliminary study for the HK design report [14], using a different analysis, estimated a significance well-above 5σ after ten years of data taking, as can be seen

in Fig. 3.2.

The project has been recently approved by Japanese government and data taking is expected commencing by 2027.

The uncertainty of the Earth's density between Tokai and Kamioka is estimated to be at most 6% [181]. Because the matter effect contribution to the total $\nu_\mu \rightarrow \nu_e$ appearance probability is less than 10% for 295km baseline, the uncertainty from the matter density is estimated to be less than 0.6% and neglected in the following analysis.

3.3 Sensitivity studies

At any stage of the experiment it is important to assess the impact of systematic errors on the total sensitivity of HK. One of the main goals is to constrain with high precision oscillation parameters, especially δ_{CP} and the octant determination. Even if real data is not available, it is possible to understand whether the statistics collected have enough constraining power to achieve the target precision. The oscillation parameters and systematic uncertainties are input to a Monte Carlo simulation to build expected distribution of events. This expected data is then compared to simulated *observed data*, which is created by selecting a combination of oscillation parameters in order to mimic the real distributions of events that will be collected eventually. Scanning over the oscillation parameters, the resolution of HK to oscillation parameters and, more importantly, the influence of the systematic uncertainties can be studied.

3.3.1 Event samples

For the study, SK atmospheric Monte Carlo (MC) is adapted and scaled to HK statistics to compose the atmospheric sample. A total of 2224 bins are used, divided in several two-dimensional histograms of $\log p$ and $\cos \vartheta$, where ϑ is the azimuthal angle. These are divided in the usual categories of fully-contained, partially-contained, and upward-going muons, and are summarised in Tab. 3.1 [20]. The beam sample, instead, is created using the far detector flux predicted with NEUT. From the flux prediction, fully-contained candidate events in the fiducial volume are grouped as appearance signal, i.e. $\nu_\mu \rightarrow \nu_e$ and $\bar{\nu}_\mu \rightarrow \bar{\nu}_e$, and background, i.e. unoscillated neutrinos. Signal and background distributions in true energy (98 bins) undergo event selection criteria to obtain the distributions in reconstructed energy (87 bins) for the four event samples:

- one ring e -like in ν -mode,
- one ring e -like in $\bar{\nu}$ -mode,
- one ring μ -like in ν -mode,
- one ring μ -like in $\bar{\nu}$ -mode.

A set of 2D smearing matrices, produced by the T2K fitting framework VALOR, simulates and replaces the correct event selection process, including tuning of the flux with near detector constraints.

Tab. 3.1: Samples event for atmospheric data. They are categorised as fully-contained sub-GeV (FC sub-GeV), fully-contained multi-GeV (FC multi-GeV), partially-contained (PC) and upward-going muons (UP- μ).

Event type	Sample	Bins $\log p$	Bins $\cos \theta$
FC sub-GeV	one ring e -like and 0 decay- e	13	20
	one ring e -like and 1 decay- e	13	2
	one ring μ -like and 0 decay- e	13	20
	one ring μ -like and 1 decay- e	13	20
	one ring μ -like and 2 decay- e	13	2
	one ring π^0	13	2
	two rings π^0	5	2
FC multi-GeV	one ring ν_e -like	10	20
	one ring $\bar{\nu}_e$ -like	10	20
	one ring ν_μ -like	5	20
	multi ring ν_e -like	8	20
	multi ring $\bar{\nu}_e$ -like	8	20
	multi ring ν_μ -like	4	20
	multi ring other	10	20
PC	stopping	4	20
	through-going	5	20
UP-μ	stopping	4	20
	through-going, not showering	1	20
	through-going, showering	1	20

Tab. 3.2: Oscillation space.

Parameter	Nominal	Range	Points
$\Delta m_{12}^2 / 10^{-5} \text{ eV}^2$	7.53	–	fixed
$\sin^2 2\theta_{12}$	0.8463	–	fixed
$\Delta m_{23}^2 / 10^{-3} \text{ eV}^2$	2.509	[2.464:2.554]	13
$\sin^2 2\theta_{13}$	0.085	[0.070:0.100]	13
$\sin^2 \theta_{23}$	0.528	[0.426:0.579]	19
δ_{CP}	$-\pi/2$	$[-\pi:\pi]$	61

These smearing matrices are provided for all samples, acting on signal (CCQE and CCnQE) and background (CCQE, CCnQE, and NC) distributions.

3.3.2 Systematic model

There are 67 systematics for the atmospheric sample, adopted from SK atmospheric studies [21]. List systematics. A more accurate systematic study for the atmospheric analysis of HK is expected in the future. The atmospheric systematics are initially uncorrelated with the beam systematics. The focus of this work is the beam sample.

For the beam part, the T2K 2018 error model is employed [22]. There are 74 uncertainties for flux and cross-section parameters, from near detector constraints, known as the BANFF fit. divided in 25×2 systematics, for each beam mode, for the four main flux components, They are grouped in 50 systematics—25 for the ν mode and 25 for the $\bar{\nu}$ mode—for the main flux components (ν_e , ν_μ , $\bar{\nu}_e$, and

$\bar{\nu}_\mu$), and 24 systematics for cross-section parameters. There are also 45 uncertainties for SK detector efficiencies and Final State Interactions, which parameterise the uncertainties on the four final state event selections at the far detector: 1 ring e -like and 1 ring μ -like in both ν and $\bar{\nu}$ modes. The 1 ring e -like + 1 electron decay sample is not treated in this study. Among these, one systematic describes the energy scale uncertainty. It consists of 25 systematic uncertainties, constrained by near detector fits, for each beam mode—neutrino or antineutrino—describing are described by 25 systematics for each beam mode—neutrino or antineutrino. There are 24 errors that describe cross section parameters, also constrained by near detector data. from flux and cross-section parameters constrained by near detector fits. Among the flux and cross-section parameters, These For the four main flux components 25 uncertainties for the beam in neutrino mode and 25 for the antineutrino mode. ($2p2h$ normalisation and shape for ^{16}O , CCQE axial-mass scaling factor, CC and NC interaction normalisations, RPA coefficients, binding energy on oxygen). In addition, there are 45 systematics from SK detector efficiencies and Final State Interactions, which parameterise the uncertainties on the four final state interaction types at the far detector: 1 ring e -like and 1 ring μ -like in both ν and $\bar{\nu}$ modes. One systematic is adopted to describe the energy scale uncertainty at the far detector.

The momentum reconstruction of neutrino event is mainly based on the charge observed by the PMTs in the tank. The factors discussed above, including water property or PMT gain will affect the performance of momentum reconstruction. On the other hand, the precise momentum determination of the neutrino event is necessary for the neutrino oscillation analysis since the oscillation probability is highly related to the energy of neutrinos. Four well-known independent control samples are used for the energy scale calibration [6] and systematic evaluation in different momentum range: Track length of high energy stopping muons (1 – 10 GeV/c) Cherenkov angle of low energy stopping muons (200 – 500 MeV/c) Invariant mass of π^0 produced by neutrino interactions (– 130 MeV/c) Momentum distribution of decay electron (– 40MeV/c).

3.3.3 Oscillation space

Both the atmospheric and beam distributions are weighted by the corresponding oscillation probabilities. For the study of this thesis, the oscillation parameters are scanned over the space The oscillation space spans four variables, Δm_{32}^2 , $\sin^2 2\theta_{13}$, $\sin^2 \theta_{23}$, and δ_{CP} , on a grid of respectively $13 \times 13 \times 19 \times 61$ points. The solar squared mass difference and the solar angle are fixed. Apart from δ_{CP} which is scanned over all possible values, the intervals for the other parameters are built around “Asimov A”, the nominal T2K best fit point [23]. For the atmospheric squared mass difference and the reactor angle, the range is chosen such that it covers a $[-3\sigma, +3\sigma]$ interval, where σ is the error from the Asimov A set; the range for $\sin^2 \theta_{23}$ spans over $[-6\sigma : +3\sigma]$ so that both octants are covered. Reactor experiments [24, 25]. At each point of this space, the event distributions are weighted with the correct oscillation probability for appearance or disappearance channels. A special point of the parameter space is chosen as a *true* com-

bination of oscillation parameters to perform sensitivity studies using a χ^2 -test statistics. By changing the *true* point, it is possible to define the exclusion regions for CP violation, by comparing the χ^2 at any value of δ_{CP} with the χ^2 computed at the null hypothesis, i.e. CP conservation. The sensitivity to exclude the $\sin \delta_{\text{CP}} = 0$ as a function of *true* δ_{CP} is quantified by

$$\sigma = \sqrt{\min_{\delta_{\text{CP}}=0,\pm\pi} \chi^2 - \chi^2_{\text{true}}} , \quad (3.13)$$

where χ^2_{true} is evaluated at the *true* point.

3.3.4 χ^2 test

The test statistics of this analysis is defined as a “pull approach” χ^2 [26], in the following way

$$\chi^2 = \min_{\underline{\varepsilon}} \left[\chi^2(\vartheta; \underline{\varepsilon}) \right] , \quad (3.14)$$

with ϑ the oscillation parameters and $\underline{\varepsilon}$ the full set of j systematic errors, and

$$\chi^2(\vartheta; \underline{\varepsilon}) = 2 \sum_n \left[E_n (1 + \sum_j f_j^n \varepsilon_j) - O_n + O_n \log \left(\frac{E_n (1 + \sum_j f_j^n \varepsilon_j)}{O_n} \right) \right] + \sum_{ij} \varepsilon_i \rho_{ij}^{-1} \varepsilon_j , \quad (3.15)$$

where O_n and E_n are respectively the number of observed and expected events in the n -th bin and ρ^{-1} is the inverse of the correlation matrix of the systematic errors. As there is no real data, the “observed” events are replaced by a prediction at the *true* oscillation point. The systematic uncertainties are embedded in the f_j^n term, which is the fractional change induced on the n -th bin by a 1σ variation of the j -th systematic; the amount of the shift is quantified by the “pull” ε_j in units of the uncertainty σ_j . For most of the systematic parameters, a linear response is assumed in the MC. This means that varying of the j -th systematic by a known amount, $\beta_j \rightarrow \beta_j + \varepsilon_j \sigma_j$, the number of expected events changes:

$$\beta_j \xrightarrow{\text{MC}} E_n \quad \Rightarrow \quad \beta_j + \varepsilon_j \sigma_j \xrightarrow{\text{MC}} E_n (1 + \varepsilon_j f_n^j) .$$

Certain systematic uncertainties, such as the CCQE axial-mass scaling factor, the Fermi momentum for ^{16}O , or some of the RPA coefficients¹, do not present a linear behaviour for small values of ε and they are better described by a four-point linear interpolation of different f_j^n histograms, computed at $\pm 1\sigma$ and $\pm 3\sigma$ variations of the systematic parameter. Given a *true* point, the χ^2 is computed at each point of the oscillation parameter space and it is minimised with respect to the pulls ε . This leads to a set of

¹The Random Phase Approximation (RPA) method is applied to calculate the total cross sections of electron neutrinos on nuclei.

j non-linear equations

$$\frac{\partial \chi^2}{\partial \varepsilon_j}(\vartheta; \underline{\varepsilon}) = 0 . \quad (3.16)$$

The system can be solved with the Newton's method by finding the Hessian of the χ^2 . This gives a linear system, which can be iterated until sufficient precision is achieved

$$\frac{\partial^2 \chi^2(\underline{\varepsilon}^{(n)})}{\partial \varepsilon_k \partial \varepsilon_j} \cdot (\varepsilon_j^{(n+1)} - \varepsilon_j^{(n)}) = -\frac{\partial \chi^2(\underline{\varepsilon}^{(n)})}{\partial \varepsilon_k} , \quad (3.17)$$

with (n) the iteration index. To account for future constraints from other experiments, a gaussian penalty terms is added to the χ^2 definition of Eq. (3.15)

$$\chi^2_{\text{penalty}} = \frac{(\vartheta - \hat{\vartheta})^2}{\sigma_{\vartheta}^2} . \quad (3.18)$$

The current constraint applied is the measurement of θ_{13} by future reactor experiments, that will achieve $\sin^2 2\theta_{13} = 0.085 \pm 0.005$.

3.4 Systematic studies

It is expected that larger systematic errors will result in a worse sensitivity, but certain uncertainties affect the measurement of the oscillation parameters more than others. For example, these can be the uncertainties on ν_e and $\bar{\nu}_e$ charged-current cross sections, the transverse flux model, the pion absorption probability, the total energy scale in SK, or the flux alignment. We study the impact of some selected systematics by modifying the nominal systematic model and analysing the overall predicted sensitivity of the experiment in these different scenarios. Doing so, it is possible to determine which systematics have the most important repercussion on the sensitivity, since it is fundamental to understand their effect at all phases of the experiment.

3.4.1 Validation of the fitter

To validate the fitting framework a special systematic set for the beam sample is used. It is composed of just two systematics: the ν_e and the $\bar{\nu}_e$ CC cross-section uncertainties. These two errors are correlated, anti-correlated (and uncorrelated) and they are tested at different magnitudes: 1%, 2%, 3%, 4%, and 5%. This means a total of 15 fits. Given the definition of χ^2 in Eq. (3.15), at fixed magnitude the difference between the sets is just the correlation matrix, whereas at fixed correlation matrix the differences are the 1σ histograms.

$$\rho = \begin{pmatrix} 1 & 1 \\ 1 & 1 \end{pmatrix} , \quad \rho = \begin{pmatrix} 1 & -1 \\ -1 & 1 \end{pmatrix} , \quad \rho = \begin{pmatrix} 1 & 0 \\ 0 & 1 \end{pmatrix} . \quad (3.19)$$

The correlation matrices written as above are singular and so not invertible. In order to get the inverted matrix, an offset of 10^{-5} is added to off-diagonal terms.

3.4.2 Variations to the nominal model

A series of modifications are performed on the nominal systematic model is modified:

3.5 Dependencies on exclusion of CP

Unknown mass hierarchy, statistics ecc, octant determination.

Chapter 4

Neutrino mass generation

[check PDG <http://pdg.lbl.gov/2019/reviews/rpp2019-rev-neutrino-mixing.pdf>]

The evidence for three neutrino flavour oscillation is well established [1, 2] and can be accounted for only if neutrino mass splittings are non zero [?]. This implies that neutrinos are massive and mix, forcing to consider extensions of the Standard Model (SM) to explain their origin. A simple means of doing so is to introduce the right-handed counterpart of SM neutrinos, which are singlet with respect to all SM gauge symmetries. The Lagrangian includes a Yukawa coupling between these sterile states, the Higgs boson and the leptonic doublet, which generates Dirac mass-terms below the scale of Electroweak Symmetry Breaking (EWSB), and Majorana mass terms for the new singlet states. On diagonalisation of the resulting neutrino mass matrix, the heavy neutrino states, commonly known as nearly-sterile neutrinos or Heavy Neutral Leptons (HNLs) in experimental contexts, remain mainly in the sterile neutrino direction and have sub-weak interactions suppressed by elements of the extended Pontecorvo-Maki-Nakagawa-Sakata (PMNS) mixing matrix.

These states have been connected to a vast range of phenomenological behaviours and even to cosmological implications (for a recent review on sterile neutrinos, see *e.g.* Ref. [27]). For instance, nearly-sterile neutrinos in the keV region are viable warm Dark Matter candidates (see *e.g.* Ref. [28]), whereas heavier HNLs could play a role in leptogenesis [7, 29–40]. So far, some possible hints in favour of heavy neutrinos have emerged in neutrino appearance oscillation experiments, specifically LSND [41] and MiniBooNE [42–44] but are disfavoured by disappearance experiments [45–47], unless non-standard effects are present [48–51]. Further hints in the same mass range have been reported for mixing with electron neutrinos in the so-called reactor anomaly [52–56] and in the less statistically significant Gallium one [57–59]. Explanations of the MiniBooNE low energy excess invoking GeV-scale HNLs with non-standard interactions [60–64], have also been put forward. In these models, heavy neutral fermions are produced by neutrino up-scattering in the detector and subsequently decaying into photons or electrons, which mimic an electron neutrino interaction. The interpretation of the current experimental results is still largely debated in the scientific community. Searches both for electron-like signatures in MicroBooNE, the SBN programme at Fermilab [65], and in short baseline reactor neutrino experiments,

such as DANNS [56], NEOS [55], PROSPECT [66], STEREO [67], NEUTRINO-4 [68], will shed further light on these possibilities.

Apart from these controversial hints, no positive evidence of heavy neutrinos has been found to date in laboratory searches. A thorough review of the current constraints can be found in Refs. [69, 70]. Bounds critically depend on the HNL masses and the flavour with which they mix. Searches for kinks in Curie plots of β -decay spectra [71–75] have placed bounds on the electronic mixing for HNL masses between the keV and MeV scales. For masses from a few MeV to a few hundreds MeV, searches for monochromatic peaks in the lepton spectrum of decaying pions and kaons place important bounds on the muonic and electronic mixing angles [76–80]. Neutrinoless double beta decay indirectly constrains Majorana HNLs from the eV to the TeV scale and lepton number violating meson and tau decays can be used to set limits on the mixing angle in narrow ranges of HNLs masses [69]. The tightest constraints come from searches for the direct production and subsequent decays of heavy neutrinos in *beam dump* experiments and at colliders. The strongest limits were set by the PS191 experiment [81, 82], a beam dump experiment which ran at CERN in 1984. Its most stringent upper bounds on the novel mixing angles are $|U_{e4}|^2, |U_{\mu 4}|^2 \leq 10^{-8} - 10^{-9}$ for neutrino masses between the pion and the kaon mass. Other bounds of this type can be found in Refs. [83–89] as well as collider ones, from LHCb [90], ATLAS [91], CMS [92, 93], BELLE [94] (see also Ref. [95]).

It is exciting to note that current and upcoming neutrino oscillation experiments will be able to perform beam dump style measurements [96–98]. A crucial difference between oscillation detectors and dedicated beam dump searches of the past is that the former tries to maximise its Standard Model neutrino scattering rate, while the latter goes to lengths to suppress it in order to reduce backgrounds. However, for some of the current and future accelerator neutrino experiments, such as the Short Baseline Neutrino (SBN) program [65], the strong particle reconstruction capabilities of Liquid Argon detectors and distinctive kinematics of neutrino decays have been shown to allow competitive bounds on heavy neutrinos to be made despite naively large backgrounds [99]. Long baseline oscillation experiments, such as the upcoming Deep Underground Neutrino Experiment (DUNE) [100], will see a greatly diluted flux of nearly-sterile neutrinos at their far detectors and consequently poor sensitivity. However, the DUNE Near Detector (DUNE ND), placed 574 m from the target, has a great potential for searches for new physics [101]. Even if the final design of the ND has not been confirmed as yet, the options being considered combine a large active volume, in close proximity to a very intense neutrino beam and cutting-edge event reconstruction capabilities. These will allow DUNE ND to undertake valuable searches for BSM physics in a entirely complementary way to the central oscillation physics programme.

In this article, we present a detailed analysis of the sensitivity of DUNE ND to HNL in beam dump style searches. Differently from previous sensitivity studies [101, 102], we ground our discussion in theoretically consistent models, in which sterile neutrinos are associated with neutrino mass generation via a low-scale seesaw mechanism. We note that the range of masses and mixing angles testable at

DUNE ND is of interest for the generation of the baryon asymmetry in the context of the ASR mechanism [34–37, 40]. We consider both Majorana and pseudo-Dirac states and calculate their decay and production rates, with careful consideration given to helicity arguments. These formulae are then used to estimate the sensitivity of the experiment, taking into account the beam and detector performance capabilities thanks to simulations of both event and background signals. We stress that DUNE will be able to extend the current limits on new fermionic singlets, including those with masses above 500 MeV, probing models of theoretical significance for the generation of neutrino mass. We show that bounds can be put also on the mixing with tau neutrinos, thanks to the high energy beam.

The article is organised as follows. In Section 4.1 we discuss neutrino mass generation and its consequences for heavy neutrinos in the mass range of interest. In Section 4.2 and Section 4.3, we present the nearly-sterile neutrino decay and production rates accounting for both Majorana/(pseudo-)Dirac states and fully incorporating helicity effects and distributional information about the final-state observables. In Section 5.3, we turn to DUNE ND, describing our assumptions about the experimental apparatus, our neutrino flux modelling, including a $\nu_\tau/\bar{\nu}_\tau$ simulation, the expected signal and the impact of backgrounds. In Section 5.4, we quantify the sensitivity of DUNE ND to decays of heavy neutrino and, in Section 5.5, its ability to constrain the parameter space of low-scale seesaw models. Our concluding remarks are made in Section 6.

4.1 Heavy neutrinos in seesaw models

The lightness of the observed neutrino masses can be explained in a range of different scenarios. New SM-gauge singlet fermions are a feature common to many of them. The most general Lagrangian including a set of right-chiral gauge singlets $\{\mathcal{N}_i\}$ is given by

$$\mathcal{L}_{\text{SM}+\mathcal{N}} = \mathcal{L}_{\text{SM}} + i\bar{\mathcal{N}}_i \partial^\mu \mathcal{N}_i + Y_{\alpha i} \bar{L}_\alpha \tilde{H} \mathcal{N}_i + \frac{1}{2} (M_R)_{ij} \bar{\mathcal{N}}^c_i \mathcal{N}_j + \text{h.c.} , \quad (4.1)$$

with \mathcal{L}_{SM} denoting the SM Lagrangian and the other symbols taking their conventional meaning. Without loss of generality, M_R can be chosen to be diagonal. After electroweak symmetry breaking, a Dirac mass emerges for which we will use the notation $m_D \equiv vY/\sqrt{2}$. This term appears, for instance, in the famous Type I seesaw mechanism [103–106]. Majorana masses for the light neutrinos arise and are given by

$$m_\nu = -m_D M_R^{-1} m_D^T + \mathcal{O}\left([m_D M_R^{-1}]^2\right) . \quad (4.2)$$

The heavy neutrino masses are approximately given by the diagonal entries of M_R and its corresponding eigenstates, the heavy nearly-sterile neutrinos N_i , have suppressed mixing with active neutrinos and are mainly composed by sterile fields. Neglecting the matrix nature of these expressions for now, if m_D takes values around the electroweak scale, acceptable neutrino masses are produced when M_R has values

around the GUT scale, suggestively connecting it to a high-scale breaking of $U(1)_{B-L}$ [103]. Low-scale solutions are also possible by taking the Yukawa couplings to be similar or smaller than the other SM lepton Yukawa couplings, *e.g.* if m_D takes values in the keV range, new nearly-sterile states would exist with masses around a GeV. Although the mass scale for the heavy neutrino can span many orders of magnitude, the resulting mixing is constrained by the contribution given to light neutrino masses

$$|U_{\alpha N}|^2 \lesssim \frac{m_\nu}{m_N} \lesssim 10^{-10} \frac{1 \text{ GeV}}{m_N}, \quad (4.3)$$

where we have taken $m_\nu \lesssim 0.1 \text{ eV}$. These suppressed mixing angles make experimental searches for heavy neutrinos in this range particularly challenging, and beyond the capabilities of most experiments to-date.

In recent years a lot of interest has focused on more complex models with multiple new fermion states, *e.g.* the Inverse Seesaw (ISS) [107, 108], extended seesaw [109] and linear seesaw models [110, 111]. In these cases the bound in Eq. (4.3) can be avoided because of the cancellation between the contributions to neutrino masses by a different sterile neutrino. For definiteness, we will focus on the ISS model. In this case, a quasi-preserved lepton number guarantees the specific texture of M_R and m_D and its small breaking is natural in the 't Hooft sense [112].

The physical spectrum of heavy neutrinos can be best understood in the Lepton Number Conserving (LNC) limit. We use ISS (a, b) to denote the model with a (b), $a, b \neq 0$, new gauge singlets of lepton number $+1$ (-1). Following Eq. (4.1) and Eq. (4.2), the most general mass matrices are then given by

$$m_D = \begin{pmatrix} m & 0 \end{pmatrix} \quad \text{and} \quad M_R = \begin{pmatrix} 0 & M^T \\ M & 0 \end{pmatrix},$$

where we introduce the $3 \times a$ complex matrix m and the $b \times a$ complex matrix M . The spectrum of physical states in the LNC limit for ISS (a, b) is given by

$$\min\{3 + b, a\} \text{ Dirac pairs} \quad \text{and} \quad |3 + b - a| \text{ massless Weyl states.}$$

The masses of the Dirac pairs are the non-zero singular values of the rectangular $a \times (3 + b)$ matrix (m^T, M^T) . Note that for $a \neq b$, in addition to a set of Dirac pairs of arbitrary masses, extra massless sterile states degenerate with the light neutrinos are present. Mixing involving these degenerate states is not defined in the LNC limit, as any unitary map in the degenerate subspace is permissible. On the contrary, the introduction of a small Lepton Number Violating (LNV) parameter perturbs the LNC spectrum as well as the mixing. In general there are only two possible origins for a low-scale heavy neutrino:

- A massless Weyl fermion in the LNC limit which is given non-zero mass proportional to the per-

turbation. As the mixing between massless states is not defined in the LNC limit, the perturbation controls the induced mixing between the nearly-sterile state and the active ones. We will refer to this state as a Majorana neutrino.

- A massive Dirac pair at the low scale in the LNC limit, becoming a pseudo-Dirac pair after the perturbation, which regulates the mass splitting of the pair. In the LNC limit, the mixing angles between Dirac pair and light neutrinos can be arbitrarily large, and this property remains after the perturbation.

The first case only arises in models with an imbalanced number of new fields, *i.e.* ISS (a, b) such that $a \neq b$, while the second option can occur in any ISS model.

In this paper, we are interested in heavy states with masses in the MeV–GeV range.¹ Our discussion above suggests that both Majorana states and (pseudo-)Dirac states should be considered, covering all possible phenomenological aspects. In what follows, we will compute the production and decay rates for Majorana states and Dirac states and study their discovery potential at DUNE ND. We disregard lepton number violating effects and therefore the distinction between pseudo-Dirac and Dirac states will not be relevant.

Feynman rules for Majorana states derived from Eq. (4.1) can be found in [69], or constructed using the techniques of Ref. [113]. For an explicit comparison between Dirac versus Majorana Feynman rules for heavy neutrinos, see Ref. [114].

4.2 Heavy neutrino decay

In this section we compute the heavy neutrino decay rates and polarised distributions necessary for the simulation of beam dump searches. We compute rates for both Majorana and (pseudo-)Dirac states, allowing us to consistently explore the parameter space of low-scale seesaw models.

This analysis can be simplified by noting the following equivalences. A Majorana neutrino N decaying via a charged current process has the same differential decay rate as the Dirac neutrino N_D with the appropriate lepton number,

$$d\Gamma(N \rightarrow \ell_\alpha^- X^+) = d\Gamma(N_D \rightarrow \ell_\alpha^- X^+) \quad \text{and} \quad d\Gamma(N \rightarrow \ell_\alpha^+ X^-) = d\Gamma(\bar{N}_D \rightarrow \ell_\alpha^+ X^-),$$

where we assume identical mass and mixing angles for both Dirac and Majorana neutrinos. This equivalence can be seen directly from the Feynman rules for Dirac and Majorana fermions [113] (see also Ref. [114]), but also explicitly in our formulae below. In a neutral current (NC) decay, however, the two contractions of the NC operator lead to another contribution,

$$d\Gamma(N \rightarrow \nu X') = d\Gamma(N_D \rightarrow \nu X') + d\Gamma(\bar{N}_D \rightarrow \bar{\nu} X').$$

¹This is motivated by the kinematic limits on production from meson decays discussed in more detail in Section 4.3.

Channel	Threshold	Channel	Threshold	Channel	Threshold
$\nu\nu\nu$	10^{-9} MeV	$e^\mp K^\pm$	494 MeV	$\nu\eta'$	958 MeV
$\nu e^+ e^-$	1.02 MeV	$\nu\eta$	548 MeV	$\mu^\mp K^{*\pm}$	997 MeV
$\nu e^\pm \mu^\mp$	105 MeV	$\mu^\mp K^\pm$	559 MeV	$\nu\phi$	1019 MeV
$\nu\pi^0$	135 MeV	$\nu\rho^0$	776 MeV	$\nu e^\pm \tau^\mp$	1776 MeV
$e^\mp\pi^\pm$	140 MeV	$e^\mp\rho^\pm$	776 MeV	$e^\mp D^\pm$	1870 MeV
$\nu\mu^+\mu^-$	210 MeV	$\nu\omega$	783 MeV	$\nu\mu^\pm\tau^\mp$	1880 MeV
$\mu^\mp\pi^\pm$	245 MeV	$\mu^\mp\rho^\pm$	882 MeV	$\tau^\mp\pi^\pm$	1870 MeV
		$e^\mp K^{*\pm}$	892 MeV		

Tab. 4.1: All the available channels for a HNL with a mass below the D_s^\pm mass are listed above, sorted by threshold mass. The active neutrino is considered massless, when compared to the masses of the other particles.

These relations hold at the differential level if the kinematic variables are reinterpreted in the obvious way. In this sense, we can view the Majorana process as the sum of Dirac particle and antiparticle decays.² Considering the total decay rates only, we find that the Majorana decay is larger by a factor of 2 compared to the Dirac case,

$$\Gamma(N \rightarrow \nu X') = 2\Gamma(N_D \rightarrow \nu X') .$$

Note that this is true only for the total decay rates with massless final-state neutrinos.

It is instructive to reconsider this result in the light of the *practical Dirac–Majorana confusion theorem* [115, 116]. In Ref. [115], the decomposition into particle and antiparticle processes was performed for Majorana neutrino–electron scattering via neutral current, leading to a factor of two enhancement in the total rate. However, this enhancement was shown to be absent in practice due to the polarisation of the incoming neutrino, which suppresses the $\Delta L = 2$ contributions by factors of the neutrino mass. In the present case of nearly-sterile decay, where mass effects are large and essential to the calculation, there is no analogous effect: Dirac and Majorana neutrinos will have distinct total decay rates regardless of their polarisation. Therefore, the total decay rates of heavy neutrinos into observable final states could in principle allow us to determine the Majorana/Dirac nature of the initial state. This is not a trivial effect: a pure Majorana state decays with equal probability into $e^-\pi^+$ as $e^+\pi^-$, one of its dominant and most experimentally distinctive branching decay modes, while a Dirac heavy neutrino will only decay into $e^-\pi^+$. Assuming charge-identification is possible in the detector, distinguishing between the two total decay rates should be possible with modest statistics. In a charge-blind search or for an NC channel, the total decay rate of Majorana neutrinos would appear to be twice as large as that of Dirac neutrinos. However, being the mixing usually an unknown quantity, the difference between Majorana and Dirac nature cannot be deduced as easily.

There is also a more subtle impact of the nature of the decaying neutrino. Even though the total decay rate is not affected by the helicity of the initial neutrino, the helicity does affect the distributions

²In a general amplitude with Majorana states, there would also be an interference contribution between these two sub-processes. However, in all cases of interest, interference diagrams are proportional to the final-state light neutrino mass, which we take to be zero.

Fig. 4.1: The branching ratios for HNL decays, integrated over the angular variables, are shown above as functions of the mass. They are grouped in CC-mediated decays (left) and NC-mediated decays (right), in the range from 0.01 MeV up to the maximum mass limit for neutrino production, near 2 GeV. A scenario in which $|U_{eN}|^2 = |U_{\mu N}|^2 = |U_{\tau N}|^2$ is chosen here for illustrative purposes. The branching ratios of Majorana neutrinos and Dirac neutrinos are mathematically identical and therefore no distinction is stressed. The decay into three light neutrinos is fundamental for a correct computation of the branching ratios, even though fully invisible from an experimental point of view.

of final state particles, which will in turn influence the observability of the signatures of neutrino decay. It is important that these polarisation effects are correctly implemented when studying the distributions of final state observables and subsequently when developing an analysis to tackle backgrounds.

In the remainder of this section, we present results for the polarised heavy neutrino decay rates and distributions for Majorana and (pseudo-)Dirac neutrinos. The decay modes considered are listed in Tab. 4.1 and the respective branching ratios as functions of the neutrino mass are shown in Fig. 4.1. The differential widths have been computed using the massive spinor helicity formalism (see *e.g.* Refs. [117, 118]), and checked numerically using FeynCalc [119, 120].

4.2.1 Polarised Majorana neutrino decay

Although spin-averaged Majorana neutrino decay rates are well known in the literature [69, 121, 122] (see also Ref. [123]), to the best of our knowledge the polarised rates are not. These are necessary to correctly describe the distributions of observables in a beam dump experiment, and in this section we present formulae for these differential decay rates.

Note that we stay agnostic as to the final nature and flavours of outgoing neutrinos, and in all cases sum over any possible outgoing states to define a semi-inclusive decay rate into the visible particle(s) X' , *i.e.*

$$\Gamma(N \rightarrow \nu X') \equiv \sum_{i=1}^3 \Gamma(N \rightarrow \nu_i X') .$$

The alternative, chosen by many other authors, is to treat light neutrinos as Dirac particles, and construct the full decay width using arguments of CP invariance, in practice amounting to adding some judicious factors of two [69, 123]. Following this approach, our summed decay rate for $N \rightarrow \nu X'$ can be seen as

$$\Gamma(N \rightarrow \nu X') \equiv \sum_{\alpha=e}^{\tau} [\Gamma(N \rightarrow \nu_\alpha X') + \Gamma(N \rightarrow \bar{\nu}_\alpha X')] .$$

The two approaches are identical mathematical procedures and can both be used to compute the differential decay rates; however, we avoid the latter as the light neutrinos in most seesaw models are Majorana fermions, and making a distinction between ν_α and $\bar{\nu}_\alpha$ is physically misleading.³ We also find that the distribution of events, the role of helicity and the heavy neutrino nature are obscured by this approach. In contrast, by summing over all outgoing states, our formulae are insensitive to the Majorana/Dirac nature of the light neutrinos, and are the physically relevant rates necessary for comparison with beam dump experiments, as outgoing neutrinos are not reconstructed.

Pseudoscalar mesons

The semi-leptonic meson decays are some of the most important channels identified in previous studies [69, 99] (see also Ref. [97]) thanks to their large branching ratios and distinctive final state particles. Both charged and neutral pseudo-scalar mesons are viable final state particles, namely P^\pm and P^0 , and the decay widths are given in the Centre of Mass (CM) frame by

$$\frac{d\Gamma_\pm}{d\Omega_{\ell_\alpha}}(N \rightarrow \ell_\alpha^- P^+) = |U_{\alpha N}|^2 |V_{q\bar{q}}|^2 \frac{G_F^2 f_P^2 m_N^3}{16\pi} I_1^\pm(\xi_\alpha^2, \xi_P^2; \theta_\alpha) , \quad (4.4)$$

$$\frac{d\Gamma_\pm}{d\Omega_{\ell_\alpha}}(N \rightarrow \ell_\alpha^+ P^-) = |U_{\alpha N}|^2 |V_{q\bar{q}}|^2 \frac{G_F^2 f_P^2 m_N^3}{16\pi} I_1^\mp(\xi_\alpha^2, \xi_P^2; \theta_\alpha) , \quad (4.5)$$

$$\frac{d\Gamma_\pm}{d\Omega_P}(N \rightarrow \nu P^0) = \left(\sum_{\alpha=e}^{\tau} |U_{\alpha N}|^2 \right) \frac{G_F^2 f_{P^0}^2 m_N^3}{16\pi} \frac{I_1(0, \xi_P^2)}{4\pi} , \quad (4.6)$$

where Γ_h is the decay rate for neutrinos of helicity h , $V_{q\bar{q}}$ is the appropriate CKM matrix element for the considered meson, f_P is its decay constant and $\xi_i = m_i/m_N$ denotes the mass of the final state particle i as a fraction of the initial state mass. The solid angle elements Ω_{ℓ_α} and Ω_P refer respectively to the charged lepton and pseudo-scalar meson angle with respect to the neutrino direction. The kinematic function $I_1(x, y)$ [69] and its angular generalisation accounting for helicity, $I_1^\pm(x, y; \theta)$, are defined in

³The approach could be seen as a short-hand for decay rates into polarised massless neutrinos, but as we are particularly concerned with polarisation effects in the beam this only adds a further complication.

Appendix A. After integrating over the angular variables, we find that both the pseudo-scalar meson decay rates do not depend on helicity, as expected,

$$\Gamma_{\pm}(N \rightarrow \ell_{\alpha}^- P^+) = \Gamma_{\pm}(N \rightarrow \ell_{\alpha}^+ P^-) = |V_{q\bar{q}}|^2 |U_{\alpha N}|^2 \frac{G_F^2 f_P^2 m_N^3}{16\pi} I_1(\xi_{\alpha}^2, \xi_P^2), \quad (4.7)$$

$$\Gamma_{\pm}(N \rightarrow \nu P^0) = \left(\sum_{\alpha=e}^{\tau} |U_{\alpha N}|^2 \right) \frac{G_F^2 f_P^2 m_N^3}{16\pi} I_1(0, \xi_P^2). \quad (4.8)$$

These rates agree with those presented in Refs. [121, 123] (correcting a factor of two discrepancy in the νP^0 rate of Refs. [69, 122]).

The decay into a neutral meson, in Eq. (4.6), is isotropic in the rest frame, while the charged-pion modes, Eqs. (4.4) and (4.5), inherit their angular dependence from $I^{\pm}(x, y; \theta_{\alpha})$, on the lepton angle to the beam line in the heavy neutrino rest frame θ_{α} . The isotropy of the neutral current decay $N \rightarrow \nu P^0$ is a manifestation of the Majorana nature of the particle, in agreement with the discussion of Ref. [124]. It is worth noting that, if final states are not charge-identified, a similar isotropy is obtained for the total rate of charged semi-leptonic decays,

$$\begin{aligned} \frac{d\Gamma_{\pm}}{d\Omega_{\ell_{\alpha}}}(N \rightarrow \ell_{\alpha} P) &\equiv \frac{d\Gamma_{\pm}}{d\Omega_{\ell_{\alpha}}}(N \rightarrow \ell_{\alpha}^+ P^-) + \frac{d\Gamma_{\pm}}{d\Omega_{\ell_{\alpha}}}(N \rightarrow \ell_{\alpha}^- P^+) \\ &= |U_{\alpha N}|^2 |V_{q\bar{q}}|^2 \frac{G_F^2 f_P^2 m_N^3}{16\pi} \frac{I_1(\xi_{\alpha}^2, \xi_P^2)}{2\pi}. \end{aligned} \quad (4.9)$$

The formulae above apply for all pseudo-scalar mesons which are kinematically allowed. For instance, below the K^0 mass, the heavy neutrino can decay only into pions, but above η and η' can be allowed in the final state.

Vector mesons

Although only for higher masses, HNL can also decay into vector mesons V , both via charged current, $N \rightarrow \ell^{\mp} V^{\pm}$, and neutral current, $N \rightarrow \nu V^0$. We find the following polarised differential distributions in the heavy neutrino rest frame,

$$\frac{d\Gamma_{\pm}}{d\Omega_{\ell_{\alpha}}}(N \rightarrow \ell_{\alpha}^- V^+) = |U_{\alpha N}|^2 |V_{q\bar{q}}|^2 \frac{G_F^2 f_V^2 m_N^3}{16\pi} I_2^{\pm}(\xi_{\alpha}^2, \xi_V^2; \theta_{\alpha}), \quad (4.10)$$

$$\frac{d\Gamma_{\pm}}{d\Omega_{\ell_{\alpha}}}(N \rightarrow \ell_{\alpha}^+ V^-) = |U_{\alpha N}|^2 |V_{q\bar{q}}|^2 \frac{G_F^2 f_V^2 m_N^3}{16\pi} I_2^{\mp}(\xi_{\alpha}^2, \xi_V^2; \theta_{\alpha}), \quad (4.11)$$

$$\frac{d\Gamma_{\pm}}{d\Omega_V}(N \rightarrow \nu V^0) = \left(\sum_{\alpha=e}^{\tau} |U_{\alpha N}|^2 \right) \frac{G_F^2 f_V^2 \kappa_V^2 m_N^3}{16\pi} \frac{I_2(0, \xi_V^2)}{4\pi}, \quad (4.12)$$

where $I_2(x, y)$ and $I_2^\pm(x, y; \theta)$ are defined in Appendix A. We find the total decay widths given by

$$\Gamma(N \rightarrow \ell_\alpha^- V^+) = \Gamma(N \rightarrow \ell_\alpha^+ V^-) = |U_{\alpha N}|^2 |V_{q\bar{q}}|^2 \frac{G_F^2 f_V^2 m_N^3}{16\pi} I_2(\xi_\alpha^2, \xi_V^2) , \quad (4.13)$$

$$\Gamma(N \rightarrow \nu V^0) = \left(\sum_{\alpha=e}^{\tau} |U_{\alpha N}|^2 \right) \frac{G_F^2 f_V^2 \kappa_V^2 m_N^3}{16\pi} I_2(0, \xi_V^2) , \quad (4.14)$$

where the constants κ_V are combinations of the Weinberg angle, depending on the flavour structure of V^0 (see below). Our charged pseudo-vector decay rates agree with Refs. [69, 121–123] while our neutral pseudo-scalar calculation agrees with the corrected version presented in Ref. [123].

As with the pseudo-scalar meson decay rates, the Majorana nature leads to an isotropic decay into a neutral vector meson. An analogous effect holds for the charged vector meson decay if we assume that the charges of final state particles are not distinguished. In this case, we find the physically relevant decay distribution in the particle rest frame to be given by

$$\begin{aligned} \frac{d\Gamma_\pm}{d\Omega_{\ell_\alpha}}(N \rightarrow \ell_\alpha V) &\equiv \frac{d\Gamma_\pm}{d\Omega_{\ell_\alpha}}(N \rightarrow \ell_\alpha^- V^+) + \frac{d\Gamma_\pm}{d\Omega_{\ell_\alpha}}(N \rightarrow \ell_\alpha^+ V^-) , \\ &= |U_{\alpha N}|^2 \frac{G_F^2 f_V^2}{16\pi} |V_{q\bar{q}}|^2 m_N^3 \frac{I_2(\xi_\alpha^2, \xi_V^2)}{2\pi} . \end{aligned} \quad (4.15)$$

There are no vector mesons lighter than the K^0 , and these decays become relevant only for higher masses for which decays into ρ^\pm and $K^{*\pm}$, and for the neutral mode into ρ^0 , ω , and ϕ would be relevant. For these neutral particles, the κ_V factors read

$$\kappa_\rho = 1 - \sin^2 \theta_W , \quad \kappa_\omega = \frac{4}{3} \sin^2 \theta_W , \quad \kappa_\phi = \frac{4}{3} \sin^2 \theta_W - 1 .$$

Charged lepton pairs

We assign the momenta to the particles in the three-body decay as follows

$$N(k_1) \rightarrow \nu(k_2) \ell_\alpha^-(k_3) \ell_\beta^+(k_4) ,$$

and denote $k_i^2 = m_i^2$. The five-dimensional phase space of the final-state particles can be parameterised using two scaled invariant masses,

$$s_1 = \frac{(k_2 + k_3)^2}{m_N^2} \quad \text{and} \quad s_2 = \frac{(k_2 + k_4)^2}{m_N^2} ,$$

as well as three lab-frame angular variables, (θ_3, ϕ_3) , giving the direction of ℓ_α^- and φ_{43} denoting the relative azimuthal angle between ℓ_α^- and ℓ_β^+ . Although $\cos \theta_4$ is not an independent element of our parametrisation, it is a physically relevant quantity and we use it to simplify the presentation of the distributions below. It can be easily related to the fundamental variables $s_1, s_2, \theta_3, \phi_3, \varphi_{43}$. The differential

decay rate is expressed as

$$d\Gamma_{\pm} = \frac{G_F^2 m_N^5}{16\pi^3} (|A_0|^2 \pm |A_1|^2) ds_1 ds_2 \frac{d^2\Omega_3}{4\pi} \frac{d\varphi_{43}}{2\pi}, \quad (4.16)$$

where Ω_3 assumes the conventional meaning and with

$$\begin{aligned} |A_0|^2 &\equiv C_1(s_2 - \xi_3^2)(1 + \xi_4^2 - s_2) + C_2(s_1 - \xi_4^2)(1 + \xi_3^2 - s_1) \\ &\quad + 2C_3\xi_3\xi_4(s_1 + s_2 - \xi_3^2 - \xi_4^2), \end{aligned} \quad (4.17)$$

$$\begin{aligned} |A_1|^2 &\equiv [C_4(s_2 - \xi_3^2) - 2C_6\xi_3\xi_4]\lambda^{\frac{1}{2}}(1, s_2, \xi_4^2) \cos\theta_4 \\ &\quad + [C_5(s_1 - \xi_4^2) - 2C_6\xi_3\xi_4]\lambda^{\frac{1}{2}}(1, s_1, \xi_3^2) \cos\theta_3. \end{aligned} \quad (4.18)$$

The coefficients $\{C_i\}$ are polynomials in chiral couplings and extended PMNS matrix elements, and are given for the decays of interest in Appendix A.1. On integration over the angular coordinates, however, only the $|A_0|^2$ terms remain and we recover the standard expression for the total decay rates through the identities given in Eqs. (A.1), (A.2) and (A.3). The general expression for the total decay rate is again helicity independent and can be written as

$$\Gamma_{\pm} = \frac{G_F^2 m_N^5}{192\pi^3} [C_1 I_1(0, \xi_3^2, \xi_4^2) + C_2 I_1(0, \xi_4^2, \xi_3^2) + C_3 I_2(0, \xi_3^2, \xi_4^2)]. \quad (4.19)$$

The functions $I_1(x, y, z)$ and $I_2(x, y, z)$ are given in Appendix A. Using the expressions for $\{C_i\}$ in Appendix A.1, we find that the total decay rates are given to first order in the heavy-active mixing parameters $U_{\alpha N}$ by

$$\Gamma_{\pm}(N \rightarrow \nu \ell_{\alpha}^- \ell_{\beta}^+) = \frac{G_F^2 m_N^5}{192\pi^3} [|U_{\alpha N}|^2 I_1(0, \xi_{\alpha}^2, \xi_{\beta}^2) + |U_{\beta N}|^2 I_1(0, \xi_{\beta}^2, \xi_{\alpha}^2)], \quad (4.20)$$

$$\begin{aligned} \Gamma_{\pm}(N \rightarrow \nu \ell_{\alpha}^- \ell_{\alpha}^+) &= \frac{G_F^2 m_N^5}{96\pi^3} \sum_{\gamma=e}^{\tau} |U_{\gamma N}|^2 \left\{ (g_L g_R + \delta_{\gamma\alpha} g_R) I_2(0, \xi_{\alpha}^2, \xi_{\alpha}^2) \right. \\ &\quad \left. + [g_L^2 + g_R^2 + \delta_{\gamma\alpha}(1 + 2g_L)] I_1(0, \xi_{\alpha}^2, \xi_{\alpha}^2) \right\}. \end{aligned} \quad (4.21)$$

where $\alpha \neq \beta$, $g_L = -1/2 + \sin^2\theta_W$ and $g_R = \sin^2\theta_W$. Our total decay rates agree with those in Refs. [69, 121–123] and correct a typographical mistake in the rates presented in Ref. [99].

All possible combinations of charged leptons except $\nu\tau^-\tau^+$ are allowed for masses below m_{D_s} . However, because of the limited phase space, the decays into $\nu\tau^{\mp}e^{\pm}$ and $\nu\tau^{\mp}\mu^{\pm}$ can be neglected.

Other decays

There are some other decay rates relevant to this study but not as viable observable channels. First, the total decay width of the process $N \rightarrow \nu\bar{\nu}\nu$, mediated by the Z boson, reads

$$\Gamma(N \rightarrow \nu\bar{\nu}\nu) = \left(\sum_{\gamma=e}^{\tau} |U_{\gamma 4}|^2 \right) \frac{G_F^2 m_N^5}{96\pi^3}. \quad (4.22)$$

Although this decay mode is experimentally invisible, it is the dominant channel up to the pion mass, when two-body semi-leptonic decays open up, and plays a significant role in defining the branching ratios of the observable channels. Our expression agrees with Refs. [69, 121–123]. Secondly, there are other decay modes with small branching ratios and/or complicated final states which we do not study further. These include the one-loop decay into a photon which has received some interest as an observable signature in non-minimal models [60, 61, 125] where it may be enhanced. In the mass models considered in this work, it has a branching ratio of below 10^{-3} and will not be considered. We also neglect the multi-pion decay modes discussed in Ref. [123], which are estimated to have at most a percent level branching ratio and a challenging hadronic final state for reconstruction.

4.2.2 Polarised (pseudo-)Dirac neutrino decay

In this section we compute the decay rates for pseudo-Dirac pairs. It is unlikely that any effect driven by the LNV parameter will be relevant for the discovery potential of DUNE ND and the signatures of these particles will be dominated by the leading order LNC effects. Accordingly, we take the strict Dirac limit in our calculations, rather than treating the states as pseudo-Dirac pairs.

Dirac (anti)neutrino decays

The decay rates for a Dirac heavy (anti)neutrino are similar in form to those presented for the Majorana neutrino. The key differences are lepton number conservation, which acts to forbid certain channels, and differences in the angular distributions of the neutral current decays. For charged current-mediated processes, the distributions for Dirac neutrinos and antineutrinos are mathematically identical to the distributions for Majorana neutrinos. The two-body semi-leptonic decays are the same of Eqs. (4.4) and (4.10),

$$\frac{d\Gamma_{\pm}}{d\Omega_{\ell_\alpha}}(N_D \rightarrow \ell_\alpha^- P^+) = \frac{d\Gamma_{\mp}}{d\Omega_{\ell_\alpha}}(\bar{N}_D \rightarrow \ell_\alpha^+ P^-) = \frac{d\Gamma_{\pm}}{d\Omega_{\ell_\alpha}}(N \rightarrow \ell_\alpha^- P^+), \quad (4.23)$$

$$\frac{d\Gamma_{\pm}}{d\Omega_{\ell_\alpha}}(N_D \rightarrow \ell_\alpha^- V^+) = \frac{d\Gamma_{\mp}}{d\Omega_{\ell_\alpha}}(\bar{N}_D \rightarrow \ell_\alpha^+ V^-) = \frac{d\Gamma_{\pm}}{d\Omega_{\ell_\alpha}}(N \rightarrow \ell_\alpha^- V^+). \quad (4.24)$$

The situation for NC processes is different with respect to Majorana neutrinos. The distribution of the final state particles is not isotropic anymore and it depends on the helicity state of the initial neutrino,

in the way shown by the following differential rates

$$\frac{d\Gamma_{\pm}}{d\Omega_P}(N_D \rightarrow \nu P^0) = \frac{d\Gamma_{\mp}}{d\Omega_P}(\bar{N}_D \rightarrow \bar{\nu} P^0) = \left(\sum_{\alpha=e}^{\tau} |U_{\alpha N}|^2 \right) \frac{G_F^2 f_{P^0}^2 m_N^3}{32\pi} I_1^{\pm}(0, \xi_P^2; \theta_P), \quad (4.25)$$

$$\frac{d\Gamma_{\pm}}{d\Omega_V}(N_D \rightarrow \nu V^0) = \frac{d\Gamma_{\mp}}{d\Omega_V}(\bar{N}_D \rightarrow \bar{\nu} V^0) = \left(\sum_{\alpha=e}^{\tau} |U_{\alpha N}|^2 \right) \frac{G_F^2 f_V^2 \kappa_V^2 m_N^3}{32\pi} I_2^{\mp}(0, \xi_V^2; \theta_V). \quad (4.26)$$

For the three-body leptonic decays, the distribution is expressed in Eq. (4.16) with the relevant coefficients from Appendix A.1. The total decay rates are found to be

$$\Gamma_{\pm}(N_D \rightarrow \nu \ell_{\alpha}^- \ell_{\beta}^+) = |U_{\alpha N}|^2 \frac{G_F^2 m_N^5}{192\pi^3} I_1(0, \xi_{\alpha}^2, \xi_{\beta}^2), \quad (4.27)$$

$$\Gamma_{\pm}(\bar{N}_D \rightarrow \bar{\nu} \ell_{\alpha}^- \ell_{\beta}^+) = |U_{\beta N}|^2 \frac{G_F^2 m_N^5}{192\pi^3} I_1(0, \xi_{\beta}^2, \xi_{\alpha}^2), \quad (4.28)$$

$$\begin{aligned} \Gamma_{\pm}(N_D \rightarrow \nu \ell_{\alpha}^- \ell_{\alpha}^+) &= \frac{G_F^2 m_N^5}{192\pi^3} \sum_{\gamma=e}^{\tau} |U_{\gamma N}|^2 \left\{ (g_L g_R + \delta_{\gamma\alpha} g_R) I_2(0, \xi_{\alpha}^2, \xi_{\alpha}^2) \right. \\ &\quad \left. + [g_L^2 + g_R^2 + \delta_{\gamma\alpha}(1 + 2g_L)] I_1(0, \xi_{\alpha}^2, \xi_{\alpha}^2) \right\}, \end{aligned} \quad (4.29)$$

$$\Gamma_{\pm}(\bar{N}_D \rightarrow \bar{\nu} \ell_{\alpha}^- \ell_{\alpha}^+) = \Gamma_{\mp}(N_D \rightarrow \nu \ell_{\alpha}^- \ell_{\alpha}^+), \quad (4.30)$$

where $\alpha \neq \beta$, $g_L = -1/2 + \sin^2 \theta_W$ and $g_R = \sin^2 \theta_W$. Our total decay rates agree with those in Refs. [69, 121–123].

All decay rates not listed above are forbidden for a Dirac (anti)particle as the combination of production and decay would amount to a LNV process. For the available modes, all NC modes are smaller by a factor of two for a Dirac (anti)neutrino compared to the equivalent Majorana process; however, the major difference we see between the Dirac (anti)neutrino and Majorana distributions is that these NC channels are dependent on the angular variables. These differences in the distributions of the final state particles could be in principle exploited to identify the fermionic nature of the decaying HNL [124].

4.3 Heavy neutrino production

Heavy neutrinos can be produced in a beam dump experiment via the same processes that generate light neutrinos. A proton beam hitting a fixed target typically yields a large number of pions and kaons, and also heavier mesons, the amount of which depends on the energy of the protons and the target choice. A set of magnetic horns is responsible for the focusing of charged pions into a decay pipe; the other short-lived particles are usually unaffected by the deflection. All these secondary particles decay leptonically or semi-leptonically via weak interactions thus creating a neutrino beam. In the standard case of light neutrinos, pions and kaons principally decay into ν_{μ} because two-body electronic modes are disfavoured by helicity suppression. Muons decay in turn into equal numbers of ν_e and $\bar{\nu}_{\mu}$. Other

	Channel	BR (%)	m_N (MeV)		Channel	BR (%)	m_N /MeV
$\pi^+ \rightarrow$	$\mu^+ \nu_\mu$	99.98	33.91	$D_s^+ \rightarrow$	$\tau^+ \nu_\tau$	5.48	191.42
	$e^+ \nu_e$	0.01	139.06		$\mu^+ \nu_\mu$	0.55	1862.63
$K^+ \rightarrow$	$\mu^+ \nu_\mu$	63.56	387.81		$e^+ \nu_e$	0.008	1967.78
	$\pi^0 e^+ \nu_e$	5.07	358.19	$\tau^+ \rightarrow$	$\pi^+ \pi^0 \bar{\nu}_\tau$	25.49	1502.31
	$\pi^0 \mu^+ \nu_\mu$	3.35	253.04		$\bar{\nu}_\tau e^+ \nu_e$	17.82	1776.35
	$e^+ \nu_e$	0.16	493.17		$\bar{\nu}_\tau \mu^+ \nu_\mu$	17.39	1671.20
$K_L^0 \rightarrow$	$\pi^\pm e^\mp \nu_e$	40.55	357.12		$\pi^+ \bar{\nu}_\tau$	10.82	1637.29
	$\pi^\pm \mu^\mp \nu_\mu$	27.04	252.38				
$\mu^+ \rightarrow$	$\bar{\nu}_\mu e^+ \nu_e$	100.00	105.14				

Tab. 4.2: Production channels at beam dump facilities yielding neutrinos, with the respective branching ratios (taken from Ref. [?]). The last column shows the maximum neutrino mass allowed if a massive state is produced. On the left, all the decays yielding ν_e , ν_μ , and $\bar{\nu}_\mu$ up to the K^0 mass are shown. On the right, the neutrino sources which depends on the D_s^+ decay chain are shown; only the first four decays of the τ lepton are considered in this work.

production sources of ν_e are the three-body decays of K^0 and K^+ . Above the neutral kaon mass, the first sizeable source of neutrino is given by the D_s meson, for which helicity suppression again favours the production of heavy charged-leptons, and so τ leptons and ν_τ are more likely to be emitted than the other flavours. Each of the subsequent τ^+ decays produces a $\bar{\nu}_\tau$. We consider only the four most probable decay modes of the τ lepton, as they provide a sufficient description of their contribution to the overall flux.⁴

If kinematically allowed, heavy neutrino states can be sourced from these decays of mesons and charged leptons. We show in Tab. 4.2 all the neutrino production channels considered in this analysis, reporting the heaviest neutrino mass m_N that is accessible by kinematics. The neutrino mass range we consider goes from a few MeV up to the D_s meson mass. To estimate the flux of heavy neutrinos produced, we start from the flux of light neutrinos, scaling it by an energy-independent kinematic factor. Given a certain SM neutrino production process, $Q \rightarrow \nu_\alpha Q'$, we use as scale factor the ratio between the decay width of the same process producing massive neutrinos, $Q \rightarrow NQ'$, and the rate of the SM decay with light neutrinos. The full flux of nearly-sterile neutrinos with a given helicity is therefore a linear combination of the different neutrino flux components, $\phi_{Q \rightarrow \nu_\alpha}$, summing over all existing parents and all allowed flavours:

$$\frac{d\phi_N^\pm}{dE}(E_N) \approx \sum_{Q,\alpha} \mathcal{K}_\pm^{Q,\alpha}(m_N) \frac{d\phi_{Q \rightarrow \nu_\alpha}}{dE}(E_N - m_N), \quad (4.31)$$

where

$$\mathcal{K}_\pm^{Q,\alpha}(m_N) \equiv \frac{\Gamma_\pm(Q \rightarrow NQ')}{\Gamma(Q \rightarrow \nu_\alpha Q')}.$$

The ratio \mathcal{K} is proportional to the mixing parameter $|U_{\alpha N}|^2$ and contains only kinematic functions of the involved masses. These are responsible for correcting phase space and helicity terms.

The helicity state plays a fundamental role in the production rate, in contrast with the case of neutrino decays, since there is no arbitrariness in the polarisation direction this time: it is defined by

⁴The decay $\tau^+ \rightarrow \bar{\nu}_\tau \pi^+ \pi^0$ is studied only at the level of phase space sampling in this work.

Fig. 4.2: The scale factors separated by helicity components are shown. In two-body decays (left), the $h = -1$ components (dashed) for all channels do not depend on the mass. The enhancement is driven by the $h = +1$ components (dotted), which are the dominant contribution of the unpolarised factors (solid). In three-body decays (right), there are two different scale factors for purely leptonic decays, noted as $\ell_\alpha \rightarrow \ell_\beta$: if the decay is mediated by $|U_{\beta N}|^2$, for which the $h = -1$ (dashed) and the $h = +1$ (dotted) components are comparable, and if the decay is mediated by $|U_{\alpha N}|^2$, for which $h = -1$ dominates over the $h = +1$ (dotdashed). In both cases, the two parts sum up to the same quantity (solid). The kaon decays are also divided in $h = -1$ (dashed) and $h = +1$ (dotted) components; $\tau^+ \rightarrow \nu \pi^+ \pi^0$ is studied only at the phase space level.

the neutrino momentum in the rest frame of the parent particle. We employ the massive spinor helicity formalism to compute the production decay rates for both Majorana and Dirac neutrinos, and these are used to build the scale factors for each neutrino helicity. Even though lepton number is preserved differently in the two cases and different Feynman rules hold, all the production channels of interest in this work are mediated by charge currents and therefore the rates are mathematically identical for Majorana and Dirac neutrinos. If the neutrino is Dirac, the production decay width for an antineutrino with given helicity is the same as the one of the neutrino, but with opposite helicity. The phenomenology of the scale factors is different for two-body decays and three-body decays and therefore we group them, respectively, in Section 4.3.1 and Section 4.3.2.

4.3.1 Two-body decays

A massless neutrino (antineutrino) has its chiral and helicity states degenerate, and so it is always produced with a negative (positive) helicity. It follows that the component of the light neutrino beam produced in two-body decays of pseudo-scalar mesons is polarised. The initial spin, which is zero, must be preserved in the decay, and since the helicity of the neutrino in the rest frame is fixed, the accompanying lepton is produced with a “wrong” helicity. This is permitted by the non-zero mass of the charged lepton and therefore final states with light flavour leptons undergo helicity suppression. As soon as the neutrino mass deviates from zero, the correspondence between chirality and helicity is lost and the neutrino can be produced with both polarisations. The main consequence is that the production of heavy neutrinos from light flavour mixings (electron) appears to be enhanced with respect to heavy flavours (muon and tau). The effect is particularly dramatic when the mass difference between parent meson and charged lepton widens, as it happens with the electron decay of D_s , the enhancement of which is around 10^6 for neutrino masses near 1 GeV.

The scale factor \mathcal{K}_h for leptonic decays of a pseudo-scalar meson P into neutrinos with helicity h , is given by the analytic expression:

$$\mathcal{K}_{\pm}^{P,\alpha}(m_N) = |U_{\alpha N}|^2 \frac{\lambda^{\frac{1}{2}}(1, \xi_N^2, \xi_{\ell_\alpha}^2) [\xi_{\ell_\alpha}^2 + \xi_N^2 - (\xi_N^2 - \xi_{\ell_\alpha}^2)^2 \pm (\xi_N^2 - \xi_{\ell_\alpha}^2) \lambda^{\frac{1}{2}}(1, \xi_N^2, \xi_{\ell_\alpha}^2)]}{2 \xi_{\ell_\alpha}^2 (1 - \xi_{\ell_\alpha}^2)^2}, \quad (4.32)$$

where λ is the Källén function:

$$\lambda(a, b, c) = (a - b - c)^2 - 4bc,$$

and $\xi_i = m_i/m_X$ is the mass ratio of the final state particle i over the parent particle mass. When summing over the helicity states, the resulting factor coincides with the one computed in Ref. [126]:

$$\mathcal{K}^{P,\alpha}(m_N) = \sum_{h=\pm 1} \mathcal{K}_h^{P,\alpha}(m_N) = |U_{\alpha N}|^2 \frac{\lambda^{\frac{1}{2}}(1, \xi_N^2, \xi_{\ell_\alpha}^2) [\xi_{\ell_\alpha}^2 + \xi_N^2 - (\xi_N^2 - \xi_{\ell_\alpha}^2)^2]}{\xi_\alpha^2(1 - \xi_{\ell_\alpha}^2)^2}.$$

In order to understand the effect of Eq. (4.32), it is convenient to define the fraction of neutrinos produced with a certain helicity as

$$S_{\pm} = \frac{\mathcal{K}_{\pm}^{P,\alpha}}{\mathcal{K}_{+1}^{P,\alpha} + \mathcal{K}_{-1}^{P,\alpha}} = \frac{1}{2} \left[1 \pm \frac{(\xi_N^2 - \xi_{\ell_\alpha}^2) \lambda^{\frac{1}{2}}(1, \xi_N^2, \xi_{\ell_\alpha}^2)}{\xi_{\ell_\alpha}^2 + \xi_N^2 - (\xi_N^2 - \xi_{\ell_\alpha}^2)^2} \right].$$

In the limit of a massless neutrino, i.e. $\xi_N \rightarrow 0$, the fractions are $S_+ \rightarrow 0$ and $S_- \rightarrow 1$, as expected: all neutrinos are produced with a negative helicity. The opposite is true when the charged lepton is in the massless limit, and the neutrinos are produced with a positive helicity.

The only two-body decay of a lepton considered in this work is $\tau \rightarrow \nu_\tau \pi$, and the scale factor is:

$$\mathcal{K}_{\pm}^{\tau,\pi}(m_N) = |U_{\tau N}|^2 \frac{\lambda^{\frac{1}{2}}(1, \xi_N^2, \xi_\pi^2) [(1 - \xi_N^2)^2 + \xi_\pi^2(1 + \xi_N^2) \mp (1 - \xi_N^2)\lambda^{\frac{1}{2}}(1, \xi_N^2, \xi_\pi^2)]}{2(1 - \xi_\pi^2)^2}. \quad (4.33)$$

The structure is similar to the scale factor for pseudo-scalar meson two-body decays, given in Eq. (4.32), and analogous considerations as above can be deduced. This is explained by crossing symmetries, as the matrix element of the process is the same. In this case, however, the positive helicity component does not lead to any enhancement before the phase space cut-off.

The effect of the scale factors as a function of the neutrino mass can be appreciated in Fig. 4.2, where not only helicity terms are corrected, resulting in an enhancement of the production, but also the phase space is properly adjusted.

4.3.2 Three-body decays

Scale factors for three-body decays are defined in the same way as two-body decay ones. Because of the different number of degrees of freedom, the helicity of the outgoing neutrinos is not fixed by the spin of the parent particles. Hence, these factors are not responsible for any enhancement in the decay rate, but they only quench the process as the neutrino mass upper limit is approached (see Tab. 4.2). The scale factors have nonetheless distinct behaviours depending on the helicity state involved. Their behaviour is plotted as a function of the heavy neutrino mass in Fig. 4.2.

The decay of a charged lepton (antilepton) of flavour α to a charged lepton (antilepton) of flavour β can be proportional to either $|U_{\alpha N}|^2$ or $|U_{\beta N}|^2$, producing a heavy Dirac neutrino (antineutrino) in the first case or an antineutrino (neutrino) in the second case. If the neutrino is Majorana, the decay can occur via both mixing matrix elements because lepton number can be violated. Decays of muons

and taus yield massive neutrinos with the following decay rate

$$\Gamma_{\pm}(\ell_{\alpha}^{+} \rightarrow \ell_{\beta}^{+} \nu N) = \frac{G_F^2 m_{\alpha}^5}{192\pi^3} \left[|U_{\alpha N}|^2 I_{\ell}^{\pm}(\xi_N^2, \xi_{\ell_{\beta}}^2, 0) + |U_{\beta N}|^2 I_{\bar{\ell}}^{\pm}(0, \xi_{\ell_{\beta}}^2, \xi_N^2) \right], \quad (4.34)$$

where the integrals $I_{\ell, \bar{\ell}}(x, y, z)$ are given in Appendix A. The helicity decompositions in I_{ℓ} and $I_{\bar{\ell}}$ are different, but the spin-averaged decay width is the same.

Neutral and charged kaons produce neutrinos in three-body semi-leptonic decays. Both of them can decay into either a muon or an electron and a charged pion if the decaying kaon is neutral or a neutral pion if the kaon is charged. The decay width of a pseudo-scalar meson h_1 to a lighter meson h_2 is given by

$$\Gamma_{\pm}(h_1^{+,0} \rightarrow h_2^{0,+} \ell_{\alpha}^{+} N) = \frac{G_F^2 m_h^5}{128\pi^3} |U_{\alpha N}|^2 |V_{q\bar{q}}|^2 I_{h_1}^{\pm}(\xi_{h_2}^2, \xi_{\ell_{\alpha}}^2, \xi_N^2). \quad (4.35)$$

The integral $I_h(x, y, z)$ is reported in Appendix A and consists of a combination of kinematic elements with terms of hadronic form factors as coefficients. The scale factor was checked numerically against the result of Ref. [127].

The final three-body decay studied in this work is $\tau^+ \rightarrow \bar{\nu}_{\tau} \pi^+ \pi^0$, however this channel is introduced only at the phase space level. The scale factors for the two helicity components are therefore assumed to be identical, $\mathcal{K}_{\pm} = \frac{1}{2}$, such that the neutrino flux sub-component coming from this decay consists of equal number of heavy neutrinos with helicity $h = +1$ and $h = -1$.

Chapter 5

HNL discovery with the DUNE experiment

Heavy nearly-sterile neutrinos are a common ingredient in extensions of the Standard Model which aim to explain neutrino masses, like for instance in Type I seesaw models, or one of its variants. If the scale of the new Heavy Neutral Leptons (HNLs) is sufficiently low, observable signatures can arise in a range of current and upcoming experiments, from the LHC to neutrino experiments. In this article, we discuss the phenomenology of sterile neutrinos in the MeV to GeV mass range, focusing on their decays. We embed our discussion in a realistic mass model and consider the resulting implications. We focus in particular on the impact on the signal of the strong polarisation effects in the beam for Majorana and (pseudo-)Dirac states, providing formulae to incorporate these in both production and decay. We study how the Near Detector of the upcoming Deep Underground Neutrino Experiment can constrain HNL states by searching for their decay products inside the detector. We conduct a Monte Carlo background analysis for the most promising signatures, incorporating the detector’s particle identification capabilities, and estimate the experimental sensitivity of DUNE to these particles. We also present an estimate of the ν_τ -derived HNL flux at DUNE, currently missing in the literature, which allows us to discuss searches for HNLs at higher masses.

5.1 Liquid argon time projection chamber

5.2 The DUNE experiment

5.3 Simulation of events at DUNE ND

DUNE [100] is a long-baseline oscillation experiment that will study neutrino physics in great detail, focusing mainly on the determination of the CP violating phase, δ_{CP} , of the mass ordering, and on the precision measurement of other oscillation parameters, in particular θ_{23} . These goals can be achieved

thanks to both an intense neutrino beam and a high-resolution Far Detector (FD), consisting of a 40 kt Liquid Argon Time Projection Chamber (LArTPC), situated 1300 km from the beam target. The drift velocity of ionised electrons in LAr, typically of the order of cm/ μ s, can be controlled with sufficient precision, by tuning the electric field, to result in high spatial resolution for event reconstruction [128]. A very sensitive FD alone, however, is not enough due to numerous uncertainties on neutrino flux and cross sections. A smaller and closer detector, called Near Detector (ND), is therefore adopted to normalise the flux of neutrinos reaching the FD and to help cancel out many of the neutrino-nucleon cross section systematics.

The DUNE ND will be placed 574 m from the target. Its final design has not been finalised yet, but it will likely be a hybrid concept, consisting of a small LArTPC placed in front of a magnetised high-pressure gaseous TPC. This module is complementary to the front detector, controlling escaping or below-threshold particles from the LArTPC, but is also capable of performing standalone measurement. For its versatile nature, it is called Multi-Purpose Detector (MPD). The sub-system LArTPC/MPD will be movable inside the ND hall—following the DUNE-PRISM concept—for better profiling the neutrino flux at different angles. There will be a third module, a 3D Scintillation Tracker (3DST), on-axis, to monitor the stability of the beam flux and neutron contamination. Currently, the proposed fiducial volume for the LArTPC module is 24 m³ (around 35 t of LAr), employing the ArgonCube technology [?], whereas the design for the MPD is based on the TPC in ALICE [129], a cylinder of 100 m³ with gas at a pressure of 10 atm and a fiducial mass of 1 t. The 3DST is designed to have a fiducial mass of around 8.7 t of plastic scintillating material and wavelength shifting plates. For this analysis, we take only in account the two core sub-detectors, the LArTPC and the MPD. The main difference between these two ND modules is that the gaseous TPC has a larger volume than the LArTPC. This feature is favourable for studying rare events, like heavy neutrino decays, because more neutrinos enter the fiducial volume. Furthermore, the lower density of the MPD helps reduce the number of neutrino scattering events, which are background to rare signatures. Apart from volume and density differences and relative positions in the detector hall, we treat the two ND units as with similar detection performances, on-axis, and do not take in account the magnetisation of the gaseous TPC.

Thanks to its proximity to the accelerator, the ND will be exposed to an extremely intense neutrino beam, with a flux peak around five million times greater than at the FD. The Long Baseline Neutrino Facility (LBNF) at Fermilab will deploy a very energetic beam of protons, extracted from the Main Injector (MI) and delivered to a graphite target. The collision produces secondary particles, which are collimated by a focusing horn system and then decay forming a neutrino beam. Assuming an 80 GeV proton beam at 1.2 MW for the first six years and at 2.4 MW for a second set of six years [100], the ND will collect in both neutrino and antineutrino mode a total of 2.65×10^{22} POT over the runtime of the experiment. In this work we consider only the beam in the neutrino mode configuration, which corresponds to half of the total runtime, or 1.32×10^{22} POT. The same study of this article can be

	PS191	DUNE ND	SBND	NA62	SHiP
Baseline	128 m	574 m	110 m	220 m	60 m
Volume	216 m ³	124 m ³	80 m ³	750 m ³	590 m ³
Energy	19.2 GeV	80 GeV	8 GeV	400 GeV	400 GeV
POT	0.86×10^{19}	1.32×10^{22}	6.6×10^{20}	3×10^{18}	2×10^{20}
Exposure	1.0	193.5	16.1	8.5	5820

Tab. 5.1: Comparison between experiments mentioned in this work. The exposure is defined as $\text{POT} \times \text{Energy} \times \text{Volume} \times \text{Baseline}^{-2}$ with respect to PS191, where “Energy” is the proton beam energy. The NA62 and SHiP experiments are not directly comparable with SBND and DUNE ND, in that different technologies are involved; the RICH detectors are adopted as fiducial volume for NA62, whereas for SHiP, we estimate the volume as the cone contained in the “hidden sector” vacuum vessel. The volume is a driving feature in the definition of the total exposure and it is of utter importance for searches of decay-in-flight events.

applied equally to the beam in reversed horn current configuration, but its details are not available to us. Including the analysis for the beam in antineutrino mode should result in an increment on the overall sensitivity, approximately a factor of two better.

A summary of the features of the ND system is reported in Tab. 5.1, where it is compared to other beam dump experiments: PS191 [81, 82], SBND which is the detector of the SBN programme with the best sensitivity to HNL [99], NA62 [130], and SHiP [131]. We define the total exposure of the experiment as the proton accelerator beam power, integrated over the total run time, and scaled by the volume of the detector over its baseline squared. The beam power times the run time corresponds to the number of protons on target (POT) times the proton energy. With this definition, an exposure twelve times bigger is expected for the DUNE ND system with respect to SBND, and around two hundred times bigger than PS191. The NA62 and SHiP experiments have a different design and are not directly comparable to TPC and tracker experiments, but we report them here for thoroughness. The estimated exposure of NA62 is limited by its number of POT and by just one year of data taking; despite this fact, the experiment is optimised to study kaon decays and has good sensitivity to HNL [132]. The SHiP experiment presents an exposure thirty times bigger than DUNE ND, but the detector is specifically designed to search for BSM physics, including heavy neutrinos [133] (see also Ref. [134]). The decay-in-flight search hugely benefits from its 50 m long decay vessel and short baseline.

On the collider physics frontier, the FASER experiment [135] will perform a dedicated search for extremely weakly-interacting particles, like HNLs for which it presents interesting sensitivity [136]. The detector consists of a 10 m cylindrical decay volume located 480 m downstream of the ATLAS interaction point.

5.3.1 Flux prediction

In order to implement our analysis, the various components of the flux by parentage must be known separately. We study only the beam operating with a forward horn current, which selects positively charged secondary particles and results in a beam dominantly made of neutrinos with a smaller component of antineutrinos. The flux predictions for ν_e , ν_μ , and $\bar{\nu}_\mu$, provided by Ref. [?] for the reference

Fig. 5.1: The prediction of neutrino fluxes, in neutrino mode, divided by parentage at the ND are shown above, normalised to 10^{20} POT. The ν_e component (top left) predominately originates from μ^+ decays; kaon decays are responsible for the high energy part of the spectrum. The ν_μ component (top right) obtains its main contribution from π^+ decays at low energies, whereas the K^+ decays are accountable for the long tail of the spectrum. Contributions from D_s^+ decay are out of scale for both ν_e and ν_μ . The distribution of the $\bar{\nu}_\mu$ component (bottom left) is due to negative charged secondary particles which are not successfully deflected by the horn system; the muon contribution is much more relevant than for the ν_μ component. The ν_τ component (bottom right) is only sourced from D_s decays and presents a prominent peak at low energies, whereas the $\bar{\nu}_\tau$ are produced in τ^+ lepton decays. The dotted black line is the total $\bar{\nu}_\tau$ component of the flux.

Fig. 5.2: The fluxes of heavy neutrinos from $D_s^+ \rightarrow \tau^+ N$ (left) are presented for different neutrino masses and normalised to 10^{20} POT at the ND. Only phase space effects are considered here. For each different value of the neutrino mass, information on the start and end point of the spectrum and the peak of the flux are extracted and used to reshape the ν_τ spectrum. We show the distortion factors used in the scaling process for the channel producing $\bar{\nu}_\tau$: the energy range normalised to 20 GeV (middle) and the inverse of the peak re-scaling (right).

beam, are shown in Fig. 5.1 subdivided in their parent components. The ν_μ flux is the dominant component and is principally originated by pion decays, whilst its long tail comes from kaon decays. Unsuccessfully deflected negative particles, like π^- or K^- , and the μ^+ are the main contributors to the $\bar{\nu}_\mu$ components, and ν_e comes predominately from the muon and both K^+ and K^0 decays. We consider only the energy range $E < 20$ GeV, because it is the most intense region of the flux and, as it will be explained in Section 5.3.3, the most relevant for this study.

We highlight here the fact that we expect also an albeit-small flux of HNLs with masses above the kaon one. This could be inferred from the ν_τ flux, but this is not available in the literature. In fact, the lightest meson with an interesting decay width to tau neutrinos is the charmed-strange meson D_s^+ , which has a mass $m_{D_s} = 1968.34 \pm 0.07$ MeV [?]. It decays into $\tau^+ \nu_\tau$ with a branching ratio of 5.48 ± 0.23 %. HNL with masses above the K^0 can be produced via the tau mixing, but more importantly via the muonic and electronic ones which are enhanced, as shown in Section 4.3. The meson D^+ also decays into $\tau^+ \nu_\tau$, but being lighter than the D_s^+ , the decay is disfavoured by the smaller phase space, with a branching ratio 50 times smaller. This meson presents three-body decay channels into ν_e and ν_μ with much higher branching ratio, but there is no enhancement for such channels into HNL, as explained in Section 4.3, and so these subdominant components are not taken in account in the present study.

The proton beam has a relatively low energy for producing charm quarks with a high cross-section, so the prediction of ν_τ has not been carried out by the collaboration to the best of our knowledge. For the reasons stated above, we make a prediction for the D_s^+ production by an 80 GeV proton beam hitting a fixed graphite target. The distribution at the production site will be then used to estimate the ν_τ flux at the ND system. In the literature, the following parametrisation has been successfully used to describe the charm meson production in proton-proton collision in the Centre of Mass frame [137]

$$\frac{d^2\sigma}{dx_F dp_T^2} \sim (1 - |x_F|)^n e^{-bp_T^2}, \quad (5.1)$$

where $x_F = 2p_z/\sqrt{s}$, with p_z the longitudinal momentum in the CM frame. The parameters n and b

	CC events			NC events		
	Per tonne	Ratio	Rate (Hz)	Per tonne	Ratio	Rate (Hz)
ν_e	3.0×10^3	75.6 %	6.6×10^{-3}	1.0×10^3	24.4 %	2.1×10^{-3}
ν_μ	240×10^3	75.2 %	530×10^{-3}	79.0×10^3	24.8 %	170×10^3
$\bar{\nu}_\mu$	17.8×10^3	70.9 %	40×10^{-3}	7.3×10^3	29.1 %	16×10^{-3}
ν_τ	7.4×10^{-6}	17.4 %	1.6×10^{-11}	3.5×10^{-5}	82.6 %	7.7×10^{-11}
$\bar{\nu}_\tau$	2.1×10^{-5}	45.3 %	4.7×10^{-11}	2.6×10^{-5}	54.7 %	5.7×10^{-8}

Tab. 5.2: The expected rates for CC and NC interaction in the near detector are presented here, normalised to 10^{20} POT. The values were computed starting from Eq. (5.2), convolving the fluxes of Fig. 5.1 with the CC and NC cross section predictions from GENIE [140]. Detector efficiencies are not applied. The first columns show the total number of events per tonne of argon, the second ones the proportion of CC or NC events with respect to the totality, and the last columns the event frequencies assuming 2.205×10^{14} POT/s.

were fitted from the E769 experiment and found to be $n = 6.1 \pm 0.7$ and $b = 1.08 \pm 0.09$ [138]. We assume that the D_s^+ meson production at the target follows the same distribution. With the help of a Monte Carlo simulation, we generate the D_s^+ four-momenta starting from Eq. (5.1) and simulate the meson decay and the subsequent tau decays. A key simplification here is that because of the short lifetime of the D_s^+ and τ^+ , of the order of 10^{-13} s, their path is not affected by the horn system nor by interactions with other accelerator components. This results in no focusing of these secondary particles, and so only neutrinos emitted within the geometric acceptance of the ND are considered to form the ν_τ and $\bar{\nu}_\tau$ spectrum. The overall normalisation comes from an open charm calculation (see Appendix B for details): the number of D_s^+ per POT is found to be $(2.8 \pm 0.2) \times 10^{-6}$. The result of the simulation is reported in the bottom right panel of Fig. 5.1, where the different contributions to the ν_τ spectrum are shown. Thanks to the large number of POTs in DUNE, the total number of D_s^+ mesons produced is comparable to other dedicated experiments [139]; however, the beamline design is not optimised for heavy mesons production and the ν_τ flux seen at the ND is strongly attenuated.

Having knowledge of the parent meson distribution, we directly simulate the production of nearly-sterile neutrinos from the D_s decays. The spectrum of heavy neutrinos is distorted when their mass approaches the various phase space thresholds, which appears as a further enhancement of the flux. This is because heavier neutrinos are more easily boosted inside the geometric acceptance of the detector. Besides the peak height, the start and the end point of the energy flux are also affected, as illustrated in Fig. 5.2. We take these effects in account, modifying the scaled neutrino flux using information retrieved by the ν_τ and $\bar{\nu}_\tau$ simulation.

5.3.2 Background evaluation

The number of SM neutrino–nucleon interactions expected at the DUNE ND, without considering detector effects, is calculated by integrating the Charged Current (CC) and Neutral Current (NC) total cross sections multiplied by the light neutrino spectrum $d\phi_\nu/dE$:

$$\mathcal{N}_{\text{tot}} = \mathcal{N}_{\text{CC}} + \mathcal{N}_{\text{NC}} = \mathcal{N}_{\text{target}} \int dE [\sigma_{\text{CC}}(E) + \sigma_{\text{NC}}(E)] \frac{d\phi_\nu}{dE}, \quad (5.2)$$

Particle	Threshold	σ_{rel}	σ_θ
EM	30 MeV	$15\%/\sqrt{E} \oplus 2\%$	1°
Hadron	50 MeV	$30\%/\sqrt{E} \oplus 5\%$	5°
Muon	30 MeV	5% or 30% of $ \mathbf{p} $	1°
Pion	100 MeV	5% or 30% of $ \mathbf{p} $	1°

Tab. 5.3: The table lists detection thresholds and energy/momentum and angular resolutions used in the fast MC, where “EM” delineates electro-magnetic showers and “Hadron” any other charged particle which is neither a lepton nor a pion. The momenta of pions and muons are smeared according to the containment of their tracks. If more than 95 % of their track is reconstructed then the relative resolution on the momentum is 5 %, otherwise a resolution of 30 % is assumed.

where $\sigma_{\text{CC}}(E)$ and $\sigma_{\text{NC}}(E)$ are the cross section predictions in argon calculated with GENIE [140], and N_{target} is the total number of Ar targets. The event rates are shown in Tab. 5.2. It turns out that less than one ν_τ event is expected in the total run of the experiment. As a comparison, the number of ν_μ events will be 10^{10} times higher. This confirms the expectations that the ν_τ component of the flux is negligible for standard oscillation physics in DUNE ND. On the other hand ν_τ appearance is expected at the FD.

These neutrino scatterings occurring within the fiducial volume of the detector could mimic the rare signal of neutrino in-flight decays, as some final state particles are common to both processes. A good estimate of the number of possible background events for each discovery channel is very important, since it dictates the true sensitivity of the experiment. We restrict our conservative background analysis to decay modes available for neutrino masses below m_{K^0} , being these the channels with the best discovery potential. They are $N \rightarrow \nu e^+ e^-$, $\nu e^\pm \mu^\mp$, $\nu \mu^+ \mu^-$, $\nu \pi^0$, $e^\mp \pi^\pm$, and $\mu^\mp \pi^\pm$. Particles are typically tagged by studying the topology of the tracks and the energy loss dE/dx in the active medium, but instead of dealing with a full detector simulation, we perform a fast Monte Carlo analysis, using as input neutrino–nucleon scattering events in argon generated by the neutrino event generator GENIE [140]. The tracks are randomly placed inside the ND system and then smeared according to a normal distribution centred on the simulated value of energy/momentum; particles with a kinetic energy above the detection threshold are then assumed to be reconstructed. The relative position between the two detectors is taken into account, in that particle tracks exiting the LArTPC end entering the FGT are reconstructed as a single track. Escaping or partially reconstructed tracks are not discarded, but treated with a different energy/momentum resolution: the initial particle energy can be estimated, with some limitations, thanks to the energy dependence of the mean energy loss during the particle propagation. We then implement possible sources of background mis-identification which are channel specific. Detector resolutions and thresholds, from Ref. [141] for both parts of the ND, are summarised in Tab. 5.3.

A strong discriminant for background events is the presence of protons, neutrons, and other hadrons in the final states, which are the results of the nucleus recoil of the neutrino interaction. If hadronic activity is reconstructed as an interaction vertex, then the event is clearly originated by SM neutrino–nucleon scattering and tagged as background. In the case this does not happen, for instance when the hadrons are below threshold, the multiplicity of final state particles becomes fundamental to distinguish

signal events from intrinsic background. However, this background can be worsened by mis-identification of certain tracks.

The main background to the pseudo-scalar meson channels, $N \rightarrow \ell^\mp\pi^\pm$, are resonance ν_e or ν_μ -CC interaction with single pion production or incoherent and deep inelastic scatterings in which only a pair $\ell\pi$ is detected. Three-body lepton decays suffers from mis-identification of additional pions and photons emitted in CC neutrino scatterings which are mistaken for charged leptons. Despite having a similar mass, pion and muon tracks differ on average in length, as the meson track often culminates in a hadronic shower. In our implementation of the detector effects, if no hadronic shower is detected and the track length is longer than two metres, the pion is identified as a muon. Electromagnetic shower induced by photons are identified by looking at the vertex displacement and at the dE/dx , which is twice as large as the energy loss for e^\pm . If a photon converts within two centimetres from the interaction point, and either the electron or the positron of the pair is below threshold, the photon is reconstructed as a single electron. A pair of electrons with a small separation angle, less than 3° , is tagged as an electron-positron pair and the parent photon is reconstructed. The main source of photons comes from the decay of the neutral pion, which is abundantly produced in neutrino–nucleon interactions. Certain hadronic transitions from secondary particles of deep inelastic scatterings also emit gammas. If a pair of photons shows an invariant mass comparable with the π^0 mass, the parent pion is identified. Interactions in which multiple neutral pions are produced, but only a pair of photons is detected and reconstructed, can be background to the $N \rightarrow \nu\pi^0$ channel. The background events surviving particle identification are between 5 % down to 0.01 % of the processed events, the rejection of which strongly depends on the analysed channel.

The channels which open up for masses above the kaon mass are more challenging from an experimental point of view. The final state particles of these modes are mostly neutral pseudo-scalar mesons, which decay electromagnetically, or vector mesons, which usually decay into a multi-state of lighter mesons, depending on the initial flavour content, sometimes accompanied by photon emission. The correct identification of these short-lived states is non trivial. For very high masses, also τ leptons are yielded, but their precise reconstruction requires *ad hoc* techniques. These tasks are beyond the scope of the analysis presented here and are best left to the collaboration superior simulation tools. We also do not consider cosmogenic background, even though a rate of $2.7\text{Hz}/\text{m}^2$ cosmic rays is expected at the ND hall [?], which has very little over burden. Given an area of a few square meters, the number of cosmic rays per drift window can be non-negligible [100], but rejection techniques are being developed with good signal efficiencies [142].

5.3.3 HNL decay events and signal efficiency

Except for N decaying into three neutrinos, all the other decay channels are in principle detectable. For a given visible decay mode d , the number of signal events is

$$\mathcal{N}_d = \int dE \Pi_d(E) W_d(E) \frac{d\phi_N}{dE} , \quad (5.3)$$

where $d\phi_N/dE$ is the number of heavy neutrinos expected at the ND, computed in the way described in Section 4.3. The function $\Pi_d(E)$ accounts for the probability of a heavy neutrino of energy E to decay inside the ND after covering the baseline distance L . It is expressed in the following form:

$$\Pi_d(E) = e^{-\frac{\Gamma_{\text{tot}}L}{\gamma\beta}} \left(1 - e^{-\frac{\Gamma_{\text{tot}}\lambda}{\gamma\beta}}\right) \frac{\Gamma_d}{\Gamma_{\text{tot}}} , \quad (5.4)$$

where λ is the length of the ND, Γ_d the decay rate for the channel d and Γ_{tot} the total decay rate. The total effect of Π_d is to favour low-energy bins of the neutrino spectrum for which the relativistic factor $\gamma\beta$ is small.

The term $W_d(E)$ is a signal efficiency factor, estimated as the binned ratio of the true N energy spectrum after and before a background rejection procedure. The latter is a process aiming to further reduce the number of background events still present after particle identification. It consists of simple data selection cuts optimised to reject the background while minimising the loss of signal events, exploiting differences in the energy and angular distributions of signal and background events. The HNL decays inside the detector are simulated by a custom Monte Carlo code and the tracks are processed in the same way as it is done for background events (see Section 5.3.2). The resulting signal efficiency therefore embeds also detector effects. If no background is expected for the channel d , there is no need for applying any rejection procedure and so the signal efficiency is maximal, i.e. $W_d(E) = 1$ at all energies. The final number of background events \mathcal{B}_d and the number of signal events \mathcal{N}_d are eventually used to build the Confidence Level (C.L.) regions of sensitivity (see Section 5.4). We leave a more detailed discussion on the background reduction cuts in Appendix 5.6, where we report the rates of background reduction and signal selection for all decay channels of both Majorana and Dirac neutrinos of a given mass. We note that the Dirac neutrino decays generally have a lower signal efficiency, between 5% and 10% less, compared to a Majorana state of the same mass. This is a consequence of certain combinations of production and decay modes which are forbidden for Dirac neutrinos, as they would lead to LNV. The final true energy distributions of Majorana and Dirac neutrinos can therefore be different. When looking at the NC decay $N \rightarrow \nu\pi^0$, the difference in signal efficiency is almost recovered, thanks to the angular dependence of Dirac neutrino decays which makes it more distinguishable from background.

Fig. 5.3: The 90 % C.L. sensitivity regions for dominant mixings $|U_{eN}|^2$ (top), $|U_{\mu N}|^2$ (middle), and $|U_{\tau N}|^2$ (bottom) are shown. The solid lines correspond to the analysis before the background analysis, which is equivalent to a weighting factor $W_d = 1$ (see Eq. (5.3)). The dashed lines are drawn after our background analysis. The distinction between the fermionic natures are explained in the colour key.

5.4 Sensitivities of DUNE ND

We present here sensitivity regions for the discovery of heavy neutrino decays for a total amount of 1.32×10^{22} POT collected with the beam in neutrino mode. All the regions are estimated at the 90 % C.L. in rejecting the null hypothesis, by which no HNL decays are seen ($\sigma = 0$), but only background events b are expected. For a specific channel d , the probability of observing n events with a signal mean $\sigma = \mathcal{N}_d$ and background $b = \mathcal{B}_d$ (see Section 5.3.3) follows a Poisson distribution

$$P(n|\sigma, b) = (\sigma + b) \frac{e^{-(\sigma+b)}}{n!} .$$

We employ the Feldman and Cousins method [143] to estimate the number of events needed in order to reject H_0 at the desired C.L.. For example, if no background is expected ($W_d = 1$), an average of $n = 2.44$ events must be detected to reject H_0 with 90 % C.L. This criterion is used to define the sensitivity regions shown in this section, for both Majorana and Dirac neutrinos. It is found in every case that the MPD alone has a better sensitivity than the LArTPC, thanks not only to a larger volume, but also to a less dense medium which gives lower backgrounds. As the two modules are assumed to have the same detection performance, we present here a combined analysis of the two detectors, taking into account particle propagation between them. We do not consider charged identification capabilities of the ND, and therefore this information is washed out in presenting the sensitivity plots in this and next sections. Because of our charge-blind analysis, the number of events expected for Majorana neutrinos is twice as large as the number in the case of Dirac neutrinos, therefore the sensitivity to Dirac neutrino decays is a factor of two worse than the Majorana case. The limits reported here below refer to Majorana heavy neutrinos; the corresponding limit for which N is a Dirac fermion is easily retrieved by doubling the upper limit.

In Section 5.4.1, we show the constraint that DUNE ND can place on a simplified scenario in which a single mixing matrix element between HNL and active neutrinos dominates. We have also considered a scenario in which two mixings are dominant with respect to the third one, the results of which are presented in Section 5.4.2.

5.4.1 Single dominant mixing

In this section, we present the sensitivity regions for the three mixings $|U_{eN}|^2$, $|U_{\mu N}|^2$, and $|U_{\tau N}|^2$, where we assume that just one mixing element dominates over the other two. The sensitivities for the decay channels $N \rightarrow \nu e^+ e^-$, $\nu e^\pm \mu^\mp$, $\nu \mu^+ \mu^-$, $\nu \pi^0$, $e^\mp \pi^\pm$ ($|U_{eN}|^2$ only), and $\mu^\mp \pi^\pm$ ($|U_{\mu N}|^2$ only) are

Fig. 5.4: The 90 % C.L. sensitivity regions for dominant mixings $|U_{eN}|^2$ (top left), $|U_{\mu N}|^2$ (top right), and $|U_{\tau N}|^2$ (bottom) are presented for Majorana (solid lines) and Dirac (dashed lines) neutrinos. All the modes for which a background analysis was not performed are shown here. These channels become available only for masses above 500 MeV.

reported in Fig. 5.3. The solid lines corresponds to a scenario in which zero background is assumed at the ND. A background study is done for these channels (see Section 5.3.2), to outline a more realistic sensitivity; the resulting regions are shown as dashed lines in Fig. 5.3. As we expect that further improvements to background reduction can be achieved with a dedicated analysis by the experimental collaboration, the final sensitivity will lie somewhere between the lines with and without backgrounds.

For both the electronic and the muonic mixings, the two-body semi-leptonic decay modes are the ones providing the best sensitivity for sufficiently heavy masses. With the channel $N \rightarrow e^\mp \pi^\pm$, the mixing can be constrained in the range $0.15 \text{ GeV} \lesssim m_N \lesssim 0.49 \text{ GeV}$ to be $|U_{eN}|^2 < 3 \times 10^{-9}$, with a minimum point $|U_{eN}|^2 < 7 \times 10^{-11}$ at $m_N \simeq 0.39 \text{ GeV}$. Including the background rejection, the limits are loosened by a factor of ~ 3.5 . The channel $N \rightarrow \mu^\mp \pi^\pm$ can constrain the mixing $|U_{\mu N}|^2 < 5.6 \times 10^{-10}$ in the mass range $0.25 \text{ GeV} \lesssim m_N \lesssim 0.39 \text{ GeV}$, with the best limit $|U_{\mu N}|^2 < 1.3 \times 10^{-10}$ at $m_N \simeq 0.35 \text{ GeV}$. In this case, the higher background and the worse signal efficiency reduce the bound up to a factor of ~ 5.6 . The NC decay $N \rightarrow \nu \pi^0$ is the channel most affected by background and with the worst signal efficiency: the limits are higher by a factor of ~ 9.0 for the electronic, ~ 8.2 for the muonic, and ~ 11.7 for the tau mixing. Assuming no background, instead, the constraints placed by this decay mode can be competitive, as the mixings are limited at best for $m_N \simeq 0.35 \text{ GeV}$ to be $|U_{eN}|^2 < 1.1 \times 10^{-10}$ and $|U_{\mu N}|^2 < 1.6 \times 10^{-10}$, and $|U_{\tau N}|^2 < 5 \times 10^{-7}$ between $0.9 \text{ GeV} \lesssim m_N \lesssim 1.3 \text{ GeV}$. There is no sensitivity to the channel $N \rightarrow \tau^\mp \pi^\pm$ because of the subdominant branching ratio and flux content.

The three-body lepton decays have a lower reach, but are more sensitive to masses above the kaon mass limit than the two-body semi-leptonic modes. The channel $N \rightarrow \nu e^- e^+$ is the only one that covers the whole mass range of interest and is the least affected by background reduction, with a factor less than 3. It can limit the electronic mixing down to $|U_{eN}|^2 < 2.6 \times 10^{-9}$ at $m_N \simeq 0.11 \text{ GeV}$, $|U_{eN}|^2 < 3.0 \times 10^{-10}$ at $m_N \simeq 0.39 \text{ GeV}$, and $|U_{eN}|^2 < 3.0 \times 10^{-9}$ at $m_N \simeq 1.6 \text{ GeV}$. The channels $N \rightarrow \nu \mu^- \mu^+$ and $\nu e^\pm \mu^\mp$, perform better with the muon mixing, despite suffering more from background rejection, between a factor of 8 for the muon mixing and up to a factor of 15 for the tau mixing. They respectively give the limits $|U_{\mu N}|^2 < 9.2 \times 10^{-10}$ at $m_N \simeq 0.37 \text{ GeV}$ and $|U_{\mu N}|^2 < 8.7 \times 10^{-8}$ at $m_N \simeq 1.5 \text{ GeV}$, and $|U_{\mu N}|^2 < 4.8 \times 10^{-10}$ at $m_N \simeq 0.36 \text{ GeV}$ and $|U_{\mu N}|^2 < 6.4 \times 10^{-8}$ at $m_N \simeq 1.6 \text{ GeV}$. The τ sector can only be constrained by the two NC-mediated channels, which give very similar constraints near $m_N \simeq 1 \text{ GeV}$, these being both $|U_{\tau N}|^2 < 1.2 \times 10^{-6}$.

A background study was not performed for all the other decay channels, which open up for masses above the K^0 mass, due to the fact that the final state particles need a more complex analysis. The sensitivities to these modes are shown in Fig. 5.4, and they can place some constraints to the mixing. All the channels peak in their sensitivity for masses between 1.3 and 1.8 GeV. The best limits obtained

Fig. 5.5: The 90 % C.L. sensitivity regions for two dominant mixings $|U_{eN}^* U_{\mu N}|$ (top), $|U_{\mu N}^* U_{\tau N}|$ (middle), and $|U_{eN}^* U_{\tau N}|$ (bottom) are presented. All the modes considered in this work are shown here, but no background analysis is reported. As before, the solid lines correspond to the analysis with Majorana neutrinos, the dashed lines with Dirac neutrino.

for CC decays are $|U_{eN}|^2 < 2.3 \times 10^{-9}$ from $N \rightarrow e^\mp \rho^\pm$ and $|U_{\mu N}|^2 < 6.2 \times 10^{-8}$ from $N \rightarrow \mu^\mp \rho^\pm$; among the NC decays $|U_{eN}|^2 < 3.7 \times 10^{-9}$ and $|U_{\mu N}|^2 < 1.0 \times 10^{-7}$ both from $N \rightarrow \nu \phi$. Even for these channels, there is no sensitivity to CC processes to the tau mixing, but interesting limits are set from $N \rightarrow \nu \omega$, $\nu \rho^0$ to be respectively $|U_{\tau N}|^2 < 1.8 \times 10^{-6}$, 8.8×10^{-7} .

5.4.2 Two dominant mixings

In this section we present the bounds in a scenario in which two mixing elements are comparable and dominant over the third one. This case complements the previous analysis in Section 5.4.1 as, by searching for HNL decays, the experiment can constrain certain combinations of the mixing elements. This can happen when the neutrino is produced via one mixing and decays via another one, or when both mixing elements play a role in production and decay. For instance, the decay $K^+ \rightarrow \mu^+ N$ yields heavy neutrinos with a flux proportional to $|U_{\mu N}|^2$, but they can afterwards decay into the channel $\nu e^+ e^-$ also via the electronic or the tau mixing. It is important to highlight that, in the case in which one mixing is responsible for the production and a different mixing for the decay, then number of events is proportional to the product of the mixings $|U_{\alpha N}| |U_{\beta N}|$ if the studied channel is CC-mediated. However, if the decay channel is also sensitive to a NC exchange, the number of events is instead proportional to $|U_{\alpha N}| \sqrt{|U_{\alpha N}|^2 + |U_{\beta N}|^2}$. In the remainder of this section, we will use the combination of two mixings represented by $|U_{\alpha N}^* U_{\beta N}|$ for comparing bounds and sensitivity plots.

The combinations of mixing terms is relevant to charged Lepton Flavour Violating (cLFV) decays or flavour changing neutral current processes which can be enhanced in presence of nearly-sterile neutrinos. For example, the well-known decay $\mu^+ \rightarrow e^+ \gamma$ has a branching ratio which is sensitive to extra neutrino states. This reads

$$\text{Br}(\mu^+ \rightarrow e^+ \gamma) = \frac{3\alpha}{32\pi} \left| \sum_i \hat{U}_{\mu i}^* \hat{U}_{ei} G\left(\frac{m_i^2}{M_W^2}\right) \right|, \quad (5.5)$$

where $G(x)$ is the loop function of the process [144]. The current upper limit is set by the MEG experiment to be $\text{Br}(\mu^+ \rightarrow e^+ \gamma) < 4.2 \times 10^{-13}$ [145]. Despite being one of the best constrained cLFV process, the bounds on $|U_{eN}^* U_{\mu N}|$ are not as good as the ones imposed by other processes, like $\mu \rightarrow eee$ or $\mu - e$ conversion on nuclei [146]. For instance, the constraint from conversion on Au is $|U_{eN}^* U_{\mu N}| < 1.6 \times 10^{-5}$ for HNL masses larger than 100 MeV [147]. The branching ratio of other cLFV channels, like $\tau \rightarrow e\gamma$ or $\tau \rightarrow \mu\gamma$ are not as well constrained and so the bounds achievable on the combination of heavy neutrino mixings are expected to be less stringent [148, 149]. Stronger bounds come from study of three-body decays of charm and bottom mesons to charged leptons with different flavour and tau decays to pseudo-scalar mesons and a charged lepton: from the search for the decay $K \rightarrow e\mu\pi$ the bound $|U_{eN}^* U_{\mu N}| < 10^{-9}$ is reached for masses $150 \text{ MeV} \lesssim m_N \lesssim 500 \text{ MeV}$; the decays

$\tau \rightarrow e\pi\pi$ and $\tau \rightarrow \mu\pi\pi$ set the limits $|U_{eN}^* U_{\tau N}|, |U_{\mu N}^* U_{\tau N}| < 5 \times 10^{-6}$ for the respective mass ranges $0.14 \text{ GeV} \lesssim m_N \lesssim 1.7 \text{ GeV}$ and $0.24 \text{ GeV} \lesssim m_N \lesssim 1.7 \text{ GeV}$ [122].

Instead of dealing with a three-dimensional parameter scan, we simplify the study by assigning the same value to the two mixing parameters under consideration. The number of events is then reported as a function of the neutrino mass and the combination $|U_{\alpha N}^* U_{\beta N}|$. The results for all channels considered in this work are shown in Fig. 5.5. The best constraints come again from two-body semi-leptonic decays for all mixing combinations, the lowest upper limits being $|U_{eN}^* U_{\mu N}| < 6.3 \times 10^{-11}$ at $m_N \simeq 0.37 \text{ GeV}$, $|U_{\mu N}^* U_{\tau N}| < 1.1 \times 10^{-10}$ at $m_N \simeq 0.35 \text{ GeV}$, and $|U_{\tau N}^* U_{e N}| < 7.4 \times 10^{-11}$ at $m_N \simeq 0.39 \text{ GeV}$. Amongst the three-body leptonic decay channels, $N \rightarrow \nu ee$ has the best sensitivity to masses $m_N < m_{K^0}$, but actually the mode $N \rightarrow \nu e^\mp \mu^\pm$ can be more constraining at higher masses. Regarding the channels available only above the kaon mass threshold, decays to pseudo-scalar mesons are the most sensitive between C processes, whereas the decay $N \rightarrow \nu \phi$ gives the best constraint of the NC-mediated channels.

5.5 Mass model constraints from DUNE ND

From the results presented in the previous section, we find that the DUNE ND will be sensitive to very low couplings for experimentally accessible mass values. These points of the parameter space corresponds to regions viable in some realisations of low scale neutrino mass models. In view of the discussion regarding seesaw models in Section 4.1, we perform a mass matrix random scan to define such regions of the parameter space. Following the previously introduced notation, we focus on three minimal ISS scenarios which predict a HNL with a mass accessible by the experiment and that satisfy the experimental evidence of neutrino oscillation [150]. In the first two cases, the heavy neutrino under study belongs to the lightest pseudo-Dirac pair of an ISS (2,2) and an ISS (2,3) realisation; the third scenario is an ISS (2,3) case in which the fourth Weyl state becomes a Majorana neutrino in the MeV–GeV region thanks to a high LNV parameter. The details of this analysis are reported in this section, together with the overall sensitivities of DUNE ND to heavy neutrino discovery and low scale mass models. A comparison with future experiments is also included.

5.5.1 Mass model scan

We have randomly generated neutrino mass matrices and numerically diagonalised them. The structure of the mass matrix is a generalised version of an ISS:

$$\mathcal{M} = \begin{pmatrix} 0 & m_D^T & 0 \\ m_D & \mu_R & M_R^T \\ 0 & M_R & \mu_S \end{pmatrix}, \quad (5.6)$$

with two LNV submatrices, μ_R and μ_S . The number of physical parameters of a ISS (a, b) mass matrix is $n_p = 7a + b + 2ab$ [150]. We choose a basis in which m_D has complex entries but three of which are real, M_R is diagonal and real, and μ_S has a real diagonal without loss of generality. If the matrix entries respect the hierarchy $\mu_{R,S} \ll m_D \ll M_R$, the mass spectrum in the LNC limit is principally given by the diagonal values of M_R . We then perturb the matrix to achieve the three minimal ISS scenarios introduced above; the randomly generated mass matrix \mathcal{M} is then diagonalised using the Jacobi Singular Value Decomposition (SVD) as implemented in the Eigen library [?]. The Takagi decomposition,

$$\hat{U}^T \mathcal{M} \hat{U} = \text{diag}(m_1, m_2, m_3, \dots),$$

is retrieved starting from the SVD decomposition $\mathcal{M} = V \Sigma U^\dagger$, from which the singular values Σ are the non-negative square roots of the eigenvalues of $\mathcal{M}^\dagger \mathcal{M}$ and the unitary matrix is $\hat{U} = U \rho^\dagger$, where $\rho = (U^T V)^{\frac{1}{2}}$ is a unitary phase matrix.

Only matrices satisfying the current constraints on heavy neutral fermions are taken in account. The first requirement is that the eigenvalues must give the correct mass squared splittings compatible within 3σ with the measured values [?]. The condition of matching also the measured mixing angles is relaxed because the entries of the PMNS matrix, \mathcal{U} , are the result of the random structure of m_D and μ_S . Constraints on the unitarity of the mixing matrix are applied instead. The deviation from unitarity are quantified by the following Hermitian matrix:

$$\varepsilon_{\alpha\beta} \equiv |\delta_{\alpha\beta} - (\mathcal{U} \mathcal{U}^\dagger)_{\alpha\beta}| = \left| \sum_{i=4}^n \hat{U}_{\alpha i} \hat{U}_{\beta i}^* \right|. \quad (5.7)$$

The non-unitarity of the PMNS matrix has been assessed in various experiments, and the constraints depend upon the mass scale of averaged out neutrinos. For neutrino masses below the GeV scale, but heavy enough to decouple from flavour oscillations, non-unitarity effects are tested in neutrino oscillation experiment as an overall normalisation. If the neutrino mass is above the GeV scale, electroweak precision experiments provide strong constraints on non-unitarity. The constraints are summarised below (from Ref. [151–153])

$$\varepsilon_{\alpha\beta} < \begin{cases} \begin{pmatrix} 2.4 \times 10^{-2} & 1.3 \times 10^{-2} & 3.5 \times 10^{-2} \\ . & 2.2 \times 10^{-2} & 6.0 \times 10^{-3} \\ . & . & 1.0 \times 10^{-1} \end{pmatrix} & \text{if } 10 \text{ eV} \lesssim m_N \lesssim 1 \text{ GeV ,} \\ \begin{pmatrix} 1.3 \times 10^{-3} & 1.2 \times 10^{-5} & 1.4 \times 10^{-3} \\ . & 2.2 \times 10^{-4} & 6.0 \times 10^{-4} \\ . & . & 2.8 \times 10^{-3} \end{pmatrix} & \text{if } m_N \gtrsim 1 \text{ GeV .} \end{cases}$$

The μ_R and μ_S entries of the ISS matrices naturally lead to lepton flavour and lepton number

violating processes. The most constrained process is the decay rate of $\mu^+ \rightarrow e^+\gamma$, the branching ratio of which is given in Eq. (5.5). The current upper limit on the branching ratio is 4.2×10^{-13} , but a future upgrade of the experiment foresees to reach a limit lower than 5×10^{-14} .

Heavy neutrinos in a ISS model also contribute to the neutrinoless double beta decay. The effective neutrino mass $m_{\beta\beta}$ receives further corrections with respect to the standard expression as

$$m_{\beta\beta} \simeq \left| \sum_i \hat{U}_{ei}^2 \frac{p^2 m_i}{p^2 - m_i^2} \right| \quad (5.8)$$

where $p^2 \simeq -0.015 \text{ GeV}^2$ is the typical virtual momentum of the exchanged neutrino. The contribution from masses above the 100 MeV scale drops as $1/m_i^2$ while it is constant for masses below [154]. It is interesting to note that the contributions given by pseudo-Dirac pairs are subject to partial cancellation, regulated by the LNV parameters. In the LNC limit, the cancellation is maximum and the paired states do not take part in the $0\nu\beta\beta$ process. The latest result from the KamLAND-Zen experiment [155] is interpreted as $m_{\beta\beta} < 61 \text{ meV}$.

We find, for the first two ISS scenarios, that the allowed ranges span in the space $m_D \sim 10^{[3,6]} \text{ eV}$, $M_R \sim 10^{[6,15]} \text{ eV}$, μ_S and $\mu_R \sim 10^{[-4,1]} \text{ eV}$. We check that each matrix generated respects the *naturalness condition* in the 't Hooft sense [112] and that the mass spectrum presents a mass state accessible by the DUNE experiment. For the third ISS case, large entries of the sub-matrix μ_S are necessary to give the Majorana state a mass that can be probed by the experiment. We find the ranges of $m_D \sim 10^{[3,10]} \text{ eV}$, $M_R \sim 10^{[7,15]} \text{ eV}$, $\mu_S \sim 10^{[4,9]} \text{ eV}$ to respect the constraints. The hierarchy and naturalness conditions are relaxed in this case. It is found that the block μ_R does not influence the final mass spectrum; it usually gives contribution to the light neutrino masses at the loop level, in a region below the GeV scale that has been already excluded by experiments. The resulting points in the space $(m_N, |U_{\alpha N}|^2)$ are clustered together and the regions defined are overlaid in Fig. 5.6. Any combination of mass and mixing element inside these areas can be justified by a valid neutrino mass matrix which can explain the light neutrino masses and survive the experimental constraints. The pseudo-Dirac pairs from the ISS (2,2) and ISS (2,3) scenarios give very similar regions, but Majorana states from the ISS (2,3) realisation can only be generated with very small couplings. A type I seesaw band, corresponding to light neutrino mass between 20 meV and 200 meV, is plotted as well for comparison.

5.5.2 Overall sensitivity

We define the overall sensitivity of DUNE ND to the discovery of HNL as the combination of the sensitivities to selected channels, presented in Section 5.4. These channels are $N \rightarrow \nu ee$, $\nu e\mu$, $\nu \mu\mu$, $\nu \pi^0$, $e\pi$, $\mu\pi$ and are preferred because of their good discovery prospect, for which backgrounds have also been studied. They all give strong sensitivities, especially for masses below 500 MeV. Their reach is due to high branching ratios and also to clean and well-defined signatures in the detector, allowing

Fig. 5.6: The 90 % C.L. sensitivity regions for dominant mixings $|U_{eN}|^2$ (top left), $|U_{\mu N}|^2$ (top right), and $|U_{\tau N}|^2$ (bottom) are presented combining results for channels with good detection prospects. The study is performed for Majorana neutrinos (solid) and Dirac neutrinos (dashed), assuming no background. The region excluded by experimental constraints (brown) is obtained by combining the results from PS191 [81, 82], peak searches [76–80], CHARM [85], NuTeV [86], DELPHI [83], and T2K [98]. The sensitivity for DUNE ND (black) is compared to the predictions of future experiments, SBN [99] (blue), SHiP [139] (red), NA62 [132] (green), and FASER [136] with 1 m radius. The shaded areas corresponds to possible neutrino mass models considered in this article: the simulations of the ISS (2,2) and ISS (2,3) models where the lightest pseudo-Dirac pair is the neutrino decaying in the ND (cyan); the ISS (2,3) scenario when the single Majorana state is responsible for a signal (magenta); the type I seesaw scenario with a neutrino mass starting from 20 meV to 0.2 eV (yellow).

the background to be controlled with sufficient precision. The neutrino spectrum component coming from the D_s meson allows for weaker sensitivity to masses above the neutral kaon mass. We conducted the sensitivity study for both scenarios, in which either a Majorana or a Dirac neutrino is the decaying particle.

To appreciate the ND performance, we make a comparison with results of previous experiments, in particular PS191 [81, 82], peak searches [76–78], CHARM [85], NuTeV [86], DELPHI [83], and T2K [98]. We find that the DUNE ND can increase the bound on the electronic and muonic mixing elements for masses $m_N < m_{K^0}$ with respect to previous experiments. The constraint on the tauonic mixing is at least comparable with previous results. For masses above, for which neutrino production relies on charm meson decays, the existing bounds are improved for the electronic mixing and the tauonic mixing, while a conservative result can be achieved in the muonic case. We also overlay the prospects for the SBN programme [99], NA62 [132], and the proposed SHiP [139] and FASER [136] with 1 m radius. DUNE ND will give the best sensitivity for masses below the 500 MeV in all channels, but the tauonic one. However, anywhere the D_s meson production is involved, the experiment cannot outperform the predicted sensitivity of the SHiP experiment which will deploy a 400 GeV proton beam on a titanium-zinc-molybdenum alloy target, enhancing the production of charm and bottom mesons. NA62 gives better results for the $|U_{\mu N}|^2$ mixing, but DUNE has a better sensitivity to the electron and tau channels. FASER is comparable to NA62 in sensitivity, but it can reach regions of the parameter space beyond the 2 GeV limit to which DUNE is not sensitive.

We then compare the overall sensitivity to regions allowed by neutrino mass models. In the electronic and muonic channels, DUNE ND will be sensitive to a large part of the pseudo-Dirac regions, corresponding to ISS (2,2) and ISS (2,3) models, part of which have been already excluded by past experiments. DUNE will close the gap and put to test type I seesaw parameters, especially for HNL masses between 200 and 500 MeV, starting to reach the region of ISS (2,3) with large lepton number violation. For the tauonic channel, the experiment will probe only a small portion of pseudo-Dirac pairs from ISS (2,2) and ISS (2,3) models. The sensitivity is not high enough to reach type I and Majorana state regions, which not even the dedicated experiment SHiP can.

The ISS (2,3) scenario in which the pseudo-Dirac pair is accessible by the experiment also predicts a light Majorana state, the mass of which is controlled by the small LNV perturbations. This entails

Fig. 5.7: One of the two ISS(2,3) realisations considered presents a Majorana state at masses comparable with SBL experiments. We show the results of the ISS(2,3) simulation (blue dots) for Δm_{41}^2 against combination of mixing angles and the experimental result at 90 % C.L.: $|U_{e4}|^2$ (left) compared to Super-Kamiokande and IceCube combined [156] and DANSS [56], $\sin^2 2\theta_{\mu e} = 4|U_{eN4}|^2|U_{\mu 4}|^2$ (middle) compared to KARMEN2, OPERA and MiniBooNE [44], and $|U_{\mu 4}|^2$ (right) compared to a combined ν_μ disappearance analysis [156]. Only the points generated by matrices which pass the experimental constraints are shown here.

the presence of a third mass splitting Δm_{41}^2 , which could give an active-sterile oscillation signature in short baseline experiments. In figure Fig. 5.7, the new mass splitting is plotted against the mixings $|U_{e4}|^2$, $|U_{\mu 4}|^2$ and the combination usually referred to as $\sin^2 2\theta_{\mu e} \equiv 4|U_{e4}|^2|U_{\mu 4}|^2$. The mass splittings generated in the matrix scan span from $\Delta m_{31}^2 \simeq 0.0025 \text{ eV}^2$ up to 10^4 eV^2 , and the squared mixings cover a large region, down to 10^{-14} for all the flavours. The reactor anomalies could be soon excluded at the 90 % C.L. by the DANSS experiment [56] and the allowed regions from LSND [41] and MiniBooNE [42–44] require values of $\sin^2 2\theta_{\mu e} \gtrsim 10^{-3}$. Given the results of the matrix scan, it is unlikely that one of the ISS(2,3) realisations considered in this work could link an heavy neutrino-like signal in DUNE ND and explain a short baseline anomaly at the same time, unless for sparse and very fine-tuned points.

5.6 Background reduction

We performed a background analysis only for the decay channels with an important discovery potential, and these are $N \rightarrow \nu e^+ e^-$, $\nu e^\pm \mu^\mp$, $\nu \mu^+ \mu^-$, $\nu \pi^0$, $e^\mp \pi^\pm$, and $\mu^\mp \pi^\pm$. The advantage of these channels is that they give the best sensitivities to new physics, thanks to both their high branching ratios and the flux intensity in the region of interest. Moreover, the final state particle are all well-studied particles, most of which leave clean tracks in the detector. As an example of the background reduction using kinematic cuts, we present here the background analysis for a sterile neutrino with mass $m_N = 300 \text{ MeV}$.

With respect to the following tables, the values presented are in the form “ $\mathcal{X} \rightarrow \mathcal{Y}$ ”, where \mathcal{X} is the per mille (10^{-3}) fraction of background events from mis-identification and \mathcal{Y} is the per mille fraction of irreducible background after the application of data cuts based on kinematic properties. When the value 0×10^{-3} is shown, we mean that less than one background event per million is expected. The average was computed by weighting the flux components contribution to the background, using the respective interaction rate as weights, reported in Tab. 5.2. We assume that the ν_τ and $\bar{\nu}_\tau$ components are not responsible for background events, therefore only the ν_e , ν_μ , and $\bar{\nu}_\mu$ components are studied. The last two rows of the tables are the percentage of signal events retained, after the kinematic cuts are applied to the MC simulation of Majorana and Dirac neutrinos. Because of the overwhelming background, the number of signal events are most of the time substantially influenced.

We group the studied channels in three categories, which have similar kinematic features: two-body decay, which are semi-leptonic, three-body decay channels, which are purely leptonic instead, and decays which can be only detected via photon reconstruction.

5.6.1 Two-body decays

The two-body decays $N \rightarrow e^\pm\pi^\mp$ and $N \rightarrow \mu^\pm\pi^\mp$ are the most promising channels for the detection of a heavy neutrino, being the decay mode with the highest branching ratios. The typical signal is a two charged particle tracks with a common vertex, in a V^0 -like fashion. Muons and pions leave a clean signature in the fine grained tracker and the LArTPC, and electrons are easily reconstructed. They give direct information on the parent particle, being the invariant mass of the process the same as the mass of the decaying neutrino, $m_N^2 = s = m_\ell^2 + m_\pi^2 + 2E_\ell E_\pi - 2|\mathbf{p}_\ell||\mathbf{p}_\pi| \cos\theta$, where θ is the opening angle between the lepton and the pion. Moreover, the two particles are emitted back-to-back in the neutrino reference frame, and, once the system is boosted in the direction of the decaying neutrino, the relative position on the perpendicular plane is preserved. The CC interactions of ν_e and ν_μ are the main background processes, because additional photons or pions can be mis-identified for electrons or muons. We therefore cut on the separation angle between the charged particles, which are very boosted forward, and we request that they are in opposite direction on the plane perpendicular to the beamline. An energy threshold on the reconstructed neutrino, above 5 GeV, is also imposed, as the background events peak at lower energies. The background events are reduced up to a factor $\mathcal{O}(10^4)$, whereas $\sim 46\%$ of the Majorana neutrino events and $\sim 40\%$ of the Dirac neutrino events lie above the cuts.

	$N \rightarrow e^- \pi^+$	$N \rightarrow \mu^- \pi^+$
ν_e	$58.2 \rightarrow 11 \times 10^{-3}$	$0.44 \rightarrow 0 \times 10^{-3}$
ν_μ	$0.11 \rightarrow 0 \times 10^{-3}$	$76.0 \rightarrow 4 \times 10^{-3}$
$\bar{\nu}_\mu$	$0.14 \rightarrow 0 \times 10^{-3}$	$72.9 \rightarrow 10 \times 10^{-3}$
Average	$0.78 \rightarrow 0 \times 10^{-3}$	$74.9 \rightarrow 5 \times 10^{-3}$
Majorana	46.14 %	46.08 %
Dirac	40.48 %	40.00 %

5.6.2 Three-body decays

The three-body decays studied are $N \rightarrow \nu e^- e^+$, $N \rightarrow \nu e^\mp \mu^\pm$, and $N \rightarrow \nu \mu^- \mu^+$. The principle sources of background are mis-reconstructed photons, which promptly converts to electron-positron pairs, or pion tracks that are too long and identified as muons. Despite this, the mis-ID rate is already low as two leptons are needed to identify these channels. However, the background analysis in the case of three-body decays is further complicated by the loss of the light neutrino and so direct information on the parent particle may not be recovered; there is some missing transverse momentum, even though small because of the neutrino lightness. Cuts on the distribution of the transverse momenta of electrons and muons can therefore help reject background events, which deviate from the beam line direction. We find, nonetheless, that cuts on the invariant mass of the charged lepton system are useful to discriminate signal from background. The energy range considered for the lepton-pairs is different for the channels $\nu e^- e^+$ ($E_{ee} > 2$ GeV), $\nu e^\mp \mu^\pm$ ($E_{e\mu} > 4$ GeV), and $\nu \mu^- \mu^+$ ($E_{\mu\mu} > 5$ GeV), due to different distributions

of the background energy spectra in the three cases. The cuts applied to the two-electron channel are the ones with the highest signal selection efficiency, yet reducing the background by a factor ~ 200 . On the contrary, the two-muon channel has the highest mis-identification rate, and so the worst selection success for three-body decays. The electron–muon channel lies in between the other two, presenting though the lowest mis-ID rate. The slightly different behaviours between the kinematics of Majorana and Dirac neutrinos is emphasised by the selection efficiencies of the $\nu e^- e^+$ channel. This tendency is lost as the signal efficiency decreases in the other two channels.

	$N \rightarrow \nu e^+ e^-$	$N \rightarrow \nu e^\pm \mu^\mp$	$N \rightarrow \nu \mu^+ \mu^-$
ν_e	$0.66 \rightarrow 3 \times 10^{-3}$	$4.48 \rightarrow 60 \times 10^{-3}$	$0.11 \rightarrow 0 \times 10^{-3}$
ν_μ	$0.71 \rightarrow 3 \times 10^{-3}$	$0.19 \rightarrow 0 \times 10^{-3}$	$5.42 \rightarrow 7 \times 10^{-3}$
$\bar{\nu}_\mu$	$0.73 \rightarrow 7 \times 10^{-3}$	$0.52 \rightarrow 7 \times 10^{-3}$	$4.72 \rightarrow 9 \times 10^{-3}$
Average	$0.71 \rightarrow 4 \times 10^{-3}$	$0.26 \rightarrow 2 \times 10^{-3}$	$5.31 \rightarrow 9 \times 10^{-3}$
Majorana	68.67 %	44.41 %	36.63 %
Dirac	59.43 %	40.50 %	33.77 %

5.6.3 EM-detected decays

The semi-leptonic decay $N \rightarrow \nu \pi^0$ may only be identified by a correct photon reconstruction, since the neutral pion decays almost 100 % of the time in two photons. This particle is extensively produced in CC and NC neutrino-nucleon interactions, while individual photon background is due to badly reconstructed EM showers, occurring especially in ν_e -CC interactions. If a pair of γ is detected and their invariant mass is compatible with m_{π^0} , the parent pion is reconstructed. Afterwards, we compare the transverse momenta of the single photons with the transverse momentum of their parent particle, and we set constraints on the separation angle between the two γ . We consider only photons with an energy greater than 1 GeV, to avoid the dominant low-energy background. The selection cuts results to be more severe for this mode, leaving signal events just below 20 %, but obtaining a reasonable background reduction of a factor of 500. This detection channel is the most challenging, among those studied, because of the multiple background sources. However, it is one of the decay modes with the highest branching ratio, and with advanced and dedicated techniques [157, 158] the reconstruction efficiency can be improved, as well as the background rejection.

$N \rightarrow \nu\pi^0$	
ν_e	$21.0 \rightarrow 58 \times 10^{-3}$
ν_μ	$24.3 \rightarrow 39 \times 10^{-3}$
$\bar{\nu}_\mu$	$26.6 \rightarrow 99 \times 10^{-3}$
Average	$24.4 \rightarrow 43 \times 10^{-3}$
Majorana	18.33 %
Dirac	17.81 %

Chapter 6

Conclusions

And that's all folks.

Appendix A

List of integrals and identities

In presenting the differential and total decay rates in Section 4.2 and 4.3, we have used a series of simplifying integrals and functions of the particle masses. We report them jointly here. The letters x , y , and z denote squared ratios of masses, while s , t , and u are the corresponding Mandelstam variables for three body decays.

A.0.1 Decay widths

In [69], the following functions are used to express the total rates of two-body decays

$$I_1(x, y) = \lambda^{\frac{1}{2}}(1, x, y) [(1 - x)^2 - y(1 + x)] ,$$

$$I_2(x, y) = \lambda^{\frac{1}{2}}(1, x, y) [(1 + x - y)(1 + x + 2y) - 4x] ,$$

and the rate of three-body decays can be expressed in terms of two more functions [69],

$$I_1(x, y, z) = 12 \int_{\frac{(\sqrt{x}+\sqrt{y})^2}{(\sqrt{x}-\sqrt{z})^2}}^{\frac{(1-\sqrt{z})^2}{(\sqrt{x}+\sqrt{y})^2}} \frac{ds}{s} (s - x - y) (1 + z - s) \lambda^{\frac{1}{2}}(1, x, y) \lambda^{\frac{1}{2}}(1, s, z) ,$$

$$I_2(x, y, z) = 24 \sqrt{yz} \int_{\frac{(\sqrt{y}+\sqrt{z})^2}{(\sqrt{y}-\sqrt{x})^2}}^{\frac{(1-\sqrt{x})^2}{(\sqrt{y}+\sqrt{z})^2}} \frac{ds}{s} (1 + x - s) \lambda^{\frac{1}{2}}(s, y, z) \lambda^{\frac{1}{2}}(1, s, x) .$$

In this work we have introduced two differential generalisations of the two-body formulae,

$$I_1^\pm(x, y; \theta) = \frac{1}{4\pi} \lambda^{\frac{1}{2}}(1, x, y) \left[(1 - x)^2 - y(1 + x) \pm (x - 1) \lambda^{\frac{1}{2}}(1, x, y) \cos \theta \right] ,$$

$$I_2^\pm(x, y; \theta) = \frac{1}{4\pi} \lambda^{\frac{1}{2}}(1, x, y) \left[(1 + x - y)(1 + x + 2y) - 4x \pm (x + 2y - 1) \lambda^{\frac{1}{2}}(1, x, y) \cos \theta \right] .$$

Our expressions satisfy the normalisation conditions,

$$\int_0^{2\pi} d\varphi \int_{-1}^1 d\cos\theta I_1^\pm(x, y; \theta) = I_1(x, y) ,$$

$$\int_0^{2\pi} d\varphi \int_{-1}^1 d\cos\theta I_2^\pm(x, y; \theta) = I_2(x, y) .$$

We also note the following integrals which are necessary in deriving the total decay rate for the three-body leptonic modes,

$$\int ds_1 \int ds_2 (s_2 - \xi_3^2)(1 + \xi_4^2 - s_2) = \frac{I_1(0, \xi_3^2, \xi_4^2)}{12} , \quad (\text{A.1})$$

$$\int ds_1 \int ds_2 (s_1 - \xi_4^2)(1 + \xi_3^2 - s_1) = \frac{I_1(0, \xi_4^2, \xi_3^2)}{12} , \quad (\text{A.2})$$

$$\int ds_1 \int ds_2 2\xi_3 \xi_4 (s_1 + s_2 - \xi_3^2 - \xi_4^2) = \frac{I_2(0, \xi_3^2, \xi_4^2)}{12} , \quad (\text{A.3})$$

where ξ_i have the same meanings of Eqs. (4.17) and (4.18).

A.0.2 Scaling factors for three body-decays

Three-body lepton decays can produce neutrinos in two ways, depending on whether the neutrino mixes with the initial or with the final flavour. The expressions presented in Section 4.3 make use of the following integrals:

$$I_\ell^\pm(x, y, z) = 12 \int_{(\sqrt{x}+\sqrt{y})^2}^{(1-\sqrt{z})^2} \frac{ds}{s} (1 + z - s) [s - x - y \mp \lambda^{\frac{1}{2}}(s, x, y)] \times \lambda^{\frac{1}{2}}(s, x, y) \lambda^{\frac{1}{2}}(1, s, z) ,$$

$$I_{\bar{\ell}}^\pm(x, y, z) = 12 \int_{(\sqrt{x}+\sqrt{y})^2}^{(1-\sqrt{z})^2} \frac{ds}{s} [1 + z - s \mp \lambda^{\frac{1}{2}}(1, s, z)] (s - x - y) \times \lambda^{\frac{1}{2}}(s, y, z) \lambda^{\frac{1}{2}}(1, s, z) .$$

When averaging over the helicity states, these two functions become identical and, because of symmetry crossing, also identical to the integral $I_1(x, y, z)$, expressed above.

In Section 4.3, the three-body decay rate of pseudoscalar meson requires the following integral:

$$I_h^\pm(x, y, z) = \int_{\frac{(\sqrt{x}+\sqrt{y})^2}{(\sqrt{x}-\sqrt{y})^2}}^{(1-\sqrt{z})^2} ds \int_{t_-}^{t_+} dt [F^2 A^\pm(s, t) + G^2 B^\pm(s, t) - \text{Re}(F^* G) C^\pm(s, t)] ,$$

with $t_\pm = x + z + \frac{(1-s-z)(s-y+x) \pm \lambda^{\frac{1}{2}}(s, y, z) \lambda^{\frac{1}{2}}(1, s, z)}{2s}$,

where F and G are convenient combinations of hadronic form factors $f^{(h, h')}$. From lattice QCD considerations, form factors should carry the correct Clebsch-Gordan, but here we drop them as they are irrelevant when studying scale factors. The combinations F and G are

$$F = 2 f_+^{(h, h')}(u) = f_+^{(h, h')}(0) \left(1 + \lambda_+^{(h, h')} \frac{u}{x} \right) ,$$

$$G = f_+^{(h, h')}(u) - f_-^{(h, h')}(u) = f_+^{(h, h')}(0) \left[1 + \lambda_+^{(h, h')} \frac{u}{x} - (\lambda_+^{(h, h')} - \lambda_0^{(h, h')}) \left(1 + \frac{1}{x} \right) \right] ,$$

with λ parametrising the linear dependence [?] of the form factors with respect the momentum transfer between the two mesons, u , directly connected to the other Mandelstam variables, s and t :

$$u = 1 + x + y + z - s - t .$$

The values of $\lambda_{+,0}$ is determined experimentally [?]. The functions A , B , and C are

$$A^\pm(s, t) = \frac{1}{2}(1+y-t) \left[1 + z - s \mp \lambda^{\frac{1}{2}}(1, z, s) \right] - \frac{1}{2} \left[u - y - z \mp \lambda^{\frac{1}{2}}(u, y, z) \right] ,$$

$$B^\pm(s, t) = \frac{1}{2}(y+z)(u-y-z) + 2yz \mp (y-z) \frac{\lambda^{\frac{1}{2}}(u, y, z)}{2} ,$$

$$C^\pm(s, t) = z(1+y-t) + \left[y \pm \frac{\lambda^{\frac{1}{2}}(u, y, z)}{2} \right] (1+z-s) .$$

When summing over helicity states, the kinematic simplifies to

$$A(s, t) = (1+y-t)(1+z-s) - (u-y-z) ,$$

$$B(s, t) = (y+z)(u-y-z) + 4yz ,$$

$$C(s, t) = 2z(1+y-t) + 2y(1+z-s) .$$

A.1 Polarised $N \rightarrow \nu \ell_\alpha^- \ell_\beta^+$ distributions

A.1.1 Dirac ν_i

The coefficients for a Dirac neutrino decay are given by

$$\begin{aligned} C_1^\nu &= C_4^\nu = \sum_{\gamma=e}^\tau |U_{\gamma i}|^2 [\delta_{\alpha\beta} g_L^2 + \delta_{\gamma\alpha} (1 + \delta_{\alpha\beta} g_L)] , \\ C_2^\nu &= C_5^\nu = \delta_{\alpha\beta} g_R^2 \sum_{\gamma=e}^\tau |U_{\gamma i}|^2 , \\ C_3^\nu &= C_6^\nu = \delta_{\alpha\beta} g_R \sum_{\gamma=e}^\tau |U_{\gamma i}|^2 (\delta_{\gamma\beta} + g_L) , \end{aligned}$$

where the chiral couplings for charged leptons are given by $g_L = -\frac{1}{2} + \sin^2 \theta_W$ and $g_R = \sin^2 \theta_W$.

A.1.2 Dirac $\bar{\nu}_i$

The coefficients for the Dirac antineutrino decay—which involve some vital minus signs compared to the neutrino case—are given by

$$\begin{aligned} C_1^{\bar{\nu}} &= -C_4^{\bar{\nu}} = \delta_{\alpha\beta} g_R^2 \sum_{\gamma=e}^\tau |U_{\gamma i}|^2 , \\ C_2^{\bar{\nu}} &= -C_5^{\bar{\nu}} = \sum_{\gamma=e}^\tau |U_{\gamma i}|^2 [\delta_{\alpha\beta} g_L^2 + \delta_{\gamma\beta} (1 + \delta_{\alpha\beta} g_L)] , \\ C_3^{\bar{\nu}} &= -C_6^{\bar{\nu}} = \delta_{\alpha\beta} g_R \sum_{\gamma=e}^\tau |U_{\gamma i}|^2 (\delta_{\alpha\gamma} + g_L) , \end{aligned}$$

where the chiral couplings g_L and g_R have the same meaning.

A.1.3 Majorana N_i

The amplitude for Majorana decay is the sum of the Dirac neutrino and Dirac antineutrino amplitudes given above:¹

$$|A_\pm|^2 = |A_\pm^\nu|^2 + |A_\pm^{\bar{\nu}}|^2 .$$

Crucially, this means that the coefficients in the isotropic terms are the sum of those for a neutrino and antineutrino while the coefficients in the angular terms are the difference, leading to cancellations. All in all, we find

$$|A_\pm|^2 = |A_0|^2 \pm |A_1|^2 ,$$

¹In general, there are interference terms between “neutrino” and “antineutrino” diagrams; however all such contributions are suppressed by the mass scale of the outgoing light neutrino, which is taken to be zero in these calculations.

with the coefficients

$$\begin{aligned}
C_1 &= C_1^\nu + C_1^{\bar{\nu}} = \sum_{\gamma=e}^{\tau} |U_{\gamma i}|^2 [(g_L^2 + g_R^2)\delta_{\alpha\beta} + \delta_{\gamma\alpha}(1 + \delta_{\alpha\beta}g_L)] , \\
C_2 &= C_2^\nu + C_2^{\bar{\nu}} = \sum_{\gamma=e}^{\tau} |U_{\gamma i}|^2 [(g_L^2 + g_R^2)\delta_{\alpha\beta} + \delta_{\gamma\beta}(1 + \delta_{\alpha\beta}g_L)] , \\
C_3 &= C_3^\nu + C_3^{\bar{\nu}} = 2\delta_{\alpha\beta}g_R \sum_{\gamma=e}^{\tau} |U_{\gamma i}|^2 (\delta_{\alpha\gamma} + g_L) , \\
C_4 &= C_1^\nu - C_1^{\bar{\nu}} = \sum_{\gamma=e}^{\tau} |U_{\gamma i}|^2 [\delta_{\alpha\beta}(g_L^2 - g_R^2) + \delta_{\gamma\alpha}(1 + \delta_{\alpha\beta}g_L)] , \\
C_5 &= C_2^\nu - C_2^{\bar{\nu}} = - \sum_{\gamma=e}^{\tau} |U_{\gamma i}|^2 [\delta_{\alpha\beta}(g_L^2 - g_R^2) + \delta_{\gamma\beta}(1 + \delta_{\alpha\beta}g_L)] , \\
C_6 &= C_3^\nu - C_3^{\bar{\nu}} = 0 .
\end{aligned}$$

Note that for the three-body decays, the decay is not isotropic in the Majorana limit; however, the quantity $g_L^2 - g_R^2 \approx 0.02$, suppresses the angular terms in the pure NC case.

Appendix B

Open charm production

Following the same procedure as the one described in Ref. [139], we estimate the number of strange D mesons to be

$$\mathcal{N}_{D_s} = \frac{\sigma_{c\bar{c}}}{\sigma_{pA}} f_{D_s} = (2.8 \pm 0.2) \times 10^{-6} , \quad (\text{B.1})$$

where $\sigma_{c\bar{c}} = 12 \pm 1 \mu\text{b}$ is the proton-target open charm cross section, $\sigma_{pA} = 331.4 \pm 3.4 \text{ mb}$ is the total inelastic proton-target on carbon ($A = {}^{12}\text{C}$) [159] cross section, and $f_{D_s} = 7.7\%$ is the D_s fragmentation fraction [160]. We calculate the open charm production cross section at the leading order in perturbation theory, with a graphite fixed target and a 80 GeV proton p . The correct process to consider is the proton–nucleon interaction, therefore

$$\sigma_{c\bar{c}} \equiv \sigma(pA \rightarrow c\bar{c} + X) \approx A \sigma(pN \rightarrow c\bar{c} + X) ,$$

using the correct Parton Distribution Function (PDF) for a bound nucleon N in the nucleus A . There are four diagrams, shown in figure Fig. B.1, that contributes to the cross section, but three of them interfere with each other. These cross sections are well-known SM calculations and can be found in Ref. [?]. The integrated cross section is:

$$\begin{aligned} \sigma(pN \rightarrow c\bar{c} + X) = & \int_{\tau_0}^1 dx_1 \int_{\frac{\tau_0}{x_1}}^1 dx_2 \int d\Omega \left[\left(f_{g/p}^1 f_{g/A}^2 + f_{g/p}^2 f_{g/A}^1 \right) \frac{d\sigma_{gg \rightarrow c\bar{c}}}{d\Omega} \right. \\ & \left. + \sum_{q=u,d,s} \left(f_{q/p}^1 f_{\bar{q}/A}^2 + f_{q/p}^2 f_{\bar{q}/A}^1 + f_{\bar{q}/p}^1 f_{q/A}^2 + f_{\bar{q}/p}^2 f_{q/A}^1 \right) \frac{d\sigma_{q\bar{q} \rightarrow c\bar{c}}}{d\Omega} \right], \quad (\text{B.2}) \end{aligned}$$

Fig. B.1: These are the four diagrams contributing to the hard process in open charm production. The diagrams with gluons in the initial state interfere with each other giving rise to cross terms in the colour structure.

with $\tau_0 = \hat{s}_0/s$ and \hat{s}_0 being the threshold energy at the partonic level and $s = 2m_p(m_p + E_p)$ is the centre of mass energy, given that $m_p \simeq m_n$. The partonic structure of the nucleus is described by the functions $f_{\rho/\eta}^i = f_{\rho/\eta}(x_i, M_F)$, which are interpreted as the probability of finding a parton ρ in the particle η carrying a x_i fraction of the momentum of η , at the energy scale M_F . The two momentum fractions are related by $x_1 x_2 s = \hat{s}$, where the hat symbol denotes the energy of the parton-level process.

We adopt a factorisation scale of $M_F = 2.1 m_c$ for the computation of $\sigma_{c\bar{c}}$, while the renormalisation scale of α_s is set to $\mu_R = 1.6 m_c$, and the charm mass has the value $m_c = (1.28 \pm 0.03) \text{ GeV}$. The integration is regulated for $|\cos \theta| < 0.8$, with θ the angle in the centre of mass frame. The theoretical curve in Fig. 7.4(a) of Ref. [139] was used to check our evaluation, and it was successfully reproduced up to NLO corrections. For the calculation we employed LHAPDF [161] and the nCTEQ15 PDF set [162], resulting in $\sigma_{pA \rightarrow c\bar{c}} = (12 \pm 1) \mu\text{b}$, for an 80 GeV protons on a graphite target.

Bibliography

- [1] B. Aharmim *et al.* [SNO Collaboration], [Phys. Rev. C **72** \(2005\) 055502](#), [[nucl-ex/0502021](#)].
- [2] Y. Fukuda *et al.* [Super-Kamiokande Collaboration], [Phys. Rev. Lett. **81** \(1998\) 1562](#), [[hep-ex/9807003](#)].
- [3] V. Zerkin and B. Pritychenko, [Nuclear Instruments and Methods in Physics Research Section A: Accelerators, Spectrometers, Detectors and Associated Equipment **888** \(2018\) 31](#).
- [4] A. B. Smith, P. R. Fields, and A. M. Friedman, [Phys. Rev. **104** \(1956\) 699](#).
- [5] A. B. Smith, P. R. Fields, and J. H. Roberts, [Phys. Rev. **108** \(1957\) 411](#).
- [6] A. D. Sakharov, [Pisma Zh. Eksp. Teor. Fiz. **5** \(1967\) 32](#).
- [7] M. Fukugita and T. Yanagida, [Phys. Lett. B **174** \(1986\) 45](#).
- [8] J. H. Christenson *et al.*, [Phys. Rev. Lett. **13** \(1964\) 138](#).
- [9] B. Aubert *et al.* [BaBar Collaboration], [Phys. Rev. Lett. **86** \(2001\) 2515](#), [[hep-ex/0102030](#)].
- [10] K. Abe *et al.* [Belle Collaboration], [Phys. Rev. Lett. **87** \(2001\) 091802](#), [[hep-ex/0107061](#)].
- [11] R. Aaij *et al.* [LHCb Collaboration], [Phys. Rev. Lett. **110** \(2013\) no.22, 221601](#), [[arXiv:1304.6173 \[hep-ex\]](#)].
- [12] R. Aaij *et al.* [LHCb Collaboration], [Phys. Rev. Lett. **122** \(2019\) no.21, 211803](#), [[arXiv:1903.08726 \[hep-ex\]](#)].
- [13] C. Jarlskog, [Phys. Rev. Lett. **55** \(1985\) 1039](#).
- [14] K. Abe *et al.* [Hyper-Kamiokande Collaboration], [[arXiv:1805.04163 \[physics.ins-det\]](#)].
- [15] S. Pascoli, S. T. Petcov, and A. Riotto, [Nucl. Phys. B **774** \(2007\) 1](#), [[hep-ph/0611338](#)].
- [16] K. Abe *et al.* [T2K Collaboration], [Phys. Rev. Lett. **107** \(2011\) 041801](#), [[arXiv:1106.2822 \[hep-ex\]](#)].
- [17] Y. Abe *et al.* [Double Chooz Collaboration], [Phys. Rev. Lett. **108** \(2012\) 131801](#), [[arXiv:1112.6353 \[hep-ex\]](#)].

- [18] F. P. An *et al.* [Daya Bay Collaboration], *Phys. Rev. Lett.* **108** (2012) 171803, arXiv:1203.1669 [hep-ex].
- [19] J. K. Ahn *et al.* [RENO Collaboration], *Phys. Rev. Lett.* **108** (2012) 191802, arXiv:1204.0626 [hep-ex].
- [20] M. Jiang *et al.* [Super-Kamiokande Collaboration], *PTEP* **2019** (2019) no.5, 053F01, arXiv:1901.03230 [hep-ex].
- [21] K. Abe *et al.* [Super-Kamiokande Collaboration], *Phys. Rev. D* **97** (2018) no.7, 072001, arXiv:1710.09126 [hep-ex].
- [22] K. Abe *et al.* [T2K Collaboration], *Phys. Rev. Lett.* **121** (2018) no.17, 171802, arXiv:1807.07891 [hep-ex].
- [23] K. Abe *et al.* [T2K Collaboration], *Phys. Rev. D* **96** (2017) no.9, 092006 (Erratum: *Phys. Rev.D98,no.1,019902(2018)*), arXiv:1707.01048 [hep-ex].
- [24] G. Bak *et al.* [RENO Collaboration], *Phys. Rev. Lett.* **121** (2018) no.20, 201801, arXiv:1806.00248 [hep-ex].
- [25] D. Adey *et al.* [Daya Bay Collaboration], *Phys. Rev. Lett.* **121** (2018) no.24, 241805, arXiv:1809.02261 [hep-ex].
- [26] G. L. Fogli *et al.*, *Phys. Rev. D* **66** (2002) 053010, [hep-ph/0206162].
- [27] K. N. Abazajian *et al.*, arXiv:1204.5379 [hep-ph].
- [28] T. Asaka, S. Blanchet, and M. Shaposhnikov, *Phys. Lett. B* **631** (2005) 151, [hep-ph/0503065].
- [29] L. Covi, E. Roulet, and F. Vissani, *Phys. Lett. B* **384** (1996) 169, [hep-ph/9605319].
- [30] A. Pilaftsis, *Phys. Rev. D* **56** (1997) 5431, [hep-ph/9707235].
- [31] W. Buchmuller and M. Plumacher, *Phys. Lett. B* **431** (1998) 354, [hep-ph/9710460].
- [32] A. Pilaftsis and T. E. J. Underwood, *Nucl. Phys. B* **692** (2004) 303, [hep-ph/0309342].
- [33] S. Davidson, E. Nardi, and Y. Nir, *Phys. Rept.* **466** (2008) 105, arXiv:0802.2962 [hep-ph].
- [34] E. K. Akhmedov, V. A. Rubakov, and A. Yu. Smirnov, *Phys. Rev. Lett.* **81** (1998) 1359, [hep-ph/9803255].
- [35] T. Asaka and M. Shaposhnikov, *Phys. Lett. B* **620** (2005) 17, [hep-ph/0505013].
- [36] P. Hernández *et al.*, *JHEP* **1510** (2015) 067, arXiv:1508.03676 [hep-ph].

- [37] P. Hernández *et al.*, JHEP **1608** (2016) 157, arXiv:1606.06719 [hep-ph].
- [38] T. Hambye and D. Teresi, Phys. Rev. Lett. **117** (2016) no.9, 091801, arXiv:1606.00017 [hep-ph].
- [39] T. Hambye and D. Teresi, Phys. Rev. D **96** (2017) no.1, 015031, arXiv:1705.00016 [hep-ph].
- [40] M. Drewes *et al.*, Int. J. Mod. Phys. A **33** (2018) no.05n06, 1842002, arXiv:1711.02862 [hep-ph].
- [41] A. Aguilar-Arevalo *et al.* [LSND Collaboration], Phys. Rev. D **64** (2001) 112007, [hep-ex/0104049].
- [42] A. A. Aguilar-Arevalo *et al.* [MiniBooNE Collaboration], arXiv:1207.4809 [hep-ex].
- [43] A. A. Aguilar-Arevalo *et al.* [MiniBooNE Collaboration], Phys. Rev. Lett. **110** (2013) 161801, arXiv:1303.2588 [hep-ex].
- [44] A. A. Aguilar-Arevalo *et al.* [MiniBooNE Collaboration], Phys. Rev. Lett. **121** (2018) no.22, 221801, arXiv:1805.12028 [hep-ex].
- [45] M. G. Aartsen *et al.* [IceCube Collaboration], Phys. Rev. Lett. **117** (2016) no.7, 071801, arXiv:1605.01990 [hep-ex].
- [46] P. Adamson *et al.* [MINOS+ Collaboration], Phys. Rev. Lett. **122** (2019) no.9, 091803, arXiv:1710.06488 [hep-ex].
- [47] M. G. Aartsen *et al.* [IceCube Collaboration], Phys. Rev. D **95** (2017) no.11, 112002, arXiv:1702.05160 [hep-ex].
- [48] J. Liao and D. Marfatia, Phys. Rev. Lett. **117** (2016) no.7, 071802, arXiv:1602.08766 [hep-ph].
- [49] J. Liao, D. Marfatia, and K. Whisnant, Phys. Rev. D **99** (2019) no.1, 015016, arXiv:1810.01000 [hep-ph].
- [50] A. Esmaili and H. Nunokawa, Eur. Phys. J. C **79** (2019) no.1, 70, arXiv:1810.11940 [hep-ph].
- [51] P. B. Denton, Y. Farzan, and I. M. Shoemaker, Phys. Rev. D **99** (2019) no.3, 035003, arXiv:1811.01310 [hep-ph].
- [52] T. A. Mueller *et al.*, Phys. Rev. C **83** (2011) 054615, arXiv:1101.2663 [hep-ex].
- [53] G. Mention *et al.*, Phys. Rev. D **83** (2011) 073006, arXiv:1101.2755 [hep-ex].
- [54] P. Huber, Phys. Rev. C **84** (2011) 024617 (Erratum: Phys. Rev.C85,029901(2012)), arXiv:1106.0687 [hep-ph].
- [55] Y. J. Ko *et al.* [NEOS Collaboration], Phys. Rev. Lett. **118** (2017) no.12, 121802, arXiv:1610.05134 [hep-ex].

- [56] I. Alekseev *et al.* [DANSS Collaboration], *Phys. Lett. B* **787** (2018) 56, arXiv:1804.04046 [hep-ex].
- [57] J. N. Abdurashitov *et al.*, *Phys. Rev. C* **73** (2006) 045805, [nucl-ex/0512041].
- [58] M. Laveder, *Nucl. Phys. Proc. Suppl.* **168** (2007) 344.
- [59] C. Giunti and M. Laveder, *Mod. Phys. Lett. A* **22** (2007) 2499, [hep-ph/0610352].
- [60] S. N. Gninenco, *Phys. Rev. Lett.* **103** (2009) 241802, arXiv:0902.3802 [hep-ph].
- [61] S. N. Gninenco, *Phys. Rev. D* **83** (2011) 015015, arXiv:1009.5536 [hep-ph].
- [62] M. Masip, P. Masjuan, and D. Meloni, *JHEP* **1301** (2013) 106, arXiv:1210.1519 [hep-ph].
- [63] E. Bertuzzo *et al.*, *Phys. Rev. Lett.* **121** (2018) no.24, 241801, arXiv:1807.09877 [hep-ph].
- [64] P. Ballett, S. Pascoli, and M. Ross-Lonergan, *Phys. Rev. D* **99** (2019) 071701, arXiv:1808.02915 [hep-ph].
- [65] M. Antonello *et al.* [MicroBooNE, LAr1-ND, ICARUS-WA104 Collaboration], arXiv:1503.01520 [physics.ins-det].
- [66] J. Ashenfelter *et al.* [PROSPECT Collaboration], *Phys. Rev. Lett.* **121** (2018) no.25, 251802, arXiv:1806.02784 [hep-ex].
- [67] H. Almazán *et al.* [STEREO Collaboration], *Phys. Rev. Lett.* **121** (2018) no.16, 161801, arXiv:1806.02096 [hep-ex].
- [68] A. P. Serebrov *et al.* [NEUTRINO-4 Collaboration], *Pisma Zh. Eksp. Teor. Fiz.* **109** (2019) no.4, 209, arXiv:1809.10561 [hep-ex].
- [69] A. Atre *et al.*, *JHEP* **0905** (2009) 030, arXiv:0901.3589 [hep-ph].
- [70] M. Drewes and B. Garbrecht, *Nucl. Phys. B* **921** (2017) 250, arXiv:1502.00477 [hep-ph].
- [71] M. Galeazzi *et al.*, *Phys. Rev. Lett.* **86** (2001) 1978.
- [72] K. H. Hiddemann, H. Daniel, and O. Schwentker, *J. Phys. G* **21** (1995) 639.
- [73] E. Holzschuh *et al.*, *Phys. Lett. B* **451** (1999) 247.
- [74] E. Holzschuh *et al.*, *Phys. Lett. B* **482** (2000) 1.
- [75] J. Deutsch, M. Lebrun, and R. Prieels, *Nucl. Phys. A* **518** (1990) 149.
- [76] A. V. Artamonov *et al.* [E949 Collaboration], *Phys. Rev. D* **91** (2015) no.5, 052001 (Erratum: *Phys. Rev.D91,no.5,059903(2015)*), arXiv:1411.3963 [hep-ex].

- [77] D. I. Britton *et al.*, *Phys. Rev. Lett.* **68** (1992) 3000.
- [78] D. I. Britton *et al.*, *Phys. Rev. D* **46** (1992) R885.
- [79] A. Aguilar-Arevalo *et al.* [PIENU Collaboration], *Phys. Rev. D* **97** (2018) no.7, 072012, arXiv:1712.03275 [hep-ex].
- [80] A. Aguilar-Arevalo *et al.* [PIENU Collaboration], *Phys. Lett. B* **798** (2019) 134980, arXiv:1904.03269 [hep-ex].
- [81] G. Bernardi *et al.*, *Phys. Lett.* **166B** (1986) 479.
- [82] G. Bernardi *et al.*, *Phys. Lett. B* **203** (1988) 332.
- [83] P. Abreu *et al.* [DELPHI Collaboration], *Z. Phys. C* **74** (1997) 57 (Erratum: Z. Phys.C75,580(1997)).
- [84] O. Adriani *et al.* [L3 Collaboration], *Phys. Lett. B* **295** (1992) 371.
- [85] P. Vilain *et al.* [CHARM II Collaboration], *Phys. Lett. B* **343** (1995) 453.
- [86] A. Vaitaitis *et al.* [NuTeV, E815 Collaboration], *Phys. Rev. Lett.* **83** (1999) 4943, [hep-ex/9908011].
- [87] J. Badier *et al.* [NA3 Collaboration], *Z. Phys. C* **31** (1986) 341.
- [88] A. M. Cooper-Sarkar *et al.* [WA66 Collaboration], *Phys. Lett.* **160B** (1985) 207.
- [89] E. Gallas *et al.* [FMMF Collaboration], *Phys. Rev. D* **52** (1995) 6.
- [90] R. Aaij *et al.* [LHCb Collaboration], *Phys. Rev. Lett.* **112** (2014) no.13, 131802, arXiv:1401.5361 [hep-ex].
- [91] M. Aaboud *et al.* [ATLAS Collaboration], *JHEP* **1901** (2019) 016, arXiv:1809.11105 [hep-ex].
- [92] A. M. Sirunyan *et al.* [CMS Collaboration], *Phys. Rev. Lett.* **120** (2018) no.22, 221801, arXiv:1802.02965 [hep-ex].
- [93] A. M. Sirunyan *et al.* [CMS Collaboration], *JHEP* **1901** (2019) 122, arXiv:1806.10905 [hep-ex].
- [94] D. Liventsev *et al.* [Belle Collaboration], *Phys. Rev. D* **87** (2013) no.7, 071102 (Erratum: Phys. Rev.D95,no.9,099903(2017)), arXiv:1301.1105 [hep-ex].
- [95] J. Harrison [LHCb, BaBar, Belle Collaboration], *Nucl. Part. Phys. Proc.* **260** (2015) 143.
- [96] A. Kusenko, S. Pascoli, and D. Semikoz, *JHEP* **0511** (2005) 028, [hep-ph/0405198].
- [97] T. Asaka, S. Eijima, and A. Watanabe, *JHEP* **1303** (2013) 125, arXiv:1212.1062 [hep-ph].

- [98] K. Abe *et al.* [T2K Collaboration], Phys. Rev. D **100** (2019) no.5, 052006, arXiv:1902.07598 [hep-ex].
- [99] P. Ballett, S. Pascoli, and M. Ross-Lonergan, JHEP **1704** (2017) 102, arXiv:1610.08512 [hep-ph].
- [100] B. Abi *et al.* [DUNE Collaboration], arXiv:1807.10334 [physics.ins-det].
- [101] C. Adams *et al.* [LBNE Collaboration], arXiv:1307.7335 [hep-ex].
- [102] I. Krasnov, Phys. Rev. D **100** (2019) no.7, 075023, arXiv:1902.06099 [hep-ph].
- [103] P. Minkowski, Phys. Lett. **67B** (1977) 421.
- [104] R. N. Mohapatra and G. Senjanovic, Phys. Rev. Lett. **44** (1980) 912.
- [105] M. Gell-Mann, P. Ramond, and R. Slansky, Conf. Proc. C **790927** (1979) 315, arXiv:1306.4669 [hep-th].
- [106] T. Yanagida, Conf. Proc. C **7902131** (1979) 95.
- [107] R. N. Mohapatra and J. W. F. Valle, Phys. Rev. D **34** (1986) 1642.
- [108] M. C. Gonzalez-Garcia and J. W. F. Valle, Phys. Lett. B **216** (1989) 360.
- [109] S. M. Barr, Phys. Rev. Lett. **92** (2004) 101601, [hep-ph/0309152].
- [110] M. Malinsky, J. C. Romao, and J. W. F. Valle, Phys. Rev. Lett. **95** (2005) 161801, [hep-ph/0506296].
- [111] S. K. Kang and C. S. Kim, Phys. Lett. B **646** (2007) 248, [hep-ph/0607072].
- [112] G. 't Hooft *et al.*, NATO Sci. Ser. B **59** (1980) pp.1.
- [113] A. Denner *et al.*, Phys. Lett. B **291** (1992) 278.
- [114] A. Abada *et al.*, Phys. Rev. D **95** (2017) no.7, 075023, arXiv:1612.04737 [hep-ph].
- [115] B. Kayser and R. E. Shrock, Phys. Lett. **112B** (1982) 137.
- [116] B. Kayser, Phys. Rev. D **26** (1982) 1662.
- [117] S. Dittmaier, Phys. Rev. D **59** (1998) 016007, [hep-ph/9805445].
- [118] J. L. Diaz-Cruz, B. O. Larios, and O. Meza-Aldama, J. Phys. Conf. Ser. **761** (2016) no.1, 012012, arXiv:1608.04129 [hep-ph].
- [119] V. Shtabovenko, R. Mertig, and F. Orellana, Comput. Phys. Commun. **207** (2016) 432, arXiv:1601.01167 [hep-ph].

- [120] R. Mertig, M. Bohm, and A. Denner, *Comput. Phys. Commun.* **64** (1991) 345.
- [121] D. Gorbunov and M. Shaposhnikov, *JHEP* **0710** (2007) 015 (Erratum: *JHEP* **11**, 101 (2013)), arXiv:0705.1729 [hep-ph].
- [122] J. C. Helo, S. Kovalenko, and I. Schmidt, *Nucl. Phys. B* **853** (2011) 80, arXiv:1005.1607 [hep-ph].
- [123] K. Bondarenko *et al.*, *JHEP* **1811** (2018) 032, arXiv:1805.08567 [hep-ph].
- [124] A. B. Balantekin, A. de Gouv  a, and B. Kayser, *Phys. Lett. B* **789** (2019) 488, arXiv:1808.10518 [hep-ph].
- [125] G. Magill, R. Plestid, and Y.-D. Pospelov, Maxim and Tsai, *Phys. Rev. D* **98** (2018) no.11, 115015, arXiv:1803.03262 [hep-ph].
- [126] R. E. Shrock, *Phys. Rev. D* **24** (1981) 1275.
- [127] A. Abada *et al.*, *JHEP* **1402** (2014) 091, arXiv:1311.2830 [hep-ph].
- [128] C. Rubbia, .
- [129] P. Glassel and P. Glaessel [ALICE TPC Collaboration], *J. Phys. G* **30** (2004) S1083.
- [130] E. Cortina Gil *et al.* [NA62 Collaboration], *JINST* **12** (2017) no.05, P05025, arXiv:1703.08501 [physics.ins-det].
- [131] M. Anelli *et al.* [SHiP Collaboration], arXiv:1504.04956 [physics.ins-det].
- [132] M. Drewes *et al.*, arXiv:1806.00100 [hep-ph].
- [133] C. Ahdida *et al.* [SHiP Collaboration], *JHEP* **1904** (2019) 077, arXiv:1811.00930 [hep-ph].
- [134] A. Caputo *et al.*, *Eur. Phys. J. C* **77** (2017) no.4, 258, arXiv:1611.05000 [hep-ph].
- [135] A. Ariga *et al.* [FASER Collaboration], *Phys. Rev. D* **99** (2019) no.9, 095011, arXiv:1811.12522 [hep-ph].
- [136] F. Kling and S. Trojanowski, *Phys. Rev. D* **97** (2018) no.9, 095016, arXiv:1801.08947 [hep-ph].
- [137] R. Ammar *et al.*, *Phys. Rev. Lett.* **61** (1988) 2185.
- [138] G. A. Alves *et al.* [E769 Collaboration], *Phys. Rev. Lett.* **77** (1996) 2392.
- [139] S. Alekhin *et al.*, *Rept. Prog. Phys.* **79** (2016) no.12, 124201, arXiv:1504.04855 [hep-ph].
- [140] C. Andreopoulos *et al.*, *Nucl. Instrum. Meth. A* **614** (2010) 87, arXiv:0905.2517 [hep-ph].
- [141] T. Alion *et al.* [DUNE Collaboration], arXiv:1606.09550 [physics.ins-det].

- [142] C. Adams *et al.* [MicroBooNE Collaboration], *Eur. Phys. J. C* **79** (2019) no.8, 673, arXiv:1812.05679 [physics.ins-det].
- [143] G. J. Feldman and R. D. Cousins, *Phys. Rev. D* **57** (1998) 3873, [physics/9711021].
- [144] A. Ilakovac and A. Pilaftsis, *Nucl. Phys. B* **437** (1995) 491, [hep-ph/9403398].
- [145] A. M. Baldini *et al.* [MEG Collaboration], *Eur. Phys. J. C* **76** (2016) no.8, 434, arXiv:1605.05081 [hep-ex].
- [146] R. Alonso *et al.*, *JHEP* **1301** (2013) 118, arXiv:1209.2679 [hep-ph].
- [147] N. G. Deshpande *et al.*, *Phys. Lett. B* **703** (2011) 562, arXiv:1106.5085 [hep-ph].
- [148] A. J. Buras *et al.*, *JHEP* **1009** (2010) 104, arXiv:1006.5356 [hep-ph].
- [149] A. Abada *et al.*, *Eur. Phys. J. C* **77** (2017) no.5, 304, arXiv:1612.05548 [hep-ph].
- [150] A. Abada and M. Lucente, *Nucl. Phys. B* **885** (2014) 651, arXiv:1401.1507 [hep-ph].
- [151] S. Antusch, J. P. Baumann, and E. Fernandez-Martinez, *Nucl. Phys. B* **810** (2009) 369, arXiv:0807.1003 [hep-ph].
- [152] E. Fernandez-Martinez, J. Hernandez-Garcia, and J. Lopez-Pavon, *JHEP* **1608** (2016) 033, arXiv:1605.08774 [hep-ph].
- [153] M. Blennow *et al.*, *JHEP* **1704** (2017) 153, arXiv:1609.08637 [hep-ph].
- [154] M. Blennow *et al.*, *JHEP* **1007** (2010) 096, arXiv:1005.3240 [hep-ph].
- [155] A. Gando *et al.* [KamLAND-Zen Collaboration], *Phys. Rev. Lett.* **117** (2016) no.8, 082503, arXiv:1605.02889 [hep-ex].
- [156] M. Dentler *et al.*, *JHEP* **1808** (2018) 010, arXiv:1803.10661 [hep-ph].
- [157] A. Ankowski *et al.* [ICARUS Collaboration], *Acta Phys. Polon. B* **41** (2010) 103, arXiv:0812.2373 [hep-ex].
- [158] J. J. Back *et al.*, *Eur. Phys. J. C* **73** (2013) no.3, 2369, arXiv:1210.2215 [physics.ins-det].
- [159] P. V. Ramana Murthy *et al.*, *Nucl. Phys. B* **92** (1975) 269.
- [160] H. Abramowicz *et al.* [ZEUS Collaboration], *JHEP* **1309** (2013) 058, arXiv:1306.4862 [hep-ex].
- [161] A. Buckley *et al.*, *Eur. Phys. J. C* **75** (2015) 132, arXiv:1412.7420 [hep-ph].
- [162] K. Kovarik *et al.*, *Phys. Rev. D* **93** (2016) no.8, 085037, arXiv:1509.00792 [hep-ph].